

**GLYATL1, a Novel Player  
in Endocrine Therapy  
Resistance in  
Breast Cancer**

Janina Müller

Oral examination: 18.12.2024



Inaugural dissertation  
for  
obtaining the doctoral degree  
of the  
Combined Faculty of Mathematics, Engineering and Natural  
Science  
of the  
Ruprecht-Karls-University  
Heidelberg

Presented by

M.Sc. Janina Müller

Born in: Rottweil, Germany

Oral examination: 18.12.2024



# **GLYATL1, a Novel Player in Endocrine Therapy Resistance in Breast Cancer**

Referees: Prof. Dr. Stefan Wiemann  
Prof. Dr. Rüdiger Hell



## **Declaration of Authorship**

I hereby declare that the work presented in my dissertation was carried out between October 2020 and October 2024 under the supervision of Prof. Dr. Stefan Wiemann in the group of Molecular Genome Analysis at the German Cancer Research Center (DKFZ, Heidelberg, Germany).

If not stated differently and referenced within the text, the data described in my dissertation is original, has been gathered by myself, and has not yet been presented as a part of a university examination. All main sources, as well as the work of cooperation, have been referenced appropriately. I, as the author, hereby declare no potential conflict of interest.

Heidelberg,



# Table of Contents

<b>Summary</b> .....	<b>1</b>
<b>Zusammenfassung</b> .....	<b>3</b>
<b>1 Introduction</b> .....	<b>5</b>
1.1 Breast Cancer .....	5
1.1.1 Molecular Subtypes of Breast Cancer.....	5
1.2 Targeting the Estrogen Receptor Activity by Endocrine Therapy .....	10
1.2.1 Selective Estrogen Receptor Modulators .....	10
1.2.2 Selective Estrogen Receptor Degradar.....	11
1.2.3 Aromatase Inhibitor.....	13
1.3 Endocrine Therapy Resistance .....	14
1.4 Endocrine Therapy Resistant Cell Culture Models.....	19
1.5 Glycine N-Acyltransferase Like 1 .....	20
<b>2 Aim of the Thesis</b> .....	<b>22</b>
<b>3 Materials and Methods</b> .....	<b>24</b>
3.1 Material .....	24
3.1.1 Instruments .....	24
3.1.2 Consumables .....	25
3.1.3 Assays Kits .....	26
3.1.4 Chemicals and reagents .....	27
3.1.5 Buffers and Solutions .....	29
3.1.6 Antibodies .....	30
3.1.7 siRNAs .....	32
3.1.8 Primers.....	33
3.1.9 Software.....	33
3.2 Methods .....	34
3.2.1 Cell Culture .....	34
3.2.2 Analysis of Genomic DNA.....	38
3.2.3 Analysis of RNA Expression .....	40
3.2.4 Analysis of Protein Expression.....	43
3.2.5 Proteomic Analysis via Mass Spectrometry .....	47

3.2.6	Quantification of Intracellular Oxidative Stress.....	49
3.2.7	Metabolomics Measurement.....	50
3.2.8	Analysis of Epigenetic Profile - EpiTOF .....	52
3.2.9	Data Analysis.....	54
<b>4</b>	<b>Results.....</b>	<b>55</b>
4.1	<i>GLYATL1</i> Expression is Increased in Aromatase Inhibitor-Resistant Cell Lines .....	55
4.2	High <i>GLYATL1</i> Expression is Associated with Poor Patient Prognosis .....	56
4.3	<i>GLYATL1</i> Expression is Correlated with Estrogen Supply.....	57
4.4	Regulation of <i>GLYATL1</i> Expression by ER $\alpha$ and FOXA1 .....	59
4.5	Generation of a <i>GLYATL1</i> -specific Antibody.....	62
4.6	<i>GLYATL1</i> Knockdown Reduces Cell Proliferation .....	64
4.7	<i>GLYATL1</i> Knockout Has a Proliferation Disadvantage .....	65
4.8	<i>GLYATL1</i> Overexpression Alone Does not Confer Endocrine Therapy Resistance .....	67
4.9	Interaction Partner of <i>GLYATL1</i> .....	70
4.10	<i>GLYATL1</i> is Localized in the Mitochondria .....	73
4.11	Influence of <i>GLYATL1</i> on Acyl-CoA Abundance and Water-soluble Metabolites.....	74
4.12	Effect of <i>GLYATL1</i> on Reactive Oxygen Species .....	81
4.13	Downstream Effect of Resistance on Epigenetic Modifier.....	86
4.14	Global Changes in the Epigenetic Landscape .....	90
4.15	Differential Pathways and Transcription Factor Activity upon <i>GLYATL1</i> Knockout .....	97
4.16	Deregulated Histone Modulator upon <i>GLYATL1</i> Knockout.....	108
4.17	Changes in Full Proteome.....	110
<b>5</b>	<b>Discussion.....</b>	<b>115</b>
5.1	<i>GLYATL1</i> Expression Anticorrelates with Estrogen Supply .....	115
5.2	Regulatory Interplay between ER and FOXA1 Regulates <i>GLYATL1</i> Expression under Estrogen-Deprived Conditions .....	116
5.3	Downregulation of <i>GLYATL1</i> but not Overexpression Influences Cell Proliferation.....	118

5.4	<i>GLYATL1</i> Contributed to Succinic Acid Accumulation, however, does not Influence Glutamine Dependency .....	118
5.5	Mitochondrial <i>GLYATL1</i> Modulates Oxidative Stress Levels .....	122
5.6	<i>GLYATL1</i> Contributed to Epigenetic Reprogramming .....	123
5.7	<i>GLYATL1</i> Expression Negatively Influence p53 Pathway Activation .....	126
5.8	<i>GLYATL1</i> Contributed to Proliferation in Endocrine Therapy-Resistant Cells .....	128
5.9	<i>GLYATL1</i> Modulates Activity of TGF $\beta$ Pathway and Associated Effectors.....	129
5.10	<i>GLYATL1</i> Expression Anticorrelates with JAK-STAT Signaling.....	131
5.11	Clonal Heterogeneity in <i>GLYATL1</i> Knockout Cell Lines.....	132
5.12	Adaptive Cellular Responses to Partial versus Complete <i>GLYATL1</i> Loss .....	134
<b>6</b>	<b>Conclusion and Outlook.....</b>	<b>136</b>
	<b>Abbreviations .....</b>	<b>138</b>
	<b>Acknowledgments .....</b>	<b>142</b>
	<b>References.....</b>	<b>144</b>
	<b>Supplementary Data .....</b>	<b>164</b>

## List of Figures

<b>Figure 1:</b> HER2 signaling .....	8
<b>Figure 2:</b> Estrogen Receptor Signaling .....	10
<b>Figure 3:</b> Mode of action of SERM tamoxifen.....	11
<b>Figure 4:</b> Mode of action of SERD fulvestrant .....	12
<b>Figure 5:</b> Mode of action of Aromatase inhibitor.....	13
<b>Figure 6:</b> PI3K/AKT/mTOR pathway .....	16
<b>Figure 7:</b> Cell cycle regulation by CDK4/6-CycD.....	17
<b>Figure 8:</b> Tamoxifen metabolism .....	19
<b>Figure 9:</b> GLYATL1-catalyzed reaction .....	21
<b>Figure 10:</b> Basal mRNA and protein GLYATL1 levels in wildtype and LTED cells.....	56
<b>Figure 11:</b> Survival analysis based on <i>GLYATL1</i> expression in patients. .	57
<b>Figure 12:</b> Effect of Estrogen presence on <i>GLYATL1</i> expression .....	58
<b>Figure 13:</b> Effect of short-term estrogen supply on <i>GLYATL1</i> expression	59
<b>Figure 14:</b> Transcription factor occupancy of <i>GLYATL1</i> promoter. ....	60
<b>Figure 15:</b> Effect of <i>ESR1</i> knockdown on <i>GLYATL1</i> expression.....	61
<b>Figure 16:</b> Effect of <i>FOXA1</i> knockdown on <i>GLYATL1</i> expression .....	62
<b>Figure 17:</b> Generation of <i>GLYATL1</i> specific antibody .....	63
<b>Figure 18:</b> <i>GLYATL1</i> knockdown reduces cell proliferation.....	64
<b>Figure 19:</b> Scheme of <i>GLYATL1</i> knockout.....	66
<b>Figure 20:</b> <i>GLYATL1</i> knockout reduces cell proliferation .....	67
<b>Figure 21:</b> Validation of <i>GLYATL1</i> overexpressing cell lines.....	68
<b>Figure 22:</b> Effect of <i>GLYATL1</i> overexpression on MCF7 cell proliferation under endocrine therapy condition.....	69
<b>Figure 23:</b> BioID2 experiment.....	70
<b>Figure 24:</b> Western blots of Streptavidin pull-downs of indicated BioID constructs.....	72
<b>Figure 25:</b> Distinct mitochondrial localization of <i>GLYATL1</i> by immunostaining.....	74
<b>Figure 26:</b> Glutamine dependency of wildtype, LTED, and <i>GLYATL1</i> knockout cells. ....	75
<b>Figure 27:</b> Altered abundance of various intracellular Acyl-CoA species. .	76
<b>Figure 28:</b> Principal component analysis of full metabolome data.....	78

<b>Figure 29:</b> Full metabolome of wildtype, resistant, and <i>GLYATL1</i> knockout MCF7 cell lines .....	80
<b>Figure 30:</b> Basal oxidative stress levels in MCF7 and T47D cells .....	82
<b>Figure 31:</b> H <sub>2</sub> O <sub>2</sub> -specific ROS levels .....	83
<b>Figure 32:</b> Cytoplasmic and mitochondrial H <sub>2</sub> O <sub>2</sub> -specific ROS levels .....	85
<b>Figure 33:</b> Altered HDAC and KAT expression and IC <sub>50</sub> determination of specific inhibitors.....	87
<b>Figure 34:</b> Effect of HDAC and KAT inhibition on proliferation .....	89
<b>Figure 35:</b> Effect of <i>KAT6B</i> knockdown on proliferation .....	90
<b>Figure 36:</b> Analysis of Histone 3 K9 and K14 acetylation levels.....	91
<b>Figure 37:</b> Analysis of the Epigenetic profile and cell identity markers using EpiTOF .....	93
<b>Figure 38:</b> Spearman Correlation Matrix of Histone Modifications and Cell Identity Markers from both EpiTOF run .....	94
<b>Figure 39:</b> Cluster-based analysis of EpiTOF data.....	96
<b>Figure 40:</b> Transcriptomic changes upon <i>GLYATL1</i> deregulation in MCF7 .....	98
<b>Figure 41:</b> Gene Set Enrichment Analysis of RNA sequencing results ...	101
<b>Figure 42:</b> Pathway activity prediction of <i>GLYATL1</i> knockdown and knockout conditions .....	104
<b>Figure 43:</b> Transcription factor activity prediction .....	107
<b>Figure 44:</b> Expression profile of Histone Modifiers .....	110
<b>Figure 45:</b> Analysis of full proteome .....	111

## List of Tables

<b>Table 1:</b> Description of used human cell lines and corresponding media composition.....	35
<b>Table 2:</b> Composition of Lysis Buffer for genomic DNA isolation.....	38
<b>Table 3:</b> Composition of Phusion PCR master mix.....	38
<b>Table 4:</b> Phusion PCR thermocycler protocol.....	39
<b>Table 5:</b> Reverse Transcription master mix.....	40
<b>Table 6:</b> Reverse Transcription thermocycler protocol.....	40
<b>Table 7:</b> Real-time qPCR master mix.....	41
<b>Table 8:</b> Real-time qPCR thermocycler protocol.....	41
<b>Table 9:</b> Summary of experimental determined IC50 values of Garcinol and TMP269.....	88
<b>Table 10:</b> Antibody panel of the EpiTOF experiment.....	92
<b>Table 11:</b> Gene set enrichment analysis of full proteome data using the hallmark gene collection from the Molecular Signature Database.....	114

## List of Supplementary Tables

<b>Supplementary Table 1:</b> Gene set enrichment analysis of RNA sequencing data using the hallmark gene collection from the Molecular Signature Database.....	164
---	-----





## Summary

Breast cancer is the most commonly diagnosed cancer and a leading cause of cancer-related death in females. The most prevalent breast cancer subtype, luminal A, is characterized by high expression and activity of the estrogen receptor (ER). These luminal A patients typically have a favorable prognosis due to the availability of endocrine therapies targeting the estrogen receptor, like tamoxifen and fulvestrant, or by inhibiting aromatase, a critical enzyme in estrogen synthesis. However, 40- 50% of ER-positive breast cancers with late-stage disease either fail to respond to this therapeutic approach or relapse as a consequence of *de-novo* or acquired endocrine therapy resistance.

This study focuses on characterizing *GLYATL1* (glutamine-N-acyltransferase), a gene previously found to be highly upregulated in aromatase inhibitor-resistant luminal A breast cancer cell lines. In these cell lines, I observed that *GLYATL1* expression is inversely correlated with estrogen supply and is regulated by the luminal transcription factors FOXA1 and ESR1 under estrogen-depleted conditions. While *GLYATL1* overexpression alone was insufficient to induce a resistant phenotype, knockdown, and knockout partially re-sensitize resistant cells to antiestrogen treatment.

Despite the distinct mitochondrial localization of *GLYATL1* and the enzymatic ability to transfer acyl groups to glutamine, I could not identify a specific acyl donor or metabolic pathway alterations influenced by *GLYATL1*. However, I could observe that *GLYATL1* promoted succinate accumulation and contributed to maintaining low oxidative stress levels in the resistant cells. These alterations could lead to several biological changes such as pathway deregulation and epigenetic reprogramming.

In the *GLYATL1* knockout cell lines, I could observe significant upregulation of p53 and the JAK-STAT signaling pathway, along with downregulation of the TGF $\beta$  and key cell cycle regulator pathways. In contrast, these pathways were partially inversely activated in the resistant cells compared to wildtype cells. Furthermore, I could observe a significant influence of *GLYATL1* on the epigenetic landscape, specifically on H3K27 acetylation and dimethylation, H3K4 trimethylation, and H3K64 acetylation histone modifications.

These findings highlight a novel role of GLYATL1 in the context of endocrine therapy resistance in ER-positive breast cancer by potentially impacting succinate accumulation, and oxidative stress levels, consequently inducing epigenetic reprogramming, and deregulation of several key pathways contributing to therapy resistance and disease progression.

## Zusammenfassung

Brustkrebs ist weltweit die am häufigsten diagnostizierte Krebserkrankung bei Frauen und zählt zu den führenden Ursachen krebsbedingter Todesfälle. Der am weitesten verbreitete Subtyp ist Luminal A, welcher durch eine hohe Expression und Aktivität des Östrogenrezeptors (ER) charakterisiert ist. Patientinnen mit Luminal A-Tumoren haben in der Regel eine günstige Prognose, da ihnen effektive endokrine Therapien zur Verfügung stehen. Zu den gängigen Behandlungsansätzen zählen Tamoxifen und Fulvestrant, die direkt auf den Östrogenrezeptor wirken, sowie Aromatasehemmer, die die Synthese von Östrogen blockieren. Jedoch sprechen 40-50% der Patientinnen mit einem ER-positiven Tumor im fortgeschrittenen Stadium entweder nicht auf diesen Therapieansatz an oder erleiden nach anfänglichen Erfolg einen Rückfall aufgrund einer *de-novo* oder erworbenen Resistenz gegen die endokrine Behandlung.

In diese Studie wurde das Gen *GLYATL1* (glutamine-N-acyltransferase) untersucht, welches in luminalen A-Brustkrebszelllinien mit Resistenz gegen Aromataseinhibitoren stark hochreguliert ist. In diesen Zellen konnte ich beobachten, dass die Expression von *GLYATL1* negativ mit der Östrogenzufuhr korrelierte und durch die luminalen Transkriptionsfaktoren FOXA1 und ESR1 reguliert wurde. Während eine Überexpression von *GLYATL1* keine resistenten Phenotyp herbeiführte, sensibilisierte *GLYATL1* Knockdown und knockout die resistenten Zellen gegenüber einer Antiöstrogenbehandlung.

Trotz einer mitochondrialen Lokalisierung und der katalytischen Fähigkeit von *GLYATL1* Acylgruppen auf Glutamin zu übertragen, konnten ich keine spezifischen Acyl-donoren oder signifikante Veränderungen im Stoffwechsel feststellen. Ich konnte jedoch feststellen, dass *GLYATL1* eine Akkumulation von Succinat förderte und zu der Aufrechterhaltung eines niedrigen oxidativen Stresslevels beitrug. Diese Veränderungen könnten zelluläre Veränderungen begünstigen, wie der Deregulierung von Signalwegen und der Beeinflussung epigenetischer Faktoren.

Der *GLYATL1* knockout führte zu einer signifikanten Aktivierung der p53- und JAK-STAT Signalwege, sowie zu einer Herunterregulierung von TGFβ – und Zellzyklus-Regulationswegen. Diese Signalwege zeigten in den resistenten Zellen im Vergleich zu dem Wildtype eine teilweise Umkehrung der Aktivität auf. Darüber hinaus konnte

ich einen signifikanten Einfluss von GLYATL1 auf epigenetischen Modifikationen, insbesondere auf die H3K27 Acetylierung und Dimethylierung, H3K4 Trimethylierung sowie H3K64 Acetylierung, beobachten.

Diese Ergebnisse deuten auf eine neuartige Rolle von GLYATL1 im Zusammenhang mit der endokrinen Therapieresistenz bei ER-positivem Brustkrebs hin, indem es möglicherweise die Succinat-Akkumulation und das oxidativen Stresslevel beeinflusst und dadurch eine epigenetische Umprogrammierung und die Deregulierung mehrerer Schlüsselwege induziert, die zur Therapieresistenz und zum Fortschreiten der Erkrankung beitragen können.

# 1 Introduction

## 1.1 Breast Cancer

Worldwide approximately 2.3 million women were diagnosed with breast cancer, which corresponds to 23.8% of all new cancer cases in females in 2022. Breast cancer is thus the most commonly diagnosed cancer and the second leading cause of cancer-related death in women, following lung cancer [1, 2]. Since 2014, breast cancer incidence rates have increased annually by 0.5% in the United States [3]. Despite the rising incidences, advances in detection and treatment strategies have contributed to an overall 5-year relative survival rate of 91.2% [4]. However, the survival rate varies significantly depending on the stage of diagnosis. The rate decreases as the cancer progresses from over 99% for early-stage breast cancer to a 5-year relative survival rate of 29% for metastatic late-stage tumors [3]. The overall prognosis and survival rate of breast cancer patients are not only dependent on the stage at the time of diagnosis but are also highly influenced by the molecular subtype of the tumor.

### 1.1.1 Molecular Subtypes of Breast Cancer

Breast cancer is a heterogeneous disease, characterized by distinct subtypes. Three subtypes, named Triple-negative, HER2 enriched, and Luminal can be distinguished by a unique molecular profile, gene expression profile, and clinical behavior. These subtypes exhibit significant differences in incidence, risk factors, prognosis, and treatment sensitivities.

In clinical practice, the expression patterns of biomarkers, including the estrogen Receptor  $\alpha$  (ER), progesterone receptor (PR), human epidermal growth factor receptor 2 (HER2), and the proliferation marker protein Ki-67 are determined to approximate the intrinsic subtypes [5, 6]. The evaluation of these biomarkers is typically conducted using immunohistochemistry to assess protein expression and fluorescence in situ hybridization to evaluate HER2 gene amplification [7, 8].

### 1.1.1.1 The Triple Negative Subtype

Approximately 10-15% of all breast cancer patients are classified as triple-negative, a subtype characterized by the absence of ER, PR expression, and the absence of HER2 overexpression or gene amplification [9].

The term “triple negative breast cancer” is frequently utilized as a synonym for the “basal-like” molecular subtype. While there is considerable overlap between the two groups, they are not entirely synonymous. Approximately 70-75% of patients with triple-negative cancer are considered to be basal-like, however, not all triple-negative cancers display a basal-like structure [10-12]. The basal-like subtype displays distinct molecular hallmarks, including a high prevalence of mutations in the cellular tumor antigen p53 (*TP53*), loss of retinoblastoma protein (*RB1*) and Breast cancer type 1 susceptibility protein (*BRCA1*) expression, high activation of the phosphatidylinositol-4,5-bisphosphate 3-kinase (PI3K) pathway. Moreover, the basal-like subtype is typically characterized by the expression of basal markers such as cytokeratins and augmented proliferation through hyperactivation of Forkhead box protein M1 (FOXO1) [13].

Chemotherapy remains the primary systematic treatment option for these patients. Despite higher responsiveness to neoadjuvant chemotherapy compared to other subtypes, these patients exhibit a higher likelihood of distant recurrence and mortality within five years of diagnosis [14-16]. The addition of carboplatin to the standard neoadjuvant taxane regimen significantly enhanced treatment response, resulting in improved event-free survival and overall survival rates [17]. Moreover, the combination of chemotherapy with bevacizumab, an anti-angiogenic agent targeting the vascular endothelial growth factor (VEGF), significantly increased the proportion of patients who achieved a pathological complete response [18].

Recently, novel therapeutic approaches have emerged transforming the treatment landscape and offering new therapeutic options. Antibody-drug conjugates are a novel therapeutic approach in which monoclonal antibodies are conjugated with small cytotoxic drug molecules by linkers that enable the targeted treatment of cancer cells. Sacituzumab govitecan is an antibody-drug conjugate consisting of an antibody targeting the trophoblast cell-surface antigen 2 (Trop-2), which is highly expressed in the majority of breast cancer cells, conjugated to topoisomerase I inhibitor SN-38 by a linker. Sacituzumab govitecan, which was approved by the Food and Drug Administration

(FDA) in 2020 as a third-line therapy, significantly elevated progression-free survival and overall response rates in comparison to chemotherapy, particularly in patients with intermediate or high Trop-2 expression levels [19-22].

Additionally, poly(ADP-ribose) polymerases (PARP) inhibitors, such as olaparib and talazoparib, which target PARP enzymes involved in single-strand DNA repair, are effective in cancers with defects of homologous recombination. Such defects of homologous recombination are often associated with mutations in the *BRCA1/2* gene. In metastatic triple-negative breast cancer patients with such germline *BRCA* mutation, olaparib and talazoparib significantly improved overall survival and progression-free survival compared to chemotherapy [23-25].

Furthermore, immune checkpoint inhibitors have emerged as a promising treatment approach for triple-negative breast cancer patients, harboring a higher number of tumor-infiltrating lymphocytes, high levels of the programmed cell death ligand 1 (PD-L1), or a higher number of nonsynonymous mutations. Combination therapy with chemotherapy and one of the two FDA-approved immune checkpoint inhibitors atezolizumab, which targets the PD-L1, or the antibody pembrolizumab, targeting the programmed cell death protein 1 (PD-1), significantly improved clinical outcomes [26-29].

### **1.1.1.2 The HER2-enriched Subtype**

The HER2-enriched breast cancer subtype is characterized by elevated RNA and protein levels of the human epidermal growth factor receptor 2 (HER2) and the absence of ER and PR expression.

The HER2 protein is a transmembrane receptor tyrosine kinase and belongs to the epidermal growth factor receptor family. Unlike other members of this family, HER2 has no known activating ligand and thus requires homo- or heterodimerization with other receptor tyrosine kinases such as HER1 (EGFR) HER3, and HER4 for activation. This dimerization leads to autophosphorylation of the cytoplasmic domain, which triggers a variety of downstream signaling pathways, including the mitogen-activated protein kinase (MAPK), and phosphatidylinositol-4,5-bisphosphate 3-kinase (PI3K) path-

ways. Activation of these downstream pathways is crucial for gene transcription involved in cellular processes such as cell proliferation and survival ultimately leading to uncontrolled growth of cancer cells (Figure 1) [30-33].

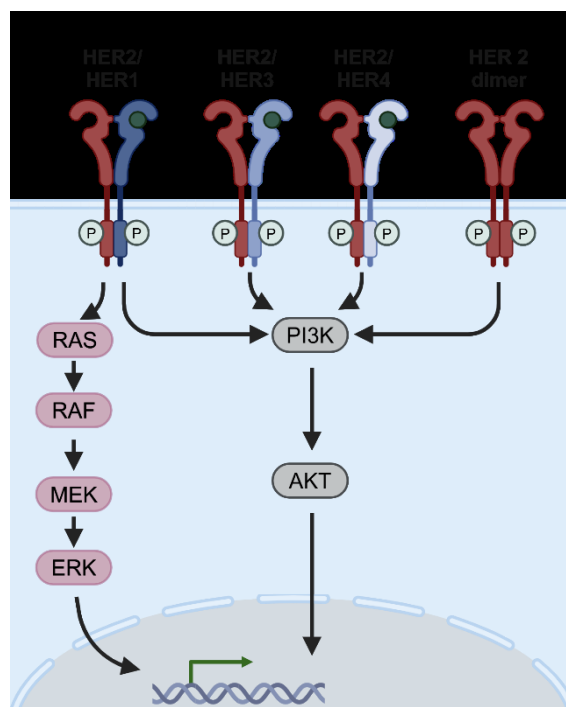


**Figure 1: HER2 signaling.** Dimerization of receptor tyrosine kinase HER2 leads to auto-phosphorylation triggering downstream signaling through MAPK and PI3K and ultimately to transcription of target genes involved in diverse cellular processes. Adapted from Lee et al [34], created with BioRender.com.

*HER2* overexpression is observed in approximately 15-20% of all breast cancers and constitutes one of the earliest events during carcinogenesis [5]. Historically, *HER2* amplification and overexpression were associated with poor prognosis. However, the prognosis has significantly improved with the implementation of novel *HER2*-targeted therapies. The monoclonal antibody trastuzumab targets the extracellular domain of the *HER2* receptor and has been shown to induce clinical benefits in combination with chemotherapy [35-37].

Moreover, the addition of pertuzumab, another monoclonal antibody that targets *HER2*, has been shown to further enhance treatment efficacy. Clinical trials have demonstrated that the combination of trastuzumab, pertuzumab, and chemotherapy

significantly improved progression-free survival and overall survival compared to trastuzumab and chemotherapy alone [38].

### 1.1.1.3 The Luminal Subtypes

The majority of breast tumors belong to the luminal subtypes due to the expression of estrogen receptors and/or progesterone receptors. The luminal subtype can be further subclassified into two subtypes, luminal A and luminal B, which are distinguished by different gene expression patterns. The most prevalent subtype, luminal A, typically has higher expression of hormonal receptors, negative HER2 expression, and elevated gene expression for proteins involved in cell differentiation and cell adhesion [39].

In contrast, the luminal B subtype typically has lower PR expression and can display positive HER2 expression. Additionally, the luminal B subtype is characterized by elevated levels of genes associated with immune response, including interleukin 2 receptor  $\alpha$  and the T-lymphocyte activation antigen CD86. Furthermore, luminal B demonstrates enrichment of genes involved in proliferation, including Ki-67 and cyclin B1, which collectively indicate elevated proliferation rates and a more aggressive phenotype [39, 40].

Luminal breast cancer is typically treated with endocrine therapy that targets the oncogenic driver, the ER, or the biosynthesis of its ligand. The ER is a member of the nuclear hormone receptor family, which are transcription factors activated by receptor-specific ligands [41, 42].  $17\beta$ -estradiol is the most potent and biologically active form of estrogen and exhibits highly selective binding to the ligand-binding pocket of the estrogen receptor. Following ligand binding, the ER undergoes a conformational change that induces homodimerization. Subsequently, the dimer translocates into the nucleus, where it can directly bind to specific DNA sequences in the promoter region of target genes, which are known as estrogen-response elements (ERE). The transcription of target genes is controlled by cofactors that bind to the hydrophobic groove on the estrogen receptor through canonical LXXLL motifs. These cofactors can therefore activate (coactivators) or inactivate (corepressors) the ER transcriptional complex (Figure 2) [43, 44]. The estrogen receptor is thus capable of regulating the transcription

of several thousand canonical target genes, influencing various cellular pathways such as proliferation and survival.

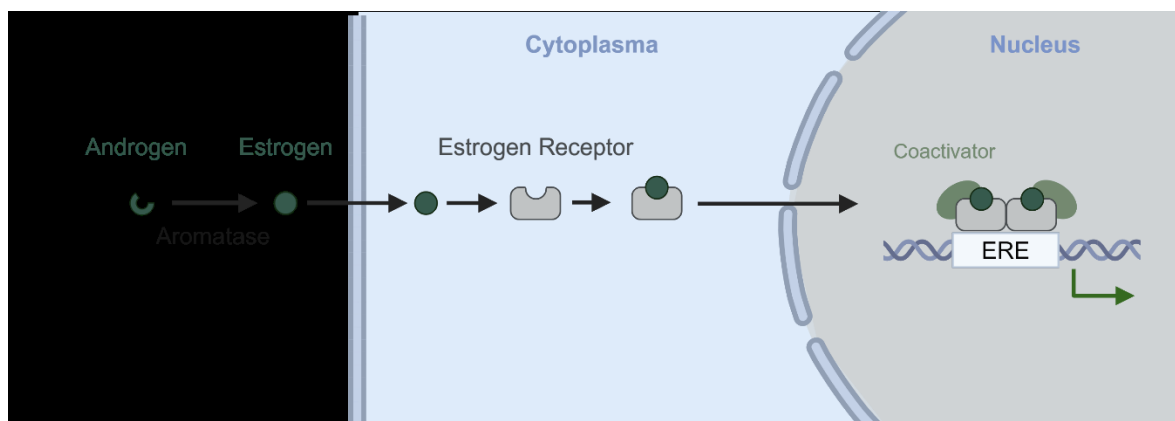


**Figure 2: Estrogen Receptor Signaling.** The enzyme aromatase catalyzes the transition of estrogen from its progenitor androgen. Upon estrogen binding to the estrogen receptor, the estrogen receptor dimerizes and translocates into the nucleus to subsequently bind estrogen response elements (ERE). Transcription of target genes is initiated by coactivator binding. Adapted from Schuurman et al [45], created with BioRender.com.

## 1.2 Targeting the Estrogen Receptor Activity by Endocrine Therapy

Treatment of estrogen-positive breast cancer often involves surgery followed by adjuvant endocrine therapy to reduce the progression of dormant or micrometastatic cells. Furthermore, endocrine therapy is a key element in treating advanced or metastatic luminal tumors. This therapy approach directly targets the estrogen receptor or its ligand, estrogen, to abolish the estrogen signaling, thereby inhibiting tumor growth and disease progression. Three different drug families are currently available for clinical use.

### 1.2.1 Selective Estrogen Receptor Modulators

The drug family of Selective Estrogen Receptor Modulators (SERMs) can act as estrogen agonists or antagonists depending on the target tissue. In breast tissue, SERMs can inhibit the estrogen receptor, thereby preventing tumor growth and cancer progression in luminal breast cancer. The binding of SERMs on estrogen receptors

causes a conformational change, which occludes the coactivator recognition groove and simultaneously allows corepressor binding to the ER (Figure 3) [44, 46].

The first SERM, tamoxifen, is approved for both pre- and post-menopausal women in adjuvant and early-stage settings [47, 48]. In clinics, tamoxifen has significantly improved survival rates for breast cancer patients and remains a cornerstone of endocrine therapy. Recent studies have demonstrated that extending adjuvant treatment for ten years, rather than stopping after five years, provides further benefits by reducing recurrence and decreasing mortality by half [49].

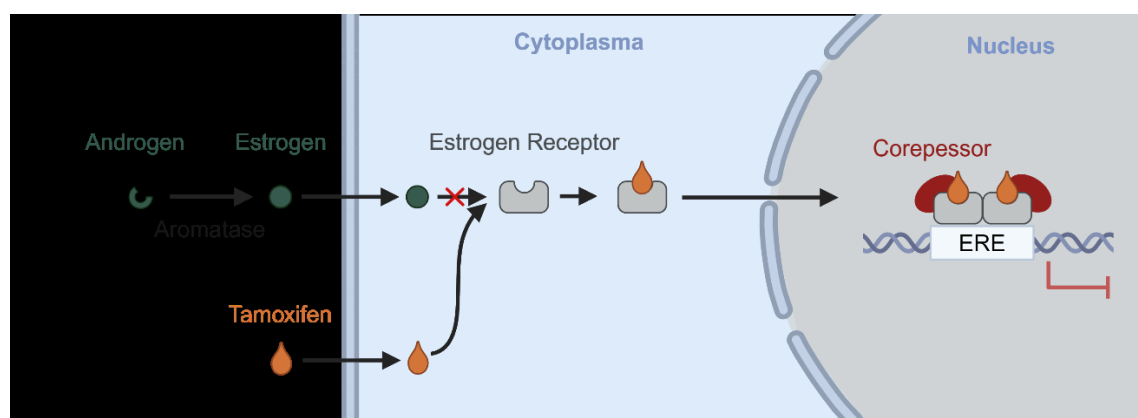


**Figure 3: Mode of action of SERM tamoxifen.** Tamoxifen competes with estrogen for estrogen receptor binding. Following binding and translocation into the nucleus, conformational changes in the estrogen receptor lead to corepressor binding. This interaction consequently inhibits the transcription of target genes. Adapted from Schuurman et al [45], created with BioRender.com.

### 1.2.2 Selective Estrogen Receptor Degradator

Unlike selective SERMs, which primarily modulate the activity of the estrogen receptor, selective estrogen degraders (SERDs) function by binding to the ER and facilitating its degradation. This mechanism effectively abolishes the estrogen signaling pathway [50, 51].

Fulvestrant, the first and until January 2023 the only approved SERD [52], binds the monomeric estrogen receptor with a binding affinity that is 89% that of  $17\beta$ -estradiol [53]. This strong binding prevents dimerization and translocation into the nucleus [54,

55]. Following binding to the ER, fulvestrant induces a conformational change that promotes the dissociation of chaperone proteins from the receptor. This conformational change exposes a hydrophobic surface, which can then be recognized by the E2 ubiquitin-conjugating enzyme complex. The binding of this enzyme complex leads to the ubiquitination of the ER by E3 ubiquitin ligase, which subsequently triggers the recognition and targeted degradation by the proteasome (Figure 4) [56-58].

While fulvestrant monotherapy provides modest clinical benefits, with a median progression-free survival of approximately 2 months [59], fulvestrant remains effective in tumors refractory to tamoxifen and aromatase inhibitors, including tumors with mutations in the ER gene *ESR1* [60, 61]. However, it is important to note that fulvestrant requires intramuscular injections, which can be a drawback for some patients. In response to this clinical restriction, the FDA recently approved the oral SERD elacestrant. This approval was based on the EMERALD trial, which demonstrated significant improvements in clinical outcomes, particularly for patients harboring *ESR1* mutations, as a second-line or later treatment for advanced or metastatic ER-positive, HER2-negative breast cancer [62].

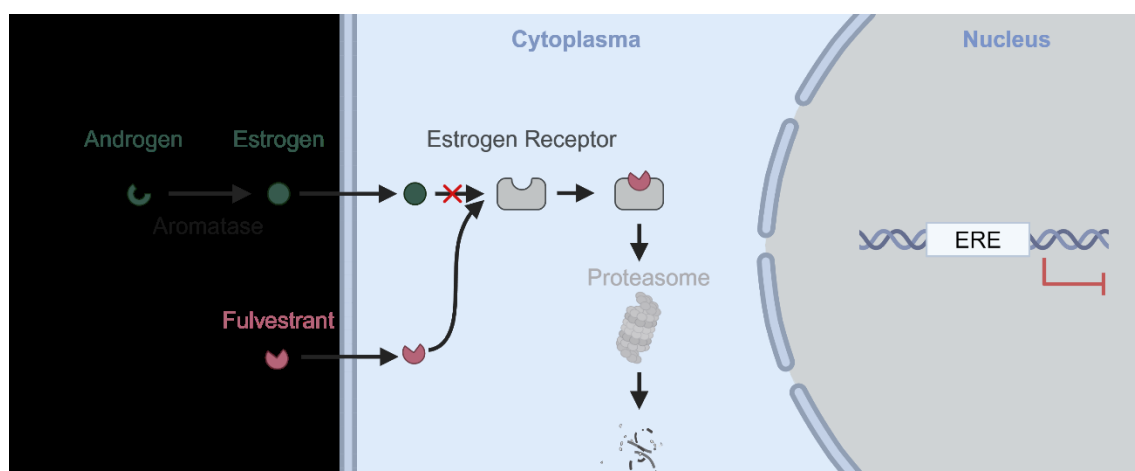


**Figure 4: Mode of action of SERD fulvestrant.** Fulvestrant competes with estrogen for estrogen receptor binding. Following binding, conformational changes in the estrogen receptor lead to proteasomal degradation. Adapted from Schuurman et al [45], created with BioRender.com.

### 1.2.3 Aromatase Inhibitor

In contrast to SERMs and SERDs, which target the estrogen receptor directly, aromatase inhibitors (AIs) block estrogen signaling by inhibiting the rate-limiting step in estrogen biosynthesis (Figure 5). In pre-menopausal females, the ovaries are the main source of estrogen [63, 64], whereas in post-menopausal women, estrogen is primarily produced through the conversion of androgens to estrogen by the peripheral enzyme aromatase (CYP19A1) [65-68]. Thus, AIs are primarily prescribed for post-menopausal women in both early-stage and metastatic settings to diminish the estrogen pool within the body. Compared to tamoxifen treatment, post-menopausal females showed superior clinical response with aromatase inhibitors in first-line therapy [69, 70].

Aromatase inhibitors are classified into two main types. Type I aromatase inhibitors, such as exemestane, are steroidal and function as irreversible inhibitors of aromatase competing with the natural substrate androgen [71].

In contrast, type II non-steroidal aromatase inhibitors, like anastrozole and letrozole can reversibly bind the heme iron in the catalytic center of aromatase enzymes, which occludes the substrate binding site and consequently prevents the conversion of androgens to estrogen [72-74].

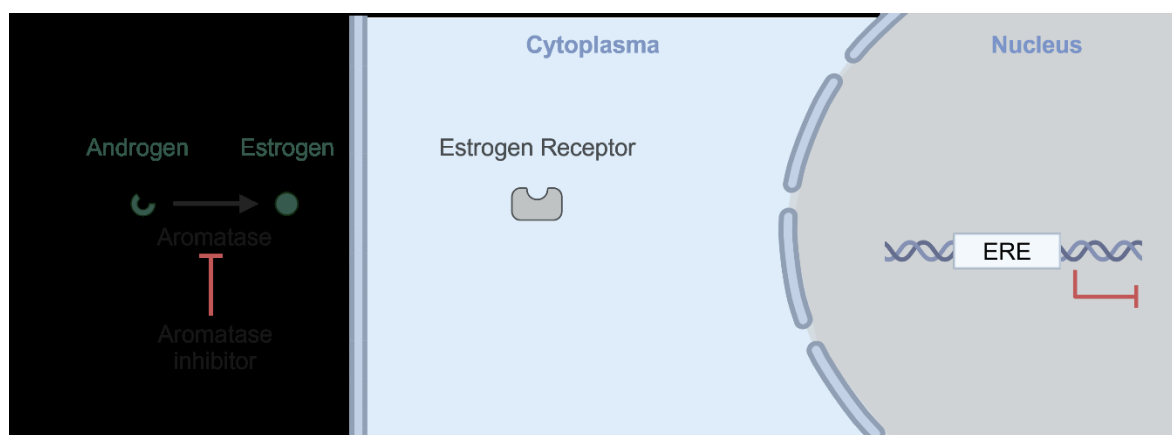


**Figure 5: Mode of action of Aromatase inhibitor.** Aromatase inhibitors directly influence estrogen abundance by inhibiting aromatase, an enzyme involved in the synthesis of estrogen from androgen. Created with BioRender.com.

### 1.3 Endocrine Therapy Resistance

Despite the success of endocrine therapy, up to 40-50% of patients with late-stage disease do not respond or relapse to this therapy approach [75]. De novo and/or acquired resistant tumors often display a more aggressive and metastatic phenotype. Recent studies shed light on several mechanisms contributing to endocrine resistance in breast cancer.

#### Activation of receptor tyrosine kinases

Receptor tyrosine kinases are a class of cell surface receptors that trigger downstream cascades in response to their respective ligand including growth factors, hormones, and cytokines. The superfamily of receptor tyrosine kinases comprises different receptors like the epidermal growth factor receptors (EGFR), insulin-like growth factor-I receptors (IGF-IR), fibroblast growth factor receptors (FGFRs), and vascular endothelial growth factor receptors (VEGFR) [76]. Aberrant expression or activation of these receptor tyrosine kinases was found to be one driving element in endocrine therapy resistance and an indication of poor prognosis [77].

In particular, expression and/or amplification of HER2 in originally HER2-negative tumors were observed in tamoxifen-resistant tumors, indicating a switch to HER-positivity [78]. Furthermore, activating mutations in the HER2 gene are associated with both intrinsic and acquired endocrine therapy resistance [79, 80]. Activated HER2 in resistant patients thus opens up the potential of combinational therapy, which demonstrated significant benefits in previous studies. In-vitro targeting EGFR and HER2 using the inhibitor lapatinib significantly restored endocrine sensitivity in resistant cell lines [81]. Furthermore, a treatment regime comprising the pan HER inhibitor neratinib and fulvestrant showed encouraging activity in ER+/HER2-mutated breast cancer patients [82].

Besides the influence of active HER2 on therapy resistance, members of the highly conserved FGFR family are often deregulated in various cancers and were associated with endocrine therapy resistance in ER-positive breast cancer [83-85]. Targeting the FGFR family with a pan-FGFR inhibitor in combination with endocrine therapy showed promising therapeutic benefits in patients with the FGFR pathway amplified in early-

phase trials. These promising studies highlight FGFR as a therapeutic target in the future [86, 87].

### **PI3K/AKT/mTOR Pathway Activation**

One of the downstream effectors of receptor tyrosine kinases is the PI3K/AKT/mTOR signaling cascade. In response to growth factor signaling, Phosphatidylinositol-3-kinase (PI3K) is activated and catalyzes the conversion of phosphatidylinositol-4,5-bisphosphate (PIP<sub>2</sub>) to phosphatidylinositol-3,4,5-trisphosphate (PIP<sub>3</sub>). PIP<sub>3</sub> functions as a second messenger by activating downstream effectors like the serine/threonine kinases AKT and mTOR, which are key regulators of several cellular processes like proliferation, apoptosis, and cell cycle (Figure 6) [88].

Mutation in the *PIK3CA* gene or other aberrant activation of the PI3K/AKT/mTOR pathway can ultimately result in enhanced cell proliferation and cancer growth, and induce the development of adaptive resistance mechanisms toward endocrine therapy [89, 90]. Moreover, PI3K and AKT can directly phosphorylate the serine 167 residue of the ER, thereby causing estrogen-independent activation and loss of sensitivity to anti-estrogens [91].

Combinational strategies combining PI3K/AKT/mTOR inhibitor with endocrine therapy have been increasingly studied and developed as a promising therapeutic approach to overcome antiestrogen therapy resistance in luminal breast cancer patients. The combination of fulvestrant with either buparlisib, a pan-PI3K inhibitor, or capivasertib, a pan-AKT inhibitor, significantly increased progression-free survival [92, 93]. Furthermore, therapeutically targeting the downstream effector mTOR by everolimus in combination with either tamoxifen or an aromatase inhibitor significantly improves the therapeutic outcome of AI-resistant patients [94, 95]. Resistant patients with *PIK3CA*-mutated benefit particularly with a treatment regimen comprising the PI3K inhibitor alpelisib in combination with fulvestrant [96].

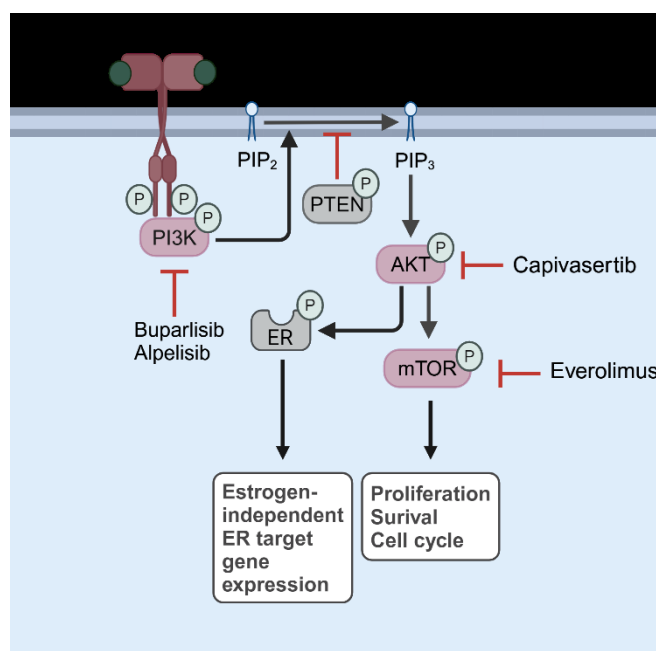


**Figure 6: PI3K/AKT/mTOR pathway.** Growth factor binding leads to activated Phosphatidylinositol-3-kinase (PI3K) triggering the transition of phosphatidylinositol-4,5-bisphosphate (PIP<sub>2</sub>) to the second messenger phosphatidylinositol-3,4,5-trisphosphate (PIP<sub>3</sub>). This second messenger leads to activation of serine/threonine kinase AKT and ultimately mTOR activation. Additionally, active AKT can phosphorylate the estrogen receptor (ER) leading to estrogen-independent downstream signaling. Adapted from Janku et al [97], created with BioRender.com.

### Altered Cell-cycle Regulation

The cell cycle is tightly regulated to allow proper and controlled cell division. Estrogen plays a crucial role in promoting cell cycle progression from G1 to S phase by stimulating the expression of key cell cycle regulators, including cyclin D1 and c-MYC [98, 99]. In the G1 phase, Cyclin D forms an active complex with cyclin-dependent kinases (CDK) 4 and 6. This activated complex targets and phosphorylates the retinoblastoma protein (pRB) driving the transition of G1 to S phase (Figure 7) [100].

Persistent expression of cyclin D, hyperactivation of CDK4/6, loss of pRB activity, and/or the persistent phosphorylation of pRb can lead to aberrant cell-cycle regulation and is associated with resistance to endocrine therapy [101, 102]. The development of potent CDK4/6 inhibitors transformed the therapeutic landscape for endocrine therapy-resistant breast cancer patients. The small molecule inhibitors palbociclib, ribociclib,

and abemaciclib significantly enhance treatment outcomes in combination with endocrine therapy and are now FDA-approved for first-line or advanced settings [103-107].

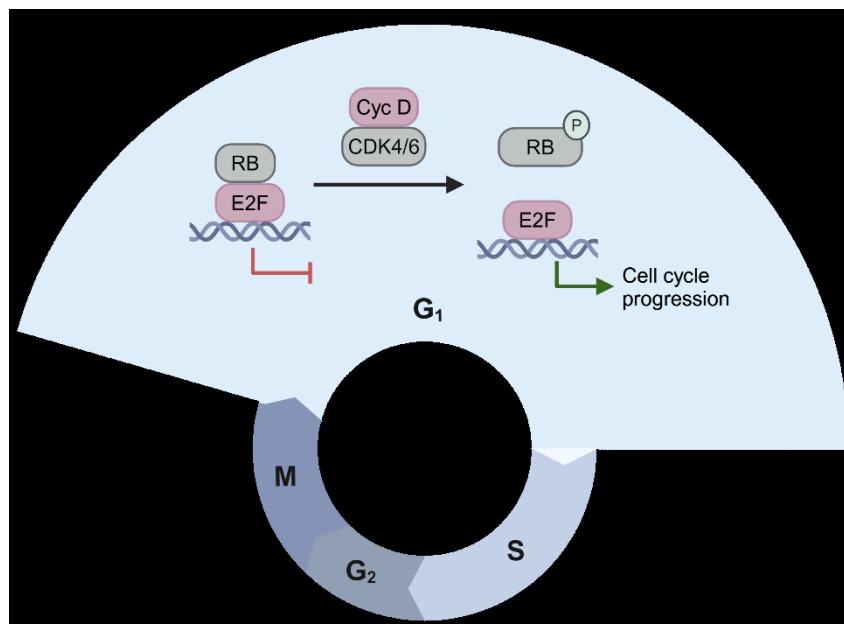


**Figure 7: Cell cycle regulation by CDK4/6-CycD.** Cyclin-dependent kinases (CDK) in active complexes with cyclin D (CycD) can phosphorylate retinoblastoma (Rb) protein. Upon phosphorylation, Rb releases E2F transcription factors promoting transcription of cyclin E triggering cell cycle progression. Created with BioRender.com.

### Alteration in ER and ER Pathway

Less than 5% of primary tumors harbors mutations in ER clustering in the ligand-binding domain. However, the incidences significantly increases in relapsed endocrine therapy treated tumors to approximately 18% [61, 108]. The most frequently observed mutations include Tyr537Ser, Thy537Asn and Asp538Gly. These mutations induce structural changes that favor an agonist conformation, and thereby enhancing constitutive estrogen-independent transcription [61, 109].

Furthermore, in-frame gene fusion involving the estrogen receptor (ESR1) and the transcriptional coactivator YAP1 leads to truncations of the ER. This truncation results in the loss of the ligand-binding domain while retaining the DNA-binding domain, transforming the receptor into an estrogen-independent transcription factor that is insensitive to endocrine treatment approaches [110].

## Epigenetic Modifications

Recent research has highlighted the pivotal role of epigenetic alterations as a fundamental mechanism underlying this resistance. One mechanism through which epigenetic changes contribute to endocrine therapy resistance is via direct DNA methylation of estrogen-response elements. This DNA methylation impedes estrogen receptor binding, thereby reducing estrogen-mediated transcription.

Furthermore, DNA methylation in the ER promoter region can result in transcriptional silencing and, consequently, the downregulation of ER expression [111]. The lack of ER expression is one of the main principal mechanisms of de novo endocrine therapy resistance. Additionally, ER silencing can be a result of alterations in the activity and expression of histone deacetylases (HDACs). The deacetylation of histones results in the formation of a closed nucleosome structure, which directly influences gene accessibility and causes the transcriptional silencing of ER [112, 113].

To address this clinical challenge, treatment with different inhibitors targeting epigenetic modifiers has demonstrated promising outcomes. The HDAC inhibitors entinostat and scriptaid successfully cause re-expression of ER, thereby sensitizing the tumor to aromatase and tamoxifen treatment respectively [114-116]. Additionally, the combination of HDAC inhibitors with a DNA methyltransferase 1 (DNMT-1) inhibitor has been shown to further enhance ER expression while also addressing the epigenetic silencing of key genes involved in hormone response [117, 118].

## Metabolic Resistance

*In-vivo*, tamoxifen undergoes hepatic oxidation by cytochrome P450 2D6 (CYP2D6), resulting in the formation of principal active metabolites, 4-hydroxytamoxifen and endoxifen (Figure 8) [119]. This metabolic conversion significantly enhances the binding affinity to the estrogen receptor similar to the binding affinity of 17 $\beta$ -estradiol. These active metabolites are therefore more effective at binding to the ER and suppressing downstream signaling [120]. However, approximately 7% of the patients are unable to effectively metabolize tamoxifen due to genetic alterations or loss of function in *CYP2D6* gene [121]. These poor metabolizers have significantly lower concentrations

of the active metabolite 4-Hydroxytamoxifen, which negatively influences the therapy efficiency [119, 120, 122, 123].

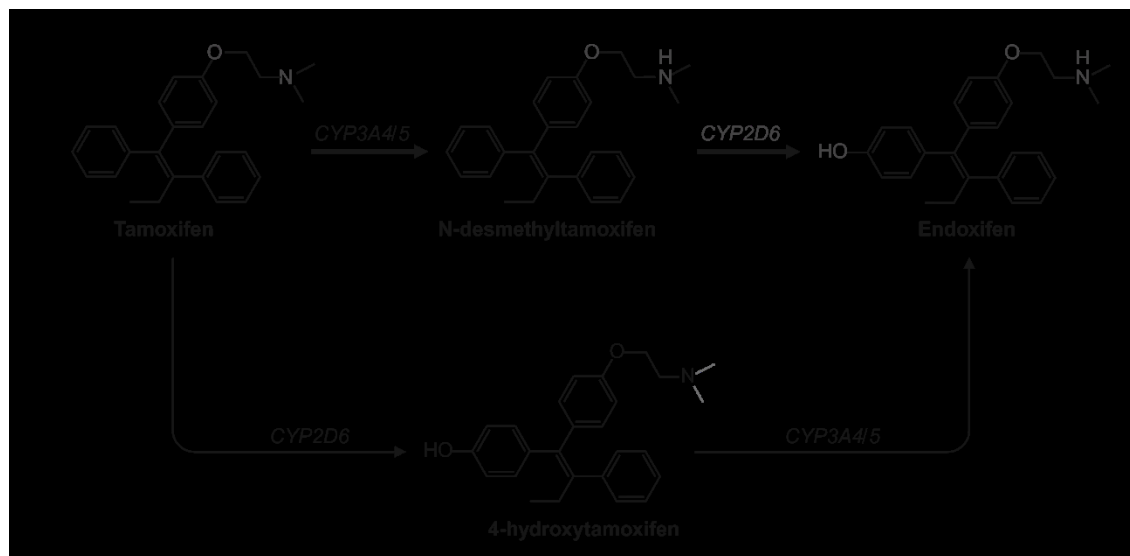


**Figure 8: Tamoxifen metabolism.** Tamoxifen is primarily metabolized in the liver by cytochrome P450 enzymes into its active metabolites endoxifen and 4-hydroxytamoxifen. Adapted from Jordan et al [124], created with BioRender.com.

## 1.4 Endocrine Therapy Resistant Cell Culture Models

Endocrine therapy breast cancer cell line models significantly shaped the current knowledge of resistance mechanisms and are valuable *in-vitro* tools for studying and developing new therapeutic approaches. The first resistant cell line model dates back to the 1980s [125]. Since then, many different laboratories developed various resistant cell line models using estrogen receptor-positive cell lines such as MCF7 and T47D. Typically, these parental cell lines were exposed to intermittent or increasing concentrations of 4-hydroxytamoxifen or fulvestrant for extended periods of several weeks or months to acquire resistance. Long-term estrogen-deprived (LTED) cells simulate resistance towards aromatase inhibitors and are routinely created under estrogen-depleted conditions. These cells frequently display retained or even increased ER expression, allowing for estrogen-independent ER-mediated growth. Thus, these cells often respond to different SERDs but show a resistant phenotype towards SERMs [126, 127].

Upon treatment, the cultures initially undergo cell death and quiescence. However, over time, resistant clones emerge and proliferate. These resistant clones could represent small, pre-existing subpopulations within the original parental culture that already possessed estrogen-independent growth capabilities or subpopulations that acquired resistance over time [128, 129].

Despite the upregulation of common pathways, the different cell line models, which were developed in numerous laboratories under slightly different conditions, exhibit specific phenotypes due to genetic and evolutionary variations. These variations lead to cell line-specific behavior, which therefore cannot be directly transferred to other model systems.

The MCF7 and T47D LTED cell lines in this study were generated under estrogen-deprived conditions for twelve months by the Magnani group at the Imperial College London (MCF7) or in-house by previous PhD students Dr. Emre Sofyali and Dr. Simone Borgoni (T47D). Extensive genomic studies revealed alterations in gene expression patterns and pathways [130].

## 1.5 Glycine N-Acyltransferase Like 1

RNA sequencing of resistant MCF7 and T47D LTED cells indicated *GLYATL1* as one of the highest upregulated genes in comparison to parental wildtype MCF7 cells [131]. The glycine-N-acyltransferase like 1/glutamine-N-acyltransferase (*GLYATL1*) gene maps to human chromosome 11 and encodes the enzyme GLYATL1 having a molecular weight of ~35 kDa. Under normal conditions, GLYATL1 is highly expressed in the liver and kidney [132], where it catalyzes the transfer of an acyl group to the  $\alpha$ -amino group of glutamine (Figure 9). Besides using glutamine as substrate, GLYATL1 was also found to bind with glycine, even though with a lower affinity than towards glutamine [133]. Affinity-purified recombinant GLYATL1 demonstrated notable arylacetyl transferase activity utilizing phenylacetyl-CoA and benzoyl-CoA as substrates [134].

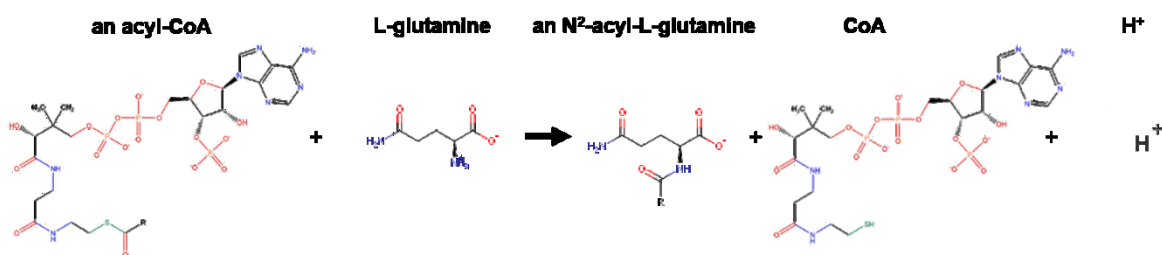


**Figure 9: GLYATL1-catalyzed reaction.** The reaction catalyzed by glycine N-acyl-transferase like 1 (GLYATL1) involves the transfer of an acyl group from an acyl-CoA to glutamine, forming an N-acyl-L-glutamine product and releasing coenzyme A (CoA). Created with ChemDraw.

*GLYATL1* expression is significantly altered in several cancer entities, influencing prognosis and disease progression. For instance, elevated *GLYATL1* expression is associated with a shorter overall survival rate in acute myeloid leukemia patients [135]. Additionally, *GLYATL1* was found to be highly expressed in colorectal and prostate cancers [136-138]. In prostate cancer cell lines, the knockdown of *GLYATL1* was observed to negatively influence cell proliferation and colony formation, accompanied by an enrichment of glycolysis, gluconeogenesis, and hypoxia-inducible factor 1 signaling [138, 139]. Additionally, *GLYATL1* expression was found to be significantly influenced by androgen treatment and the transcription factor ETV1 prostate cancer cell line [139]. Conversely, a reduction in *GLYATL1* expression in tissues with elevated basal *GLYATL1* levels, such as the kidney and liver, has been observed to influence cancer progression. In particular, low *GLYATL1* expression in renal cell carcinoma is associated with advanced stages and correlates with short overall and disease-free survival by influencing small metabolic processes such as carboxylic acid, amino acid, fatty acid, and immune infiltration [140, 141]. A similar correlation with the overall patient survival rate was identified in hepatocellular carcinoma, where *GLYATL1* was identified as one of ten core hub genes [142, 143].

Understanding the mechanism of action of GLYATL1 is thus crucial for evaluating its potential as a molecular target or diagnostic biomarker.

## 2 Aim of the Thesis

Breast cancer is the most commonly diagnosed cancer in women globally and is one of the leading causes of cancer-related death. The majority of breast tumors are classified as luminal breast cancer, which is characterized by high expression of the estrogen receptor. Luminal A tumors are therapeutically treated with endocrine therapy targeting the estrogen receptor or its ligand estrogen. Despite the best prognosis of these patients of all subtypes, frequent failure and resistance toward endocrine therapy remain an urgent clinical problem. Recent studies have identified *GLYATL1* as a highly upregulated gene in resistant MCF7 and T47D *in-vitro* models. Although *GLYATL1* was found to be involved in various cancer types, the function of *GLYATL1* is not well studied. In particular, the involvement of *GLYATL1* and its impact on endocrine therapy resistance remains elusive.

Based on this background, the aim of my PhD thesis is to elucidate the role of *GLYATL1* in endocrine therapy resistance in breast cancer. To achieve this, I applied the following approaches:

- Analyze the influence of estrogen depletion and drug withdrawal on *GLYATL1* expression to gain insights into the connection between endocrine therapy resistance and *GLYATL1* expression.
- Generate stable clonal *GLYATL1* knockout cell lines to facilitate downstream functional studies.
- Investigate the influence of *GLYATL1* knockdown, knockout, and overexpression on the phenotypical behavior and characteristics of breast cancer cells.
- Construct a functional network around *GLYATL1*:
  - o Analyze the subcellular localization of *GLYATL1*.
  - o Identify the impact of *GLYATL1* on cellular pathways contributing to resistance.
- Identify alterations in the epigenetic landscape associated with resistance and the impact of *GLYATL1*.
- Profile transcriptomic and proteomic changes following *GLYATL1* knockdown and knockout in resistant cell lines to elucidate the molecular changes associated with *GLYATL1* activity.

## Aim of the Thesis

---

This comprehensive approach aims to uncover the role of GLYATL1 in endocrine therapy resistance.

### 3 Materials and Methods

#### 3.1 Material

##### 3.1.1 Instruments

<b>Instrument</b>	<b>Manufacturer</b>
Axiovert 40 CFL	Zeiss
Bacterial incubator (37°)	Memmert
Bacterial shaking incubator (37°)	INFORS HAT
Biohit Proline multichannel pipette	Sartorius
Cell culture hood HERA Safe	Thermo Fisher Scientific
Cell culture incubator	Heraeus
Cell Observer	Zeiss
Centrifuges	Eppendorf AG
Extracellular flow bioanalyzer (Seahorse XF96)	Agilent Technologies
Fluidlab R-300	Anvajo
Flow Cytometer FACSCalibur	BD Biosciences
Freezer (-20°C)	Liebherr
Freezer (-80°C)	Sanyo
Fridge (+4°)	Liebherr
F.SIGHT	Cytexa
Gel documentation system	Herolab
Glomax explorer plate reader	Promega
Helios™ II CyTOF®	Standard BioTools
ImageXpress Micro XLS	Molecular Devices
ImageXpress Micro Confocal	Molecular Devices
LSM 900 Airyscan	Zeiss
Nanodrop ND-1000 spectrophotometer	Thermo Fisher Scientific
Neubauer cell counting chamber	BRAND
Odyssey Infrared Imaging System	LI-COR Biosciences
Orbitrap Exploris 480	Thermo Fisher Scientific
Pipetboy acu pipette	INTEGRA Biosciences

Pipetman® pipette	Gilson
Protein Gel Apparatus MiniProtean II	Bio-Rad
Q Exactive Plus mass spectrometer	Thermo Fisher Scientific
QuantStudio 5 real-time PCR machine	Thermo Fisher Scientific
Thermocycler	Applied Biosystems
Thermomixer	Eppendorf
Titramax 100 rocking platform	Heidolph
Trans-Blot Turbo Transfer	Bio-Rad
Ultimate 3000 liquid chromatography (LC) system	Agilent
Ultracentrifuge, Beckman L8-70M	Beckman Coulter
Vacuboy aspiration device	INTEGRA Biosciences
Vacuum concentrator	Labconco
Vortex mixer	neoLab
Water bath	GFL

### 3.1.2 Consumables

Consumable	Manufacturer
384-well plates for qPCR	Thermo Fisher Scientific
4-15% Mini-PROTEAN®TGX™ Pre-cast Protein Gels (10,12 and 15-well)	Bio-Rad
96-well canonical bottom plate	Thermo Fisher Scientific
96-well plate (black)	Greiner Bio-One
Adhesive Optically Clear Plate Seal	Thermo Fisher Scientific
Canonical tubes (15 ml and 50 ml)	BD Falcon
Cell culture dishes (100 mm and 150 mm)	Greiner Bio-one
Cell scraper	Corning
Cryogenic vials	Thermo Fisher Scientific
Disposable filter tips	Starlab
Disposable tips	Steinbrenner
FACS tubes	BD Falcon
HiTrap™ Protein G HP column	Cytiva
Micro centrifuge tubes (1,5,2 and 5 ml)	Eppendorf

Multi-well plates cell culture plates (6, 12, 24, 48, 96-well)	Greiner Bio-one
PCR strips	Steinbrenner Laborsysteme
Pierce™ snap-cap spin columns	Thermo Fisher Scientific
PVDF blotting membrane	Merck
Reservoirs 50ml	Corning
Serological pipettes (5mL, 10mL, 25mL, 50ml)	BD Falcon
Syringes	Sigma-Aldrich
Syringe filters	Sigma-Aldrich
Trans-Blot Turbo™ Mini PVDC Transfer Packs	Bio-Rad
Whatman 3 mm filter paper	GE Healthcare

### 3.1.3 Assays Kits

<b>Kit</b>	<b>Manufacturer</b>
AllPrep DNA/RNA Micro Kit	Qiagen
Cell-ID 20-Plex Pd Barcoding Kit	Fluidigm
CellTiter-Glo Luminescent assay	Promega
Click-iT™ EdU Cell Proliferation Kit for Imaging, Alexa Fluor™ 594 dye	Thermo Fisher Scientific
DNeasy Blood & Tissue Kit	Qiagen
Maxpar Nuclear Antigen Staining Buffer Set	Fluidigm
MIBItag Conjugation Kit	IONPATH
NE-PER Nuclear Cytoplasmic Extraction Kit	Thermo Fisher Scientific
Plasmid Plus Midi Kit	Qiagen
Pierce™ BCA Protein Assay Kit	Thermo Fisher Scientific
RevertAid™ H Minus First Strand cDNA synthesis kit	Thermo Fisher Scientific
RNeasy Mini Kit	Qiagen
Trans-Blot Turbo mini PVDF Transfer Kit	Bio-Rad
Wizard SV Gel and PCR Clean-up System	Promega

### 3.1.4 Chemicals and reagents

Chemical/reagent	Manufacturer
0.25% Trypsin EDTA Solution	Gibco
<sup>13</sup> C <sub>3</sub> -Malonyl-CoA	Cambridge Isotope laboratories
17-β-estradiol	Sigma-Aldrich
5xHF buffer	Thermo Fisher Scientific
6x Orange Loading Dye	Fermentas
Acetic Acid	Sigma-Aldrich
Acrylamide/bisacrylamide 37.5:1	Carl Roth
Agar	Sigma-Aldrich
Agarose	Carl Roth
amide-HILIC column (2.6 μm, 2.1x100 mm)	Thermo Fisher
Ammonium peroxodisulfate (APS)	Sigma-Aldrich
Ampicillin	Sigma-Aldrich
Biotin	Sigma-Aldrich
Blasticidin	Thermo Fischer Scientific
Bovine serum albumin (BSA)	Sigma-Aldrich
Charcoal Stripped Fetal Bovine Serum (CSFBS)	Sigma-Aldrich
Cisplatin	Fluidigm
cOmplete EDTA-free protease Inhibitor	Roche
Crystal violet	Sigma-Aldrich
deuterium labelled TCA cycle intermediates	Cambridge Isotope laboratories
DMEM medium	Gibco
DMSO	Sigma-Aldrich
dNTPs	Thermo Fisher Scientific
EDTA	Sigma-Aldrich
Ethanol	Sigma-Aldrich
Ethidium bromide	Sigma-Aldrich
Fetal Bovine Serum (FBS)	Gibco
Glycine	Sigma-Aldrich

Hoechst 33258	Sigma-Aldrich
Iridium	Fluidigm
Isopropanol	Greiner Bio-One International
LB Broth	Sigma-Aldrich
L-glutamine	Gibco
Lipofectamine 2000	Thermo Fischer Scientific
Lipofectamine RNAiMAX	Thermo Fischer Scientific
MassRuler DNA Ladder Low Range	Fermentas
Methanol	Greiner Bio-One International GmbH
MeOH/H <sub>2</sub> O/Acetonitrile (50/20/30 v/v)	Phenomenex
Magnesium chloride (MgCl <sub>2</sub> )	Thermo Fisher Scientific
Nuclease-free water	Thermo Fisher Scientific
Opti-MEM	Gibco
Paramagnetic beads	Sigma Aldrich
PageRuler™ Prestained Protein Ladder	Thermo Fisher Scientific
Penicillin/Streptomycin (P/S)	Gibco
Phosphate-Buffer Saline (PBS)	Gibco
PhosSTOP Phosphatase Inhibitor Cocktail	Roche
Phusion Hot Start II DNA-Polymerase (2 U/μL)	Thermo Fisher Scientific
Pierce™ High Capacity Streptavidin Agarose	Thermo Fisher Scientific
Pierce™ Lane Marker Non-reducing Sample Buffer	Thermo Fisher Scientific
Pierce™ Paraformaldehyde 16% (w/v), Methanol-free	Thermo Fisher Scientific
Power SYBR Green PCR Master Mix (2x)	Thermo Fisher Scientific
Proteinase K	Sigma-Aldrich
Puromycin	Thermo Fischer Scientific
RIPA Lysis and Extraction buffer	Thermo Fischer Scientific
RNase A	Qiagen

RNase-free DNase	Qiagen
Rockland Blocking Buffer	Rockland Immunochemicals
Roti®-Load 1, 4x sample loading buffer	Carl Roth
Sodium chloride (NaCl)	VWR International
Sodium dodecyl sulfate (SDS)	Carl Roth
Sodium fluoride (NaF)	Bernd Kraft
Sodium hydroxide (NaOH)	Sigma-Aldrich
Sodium orthovanadate (Na <sub>3</sub> VO <sub>4</sub> )	Bernd Kraft
Sodium pyruvate, 100mM	Gibco
stable isotope labeled amino acids and	Cambridge Isotope Laboratories
TEMED	Carl Roth
Tris-base	Sigma-Aldrich
Triton X-100	Sigma-Aldrich
Trypsin 0.05%/EDTA 0.1% in PBS, w/o Ca and Mg	PAN-Biotech GmbH
Tween 20	Sigma-Aldrich
(Z)-4-Hydroxytamoxifen ≥98%	Sigma-Aldrich

### 3.1.5 Buffers and Solutions

<b>Western Blotting</b>	
10x TBS	1.37 M NaCl 200 mM Tris pH 7.6
Blocking Buffer	1:1 Rockland blocking buffer: TBS 10 mM NaF 1 mM Na <sub>3</sub> VO <sub>4</sub>
Lysis Buffer	10 mL RIPA buffer 1x cOmplete EDTA-free protease inhibitor 1x PhosphoSTOP phosphatase inhibitor
	Lysis Buffer 10 mM NaF

Lysis Buffer for Mass Spectrometry	1 mM Na <sub>3</sub> VO <sub>4</sub> 150 U/mL Benzonase 10 U/mL RNase-free DNase
SDS running buffer	192 mM glycine 25 mM Tris 0.1% SDS (w/v)
Transfer buffer	10% Trans-Blot Turbo™ 5x Transfer Buffer 20% EtOH 60% dH <sub>2</sub> O
Blocking Buffer (TBST)	0.1% Tween20 in TBS
<b>BioID2</b>	
NP-40 Lysis Buffer	50 mM Tris-HCl pH 8.0 150 mM NaCl 1 mM EDTA 0.2% NP-40
<b>Immunofluorescence</b>	
Fixation Buffer	4% PFA in PBS
Permeabilization Buffer	0.5% Triton X-100 in PBS
Blocking Buffer	3% BSA in PBS

### 3.1.6 Antibodies

<b>Primary antibodies</b>				
<b>Target</b>	<b>Antibody-ID</b>	<b>Manufacturer</b>	<b>Species</b>	<b>Dilution</b>
β-Actin	69100	MP Biologicals	Mouse	1:10 000
β-Actin	A5060	Sigma Aldrich	Rabbit	1:10 000
Flag-tag	F3165	Sigma Aldrich	Rabbit	1:1 000
GLYATL1	HPA039501	Human Protein Atlas	Rabbit	1:1 000
Streptavidin-680	S32358	Invitrogen		1:5 000
Myc-tag	CST2276	Cell Signaling Technology	Mouse	1:1 000

<b>Secondary antibodies</b>				
F(ab') <sub>2</sub> -Goat anti-Rabbit IgG (H+L) Cross-Adsorbed Secondary Antibody, Alexa Fluor™ 680	A-21077	Thermo Fisher Scientific	Goat	1:10 000
Goat anti-Mouse IgG (H+L) Secondary Antibody, DyLight 800 4X PEG	SA5-35521	Thermo Fisher Scientific	Goat	1:10 000
<b>Metal-coupled antibodies for EpiTOF experiment</b>				
<b>Target</b>	<b>Metal</b>	<b>Antibody-ID</b>	<b>Manufacturer</b>	<b>Amount per 1 million cells [μL]</b>
Tri-Methyl-Histone H3 (Lys4)	145Nd	9751	Cell Signaling Technology	0,5
Di-Methyl-Histone H3 (Lys36)	149Sm	2901	Cell Signaling Technology	1
H4K16AC	152Sm	2901	Cell Signaling Technology	0,3
H3K4me1	154Sm	2901	Cell Signaling Technology	0,5
Anti-Histone H3.3	155Gd	176840	Abcam	1,5
Anti-Histone H3 (acetyl K64) antibody	156Gd	251549	Abcam	0,25
Acetyl-Histone H3 (Lys27)	160Gd	8173	Cell Signaling Technology	0,1
Histone H3K27me3	168Er	61017	Active Motif	0,4
H3K9me3	170Er	2901	Cell Signaling Technology	0,5
Anti-pHistone H3 [S28]	175Lu	3175012A	FLUIDIGM	1

Anti-Human CD326/EpCAM	141Pr	3141006B	FLUIDIGM	2
Anti-Human CD24	166Er	3166007B	FLUIDIGM	2
Anti-Human/Mouse CD49F	164Dy	3164006B	FLUIDIGM	2
Anti-Human/Mouse CD44	171Yb	3171003B	FLUIDIGM	2
K5	140Ce	236216	Abcam	1
H3K27me2	142Nd	24684	Abcam	0,75
H3K9me2	151Eu	173325	Abcam	2
H2Aub	153Eu	8420	Cell Signaling Technology	0,1
H4	159Tb	13919	Cell Signaling Technology	1,5
H4K20me3	161Dy	239410	Abcam	0,4
H3K36me3	165Ho	4909BF, lot4	Cell Signaling Technology	2
H3K9ac	169Tm	61663	Active Motif	0,5
Ki-67	172Yb	3172024B	FLUIDIGM	0,25
K8/18	174Yb	3174014A	FLUIDIGM	1
ER	163Dy	3163024A	FLUIDIGM	1

### 3.1.7 siRNAs

The siRNA pools for knockdown experiments of *ESR1*, *FOXA1*, *GLYATL1*, and *KAT6B* were purchased by siTOOLS Biotech. Untarget Control siPools negC served as a negative control.

### 3.1.8 Primers

Gene	Primer forward (5'-3')	Primer reverse (5'-3')
<i>ACTB</i>	ATTGGCAATGAGCGGTTC	GGATGCCACAGGACTCCA
<i>ESR1</i>	GATGGGCTTACTGACCAACC	AAAGCCTGGCACCCCTCTT
<i>GLYATL1</i>	CACATCAATCACGGGAACC	CCATGTCATCAGTCATCTCCTG
<i>PUM1</i>	TCACATGGATCCTCTTCAAGC	CCTGGAGCAGCAGAGATGTAT
<i>FOXA1</i>	TAATCATTGCCATCGTGTGCTT	ATAATGAAACCCGTCTGGCTA
<i>GLYATL1</i> <i>KO locus</i>	GCATGGGTTTTGGAGACAGT	CATATCCATTCAGACAGGCTCC
<i>KAT6B</i>	CCCATGAGAAAGACCAGCCC	CAAACAGGATGGGTGTCCACT

### 3.1.9 Software

Software	Manufacturer
BD FACSDiva™ Software	Becton Dickinson
BioRender	<a href="https://www.biorender.com/">https://www.biorender.com/</a>
GraphPad Prism 5	GraphPad Software, Inc.
Fiji/ImageJ 1.53q	<a href="https://fiji.sc/">https://fiji.sc/</a> [144]
Flowing Software v2.5.1	Becton Dickinson
GSEA v4.1.0	Broad Institute, Inc.
Image Studio v5.2	LI-COR Biosciences
Inkscape v1.2	Software Freedom Conservancy, Inc.
Molecular Devices Analysis Software	Molecular Devices
MetaboAnalyst 6.0	<a href="https://www.metaboanalyst.ca/MetaboAnalyst/home.xhtml">https://www.metaboanalyst.ca/MetaboAnalyst/home.xhtml</a>
Odyssey 2.1	LI-COR
QuantStudio Analysis and Design v1.5.1	Thermo Fisher Scientific
R v4.3.2	R Core Team
R studio 2023.09.01	Posit PBC
SnapGene software 6.1.2	Insightful Science

## 3.2 Methods

### 3.2.1 Cell Culture

#### 3.2.1.1 Cultivation of Cancer Cell Lines

T47D parental breast cancer cell lines were obtained from ATCC. T47D wildtype cell line was used by two former PhD students, Dr. Simone Borgoni and Dr. Emre Sofyali, to generate T47D long-term estrogen-depleted (LTED) cells mimicking resistance towards aromatase inhibition. The Magnani Lab (ICL, London) kindly provided MCF7 LTED cells and the corresponding parental MCF7 wildtype cell line. The cell lines were authenticated by Multiplexon GmbH and tested for potential mycoplasma contamination regularly.

All cells were cultivated at 37°C and 5% CO<sub>2</sub> in a humidified incubator in the appropriate growth media (Table 1). After reaching 70-80% confluency, cells were subcultivated. To this end, cells were washed once with PBS and incubated with 0.25% trypsin-EDTA to detach the cells. The enzymatic reaction of trypsin was stopped by adding corresponding media and, subsequently, cells were re-seeded in an appropriate dilution. To abolish the interaction of the pH indicator phenol-red with the estrogen receptor and the resulting weak estrogenic effect [145], LTED cells were detached with phenol-red-free trypsin and cultivated in phenol-red-free media. Stable viral transduced cell lines were selected in the presence of 1 µg/mL blasticidin or puromycin in the media.

To prepare for extended storage, cells were centrifuged at 1,500 xg for 5 minutes and the resulting pellet was resuspended in media containing 70% normal growth media, 20% FBS/CS-FBS, and 10% DMSO. Aliquots of 1\*10<sup>6</sup> cells in 1 mL freezing media were transferred into cryovials and frozen down in an isopropanol bath to -80°C. Finally, cells were transferred to liquid nitrogen for long-term storage.

Frozen cells were reactivated by thawing at 37°C and then transferred into a dish containing the corresponding media. Following overnight incubation to facilitate attachment of the cells, the media was replaced with DMSO-free media.

**Table 1: Description of used human cell lines and corresponding media composition**

<b>Cell line</b>	<b>Description</b>	<b>Medium</b>
MCF7 Wildtype (WT) T47D Wildtype (WT)	Luminal A breast cancer cell lines	DMEM media supplemented with 10% FBS, $10^{-8}$ M E2, 1% P/S
MCF7 Long-term estrogen-deprived (LTED) T47D Long-term estrogen-deprived (LTED)	Luminal A breast cancer cell lines resistant to estrogen deprivation, mimicking aromatase inhibition	DMEM phenol red-free supplemented with 10% CSFBS, 1% P/S, 1% sodium pyruvate, 1% L-glutamine
MCF7 LTED <i>GLYATL1</i> knockout (KO)	<i>GLYATL1</i> knockout cell lines generated by CRISPR-Cas9 approach	
MCF7 <i>GLYATL1</i> overexpression (OE) T47D <i>GLYATL1</i> overexpression (OE)	Luminal A breast cancer cell lines stability overexpressing <i>GLYATL1</i>	DMEM media supplemented with 10% FBS, $10^{-8}$ M E2, 1% P/S, 1µg/ml Blasticidin
MCF7 WT BioID2 constructs	Stable cell lines harboring BioID2 plasmids	DMEM media supplemented with 10% FBS, $10^{-8}$ M E2, 1% P/S, 1µg/ml Puromycin
HEK239 FT	Fast growing, highly transfectable human embryonic kidney cells	DMEM media supplemented with 10% FBS, 1% NEAA, 1% Geneticin, 1% P/S

### 3.2.1.2 Generation of stable Cell Lines

Stable cell lines were generated by the DKFZ Cellular Tools Core Facility via viral transduction. Subsequently, cells were selected with either 1 µg/mL blasticidin or puromycin for integration of plasmid.

### **3.2.1.3 Generation of Single-cell Clones**

*GLYATL1* knockout cell lines were generated by Dr. Emre Sofyali using the CRISPR-Cas9 approach with a single guide RNA targeting exon 4. I used this pool to generate cell lines with a clonal background. With the help of the DKFZ Cellular Tools Core Facility, single cells were spotted using the F.SIGHT™ dispenser into a poly-L-lysine coated 96-well plate. The single-derived clones were expanded and transferred to bigger wells. After the cells had been expanded into the 6-well format, genomic DNA was purified and the sequence around the sgRNA binding site was PCR-amplified, purified, and Sanger sequenced.

### **3.2.1.4 Cell Proliferation Assay**

Cell growth was analyzed via Hoechst 33342 staining. To this end, 500 cells were seeded in 150 µL per well into 96-well black plates. Following overnight incubation to allow the cells to attach, the media was aspirated, and cells were washed before adding fresh corresponding media. Seeding control was assessed by staining the cells with 20 mM Hoechst 33342 (final dilution 1:5,000) for 30 min. Proliferation was monitored over the indicated amount of days, after which cells were stained with Hoechst 33342. Cell numbers were quantified by microscopy-based nuclei counting using the ImageXpress Micro Confocal microscope and the Molecular Device Software. Proliferation rates were normalized to the seeding control.

### **3.2.1.5 Inhibitor Treatments**

Dose-response curves were performed to calculate the IC<sub>50</sub> values for Gracinol (KAT2B inhibitor [146]) and TMP269 (HDAC5/9 inhibitor [147]). To this end, cells were seeded into a 96-well black plate with a density of 500 cells per well. On the next day, media was aspirated and replaced by media containing a 1:3 dilution series of the inhibitor, solved in DMSO. To diminish the toxic effect of the solvent, concentrations were selected in a way that total DMSO concentration remained under 0.2%. Proliferation was analyzed after 8 days of inhibitor treatment and normalized to cells treated with DMSO.

### 3.2.1.6 Transfection

Knockdowns were performed in 6-well plates using siRNAs targeting *GLYATL1*, *FOXA1*, *ESR1* or *KAT6B*. Therefore,  $2 \times 10^6$  cells ( $2.5 \times 10^5$  cells for T47D LTED) were seeded 24 hours prior transfection. After overnight incubation, to allow the cells to attach, the medium was aspirated, cells were washed with PBS and 1.5 mL P/S-free media was added per well. Cells were transfected with a final concentration of 3 nM siRNA and Lipofectamin RNAiMAX. To this end, siRNA was mixed with Opti-MEM™ with a total volume of 250  $\mu$ L per well. Additionally, 4  $\mu$ L RNAiMAX was diluted in 246  $\mu$ L of Optimem separately. Both mixtures were combined 1:1 and incubated for 5 minutes before adding 500  $\mu$ L of the transfection mix to the cells droplet-wise. Cells were incubated for 72 hours before evaluating the knockdown efficiency and the cellular effect.

Whole plasmids were transfected in HEK293FT using polyethylenimine (PEI). To this end, cells were trypsinized and  $1.5 \times 10^6$  cells were diluted with 9 mL fresh growth media. In parallel, 1 mL serum-free media was supplemented with 4  $\mu$ g DNA and 20  $\mu$ L 1 mg/mL PEI solution and incubated for 15 minutes at room temperature. Afterward, the transfection mixture was added to the prediluted cells and distributed into a 100 mm dish or 6-well plate and incubated at 37°C and 5% CO<sub>2</sub>. After 24 hours of transfection, the media was changed to new growth media and further incubated for additional 24 hours.

Plasmid DNA transfection in MCF7 was carried out using Lipofectamin™ 2000. To this end, 250,000 cells per well were plated into 6-well plates. On the next day, 6  $\mu$ L Lipofectamin™ 2000 in 150  $\mu$ L Opti-MEM™ media was mixed with 2,500 ng DNA in 150  $\mu$ L Opti-MEM™ media and incubated for 25 minutes at room temperature. In the meantime, cells were washed with PBS and 700  $\mu$ L of P/S-free media was added to each well. After the 25 minutes incubation time, the DNA-lipid complex was added to the cells. Following 5 hours of incubation, the media was aspirated and replaced by full-growth media. The transfected cells were analyzed after 48 hours.

### 3.2.2 Analysis of Genomic DNA

#### 3.2.2.1 Cell Lysis

Cells were grown in 48-well plates until a confluency of 60-70% was reached. Growth media was aspirated and cells were frozen down at  $-80^{\circ}\text{C}$  to facilitate cell lysis. Cells were lysed in 200  $\mu\text{L}$  lysis buffer (Table 2), transferred into a 1.5 mL reaction tube and incubated for 30 minutes at  $56^{\circ}\text{C}$ . Subsequently, enzymes were inactivated by incubation at  $96^{\circ}\text{C}$  for 5 minutes. DNA was stored at  $-20^{\circ}\text{C}$  until further usage.

**Table 2: Composition of Lysis Buffer for genomic DNA isolation**

Reagent	Volume [ $\mu\text{L}$ ]
5x Phusion HF Buffer	40
Proteinase K [20 mg/mL]	10
RNase A [100 mg/mL]	1
Nuclease-free water	149

#### 3.2.2.2 Amplification of Gene Sequence via Polymerase Chain Reaction and Visualization of PCR Amplicon

The region around exon four of the *GLYATL1* gene was PCR-amplified to evaluate the base pair deletion generated by CRISPR-Cas9 editing. To this end, 10  $\mu\text{L}$  of lysed cells were used as input, supplemented with Phusion-PCR master-mix (Table 3), and incubated using the thermocycler protocol shown in Table 4.

**Table 3: Composition of Phusion PCR master mix**

Reagent	Volume [ $\mu\text{L}$ ]
5x Phusion HF Buffer	10
10 mM dNTPs	1
Forward Primer [10 $\mu\text{M}$ ]	2
Reverse Primer [10 $\mu\text{M}$ ]	2
50 mM $\text{MgCl}_2$	0.5
Phusion Hot Start	0.5
Nuclease-free water	24

**Table 4: Phusion PCR thermocycler protocol**

Temperature [°C]	Time	Cycles
98	2 min	
98	10 s	
64	20 s	35 cycles
72	1 min	
72	10 min	
4	∞	

5 µl of the PCR fragments were supplemented with 1 µL 6x Orange Loading Dye and run on 1% Agarose gel in 1x TAE for 1 h at 100 V. 5 µL of O'Generuler 100 bp DNA Ladder plus was used as a size standard. Gel was stained in an ethidium bromide bath (10 µg/mL) for 15 minutes and DNA was visualized using the Herolab Gel Documentation System.

### 3.2.2.3 PCR Product Purification

The PCR product was purified using the Wizard SV Gel and PCR Clean-up System according to the manufacturer's instructions. DNA fragments were eluted in nuclease-free water and concentration was measured with the Nanodrop ND-1000 UV-Vis Spectrophotometer.

### 3.2.2.4 Sanger Sequencing

The purified PCR product was sent for Sanger sequencing to Eurofins Genomics. Sequence alterations were analyzed using the SnapGene software version 7.2.

### 3.2.3 Analysis of RNA Expression

#### 3.2.3.1 RNA Isolation

RNA was isolated using the RNeasy Mini Kit according to the manufacturer's instructions. Additionally, DNA was digested on-column using RNase-free DNase, and purified RNA was eluted in nuclease-free water. RNA concentrations were measured with the Nanodrop ND-1000 UV-Vis Spectrophotometer.

#### 3.2.3.2 Reverse Transcription

Purified mRNA was reverse transcribed into cDNA utilizing the RevertAid RT Reverse Transcription Kit. Initially, 1  $\mu\text{g}$  of mRNA was combined with 1  $\mu\text{L}$  oligo-dT primer filled up with nuclease-free water to a total volume of 12  $\mu\text{L}$ . Following incubation at 65°C for 5 minutes, the mixture was placed on ice and mixed with the reverse transcription reaction master mix (Table 5). The cDNA synthesis was run as described in Table 6.

**Table 5: Reverse Transcription master mix**

Reagent	Volume per reaction [ $\mu\text{L}$ ]
5x Reaction Buffer	4
RiboLock RNase Inhibitor [20 U/ $\mu\text{L}$ ]	1
10 mM dNTP Mix	2
RevertAid Reverse Transcriptase [200 U/ $\mu\text{L}$ ]	1

**Table 6: Reverse Transcription thermocycler protocol**

Temperature [ $^{\circ}\text{C}$ ]	Time
37	5 min
42	1h
70	10 min
4	$\infty$

### 3.2.3.3 Quantitative Reverse Transcription Polymerase Chain Reaction (RT-qPCR)

A total of 10 ng of cDNA in a total volume of 5  $\mu$ L was transferred into a 384-well plate. Subsequently, 6  $\mu$ L of real-time qPCR master mix (Table 7) was added and measurement was taken on the Quantstudio 5 using the protocol shown in Table 8. Relative fold gene expressions were calculated using the  $\Delta\Delta C_t$  method ( $2^{-\Delta\Delta C_t}$  algorithm).  $C_T$  values were normalized to the housekeeping genes *ACTB* and *Pum1*.

**Table 7: Real-time qPCR master mix**

Reagent	Volume per reaction [ $\mu$ L]
2x SYBR Green PCR Master mix	5.5
Forward Primer [20 $\mu$ M]	0.2
Reverse Primer [20 $\mu$ M]	0.2
Nuclease-free water	0.1

**Table 8: Real-time qPCR thermocycler protocol**

Temperature [ $^{\circ}$ C]	Time	Cycles
50	2 min	
95	15 min	
95	15 s	45x
60	1 min	
95	15 s	
60	1 min	0.075 $^{\circ}$ C/s
95	15 s	

### 3.2.3.4 RNA Sequencing

RNA sequencing was performed in the NGS Core Facility at the DKFZ on Illumina NovaSeq 6000 S1 to obtain an average of ~58 million read pairs per sample. Initial data analysis and mapping were performed by Dr. Birgitta Michels and Dr. Verônica Rodrigues de Melo Costa. First quality score filtering, poly-A trimming, artifact removal,

removal of 'N' containing reads, and clearing of rRNA contamination were performed using EvalRSeq, a pipeline provided by the HUSAR platform from DKFZ. Subsequently, strand-specific reads were mapped to the human reference genome GRCh38.13 (STAR version 2.3.) with an index built on gencode v34 [148]. The read quality of the raw gene expression data was determined using the FASTQC tool [149]. DeepTools2.0 [150] was used to assess the genome-wide similarity of the sequencing replicates. The reads mapping to each gene were counted using htseq-count from HTSeq 0.11.1 [151].

### **3.2.3.5 Pathway Activity Estimation**

Pathway activity for 14 key biological pathways was estimated using the Pathway Responsive GENes for Activity Interference (PROGENy) R package (version 1.26.0) [152, 153]. This method utilizes consensus gene signature for each pathway developed from high-throughput perturbation experiments to infer pathway activity from gene expression data. Enrichment analysis was conducted using decoupeIR package (version 2.8.0) with default parameters. Limma t-values were used as input, indicating differential expression between the compared cell lines.

### **3.2.3.6 Transcription Factor Activity Estimation**

DoRothEA (version 1.16.0) was used to predict transcription factor activity from expressing data providing insights into the regulatory network in the different cell lines [153-155]. This computational tool gene relies on a comprehensive collection of known targets for a broad set of transcription factors, with targets characterized based on the levels of evidence. Gene-level statistics were obtained using limma t-values, indicating differential expression between the compared cell lines. These statistics served as input for the decoupeIR package (version 2.8.0), which integrates the DoRothEA regulations to estimate transcription factor activity scores. Transcription factors with at least 25 targets detected were displayed.

### **3.2.3.7 Gene Set Enrichment Analysis**

Gene Set Enrichment Analysis (GSEA) was performed to comprehensively assess the biological processes and pathways enriched in the gene expression data using the GSEA software from Broad Institute (version 4.1.0) [156, 157]. Differential gene expression between two different cell lines was used to generate a pre-ranked gene list, including gene names and log<sub>2</sub> fold change values. GSEA was run with 1,000 permutations, without collapsing gene sets, and using gene sets from the Molecular Signatures Database (MSigDB) version v2023.2.Hs.

### **3.2.4 Analysis of Protein Expression**

#### **3.2.4.1 Protein Isolation**

Proteins were isolated from cells growing in 100 mm or 6-well plates. To this end, culture plates were directly placed on ice, and media was aspirated. After washing with PBS, residual PBS was aspirated and lysis buffer (60 µL for 6-wells, and 120 µL for 100 mm dishes) was added. Cells were detached using a cell scraper and transferred into a 1.5 mL reaction tube. After an incubation step at 4°C for 30 minutes at a vertical rotor, lysates were centrifuged for 15 minutes at 15,000 g and 4°C. The supernatant containing the soluble proteins was transferred into a new 1.5 mL reaction tube and stored at -80°C until further usage.

#### **3.2.4.2 Protein Quantification**

Protein concentrations were determined using the Pierce™ BCA Protein Assay Kit according to the manufacturer's instructions. The colorimetric readout was measured with the GlowMax Discover system and quantified using a BSA serial dilution standard curve.

#### **3.2.4.3 Sodium Dodecyl Sulfate-Polyacrylamide Gel Electrophoresis**

Proteins were separated based on their molecular weight using sodium dodecyl sulfate-polyacrylamide gel electrophoresis (SDS-PAGE). To this end, 30 µg protein was diluted with water and supplemented with a final concentration of 1x Roti®-Load 1.

Proteins were denatured at 95°C for 15 minutes and loaded on a Mini-PROTEAN TGX Stain-Free™ precast gel. Additionally, 5 µL of PageRuler™ Prestained Protein Ladder were loaded for size determination. Electrophoresis was conducted in 1x running buffer at 130 V for 70 minutes.

#### **3.2.4.4 Western Blotting**

Following size-separating the proteins via SDS-PAGE, the proteins were transferred to a polyvinylidene fluoride (PVDF) membrane using the Trans-BlotR Turbo™ Transfer System. To this end, the Trans-Blot Turbo™ PVDF Transfer Kit was used according to the manufacturer's instructions. The protein were transferred on the PVDC membrane at 1.3 A, 25 V for 7 minutes. Subsequently, unspecific binding sites were blocked by incubating the membrane with blocking buffer for 1 hour. Afterward, the membrane was incubated with diluted primary antibody in blocking buffer overnight at 4°C. Following three washing steps with TBST for 5 minutes each, the membrane was incubated with the corresponding fluorophore-coupled secondary antibody diluted in TBST for 1 hour. Excessive antibodies were removed in three washing steps using TBST. Fluorescence signal was captured using the Odyssey Infrared Imaging System and blots were further processed using the Image Studio Lite software.

#### **3.2.4.5 Immunofluorescence Imaging**

Immunofluorescence imaging was conducted to examine the expression and localization of GLYATL1. To this end,  $2.5 \times 10^5$  cells were seeded on top of 12 mm coverslips in a 6-well plate. After reaching 70-80% confluency, cells either directly underwent fixation or were stained beforehand with 500 nM abberior LIVE ORANGE mito for 1 hour at 37°C and 5% CO<sub>2</sub>. Cells were fixed with 4% paraformaldehyde for 15 minutes at room temperature. After fixation, cells were washed trice with PBST for 5 minutes each and permeabilized with 0.1% Triton X-100 in PBS for 10 minutes to allow antibody penetration. Coverslips were washed trice with PBST and non-specific bindings sites were blocked by incubating cells with 3% BSA in PBS for 1 hour at room temperature. Primary antibodies were diluted in 3% BSA and added to the cells. Following overnight

incubation, the cells were washed with PBST trice to remove unbound antibodies. Secondary antibodies conjugated to a fluorophore (1:400 in BSA) were added and incubated for 1 hour at room temperature in the dark. After washing off excess secondary antibodies with PBS, cells were either stained with additional antibodies or mounted onto glass slides using ProLong Diamon antifade containing DAPI for nuclear staining. The samples were examined under a fluorescence microscope using either Cell Observer or LSM-900 (Zeiss). Negative controls (no primary or secondary antibody) were used to verify specificity and antibody reactivity. Analysis was performed using the Zenn Blue software and ImageJ.

### **3.2.4.6 Generation of a Monoclonal GLYATL1 Antibody**

Specific monoclonal antibody targeting GLYATL1 was generated in cooperation with the Antibodies Core Facility at the DKFZ. To this end, mice were injected with 1 mg KLH-coupled peptide (ENEDSRRFVGQFGFFEASC, Peptide Specialty Laboratories GmbH). Immunization was repeated in total six times once a week. Sera were tested for protein recognition on Western Blot using lysates of transfected HEK293FT cells transiently expressing Flag-tagged GLYATL1. Mice with specific GLYATL1 antibodies in sera were sacrificed and lymphocytes were extracted from blood. To this end, blood was incubated for one hour at 37°C to coagulate followed by 20 minutes centrifugation at 21,460 g at room temperature. Additionally, lymphocytes were isolated by crushing isolated lymph nodes to separate cells.

Isolated lymphocytes were subsequently fused to myeloma cancer cells to generate hybridoma. To this end SP 2/0 cells and lymphocytes were each pelleted at 150 g for 10 minutes at room temperature and media was aspirated afterward. Cell pellets were combined in 1,5 mL PEG and were added slowly under continuous agitation to open the cell membrane. RPMI was added droplet-wise to close the cell membranes and therefore facilitated the fusion of lymphocytes with the myeloma cells. To increase fusion efficiency, RPMI was added with a flow rate of 1 mL in the first 2 minutes, followed by 3 mL within 1 minute and subsequently, 16 mL in 3 minutes. Afterward, cells were centrifuged for 10 minutes at 150 g at room temperature. After 5 minutes of incubation time, the supernatant was carefully aspirated and cells were plated in 96-well plates with 200 µL/well. After four to seven days, the supernatants were tested for protein

recognition on Western Blot. “Mother” clones with specific GLYATL1 binding were deconvoluted in the Cellular Tools and Clone Repository core facility at the DKFZ using the F.SIGHT™ dispenser. The specificity of the different “daughter” clones was screened via immunofluorescence and Western Blot. Antibodies displaying specific GLYATL1 binding were purified via the hiTRAP Protein G HP column using the manufacturer’s protocol.

#### **3.2.4.7 Analysis of Protein-Protein Interaction**

Protein-protein interaction was studied using the BioID2 approach [158]. To this end,  $2 \times 10^6$  stable cells expressing either rwpMXs\_MCS\_MYC\_Linkers\_BioID2 IRES-Puro or rwpMXs\_GLYATL1\_MYC\_Linkers\_BioID2 IRES-Puro plasmid were seeded in 100 mm plates. Following incubation for 24 hours at 37°C and 5% CO<sub>2</sub>, 50 μM biotin was added to the cells and further incubated for additional 24 hours. Afterward, plates were directly placed on ice, and cells were washed once with PBS. After aspirating the remaining buffer, cells were lysed with 500 μL ice-cold NP-40 lysis buffer and scraped into a pre-chilled 1.5 mL reaction tube. The lysates were centrifuged at 15,000 g, 4°C for 10 minutes and the supernatant was transferred into a new tube. The protein concentration was measured and adjusted to 2 μg/μL with NP-40 lysis buffer.

In the meantime, a 1 mL spin column was activated with 200 μL PBS and loaded with 100 μL High Capacity Streptavidin Agarose resin, followed by three washing steps with 250 μL PBS. The remaining liquid was removed by centrifugation at 500 g for 1 minute. Afterward, the column was plugged and 500 μL of the prepared protein samples were loaded on the column and allowed to enter the resin. The mixture was incubated for 30 minutes at room temperature with end-over-end mixing. Afterward, the plug was removed, and the column was centrifuged at 500 g for 1 minute, followed by five washing steps with 250 μL PBS. Biotinylated proteins were eluted with 100 μL 2x non-reducing Lane Marker sample Buffer and 2 mM biotin at 95°C for 5 minutes. Eluate was collected in a new 1.5 mL tube by centrifugation at 1,000 g for one minute.

### **3.2.5 Proteomic Analysis via Mass Spectrometry**

Mass spectrometry measurements were carried out in collaboration with Luisa Schwarzmüller. Protein lysates were prepared as described in 3.2.4.1 using a lysis buffer supplemented with 10 mM NaF, 1 mM Na<sub>3</sub>VO<sub>4</sub>, 150 U/mL Benzonase and 10 U/mL RNase-free DNase. Further sample preparation and measurement (3.2.5.1-3.2.5.3) was performed by Luisa Schwarzmüller.

#### **3.2.5.1 SP3 Sample Preparation**

Single-pot solid-phase sample preparation (SP3) [159] was conducted using 20 µg of protein in a total volume of 60 µL of RIPA buffer, supplemented with 100 mM TEAB. CAA and TCEP were added to a final concentration of 40 mM and 10 mM, respectively. Protein alkylation and reduction were carried out at 95°C for 5 min. Subsequently, 1 µL of each paramagnetic beads (Sigma-Aldrich #45152105050250 and #65152105050250) were mixed 1:1. Ethanol to a final concentration of 50% was added and incubated for 15 minutes at 650 rpm. To facilitate bead-protein binding, the mixture was incubated on a shaker at 650 rpm at room temperature for 15 minutes. The bound proteins were then washed twice with 80% ethanol, followed by a single wash with 100% acetonitrile. After aspirating the remaining acetonitrile, the beads were resuspended in 100 mM TEAB containing trypsin at a protease: protein ratio of 1:25. Digestion was facilitated by sonication in a water bath for 30 seconds, followed by incubation at 37°C, 800 rpm for 16 hours. The next day, the supernatant containing digested peptides was collected and vacuum-dried at 30°C, 1300 rpm. Peptides were stored at -20°C until measurement.

#### **3.2.5.2 Liquid chromatography–mass spectrometry (LC-MS) Measurement**

Peptides were solved in MS-grade water supplemented with 0.1% trifluoroacetic acid (TFA) and 2.5% hexafluoroisopropanol (HFIP) before measurement. Using the Ultimate 3000 liquid chromatography (LC) system, 1 µg peptides were separated on a 25 cm column (Waters nanoEase™ BEH C18 130Å, 1.7 µm, 75 µm x 250 mm, Cat. 186008795). A 100-minute linear gradient of 4-30% acetonitrile at a flow rate of

300 nL/min, reaching a total method time of 120 minutes, was utilized for peptide separation. Mass spectrometric analysis was carried out with the Orbitrap Exploris 480. MS1 scans were acquired at a resolution of 120,000, with an AGC target set to  $3e^6$  ions. MS2 spectra were obtained in 47 isolation windows of variable width, covering 400 – 1000 m/z at a resolution of 60,000 and an AGC target of  $1e^6$ . Peptides were fragmented with a collision energy of 28%.

Peptides and proteins were identified and quantified with Spectronaut (version 15.6) using the proteome-wide human fasta file from UniProt. Protease trypsin was set and up to two missed cleavage sites were allowed. Modifications were set with Carbamidomethylation (C) as fixed, Oxidation (M), and Acetylation (N-terminus) as variable modifications. Peptides were quantified on the MS2 level by summing up the signal area of the 3-6 best fragments.

Data was further analyzed using the Perseus software (version 1.6.2.3). The data set was log<sub>2</sub>-transformed and unpaired two-sample t-tests were performed with permutation-based FDR correction with 250 shuffles. Data was filtered for significant changes with a p-value of 0.05 and an absolute fold-change  $\geq 2$ .

### 3.2.5.3 Parallel Reaction Monitoring

For Parallel Reaction Monitoring (PRM) MS measurement, the same LC and MS1 parameters as for DIA were used. The MS2 spectra were acquired for pre-selected peptides of GLYATL1 at a resolution of 120,000.

Data analysis was performed using Skyline (version 3.1.0.7312) [160]. GLYATL1 protein fasta files were imported from Uniprot (Q969I3) and *in silico* digested with trypsin allowing one missed cleaving site. Y and b fragment ions revealed filtered peptides for the three pre-measured GLYATL1 peptides. The retention time of R.ALLLVTEDILK.L peptide peaks was identified using a spectrum of MCF7 GLYATL1 overexpressing cell line and applied to all samples. The peak areas were calculated by setting peak boundaries and summing the fragment areas.

### **3.2.6 Quantification of Intracellular Oxidative Stress**

#### **3.2.6.1 Flow Cytometry Analysis of Intracellular Reactive Oxygen Species Levels**

To assess the intracellular oxidative stress levels, 500,000 cells were stained with 5  $\mu$ M CellROX Oxidative Stress reagent in full growth media for 30 minutes at 37°C. Subsequently, cells were centrifuged for 5 minutes at 1,500 g and the resulting cell pellet was resuspended in PBS. The cells were transferred into FACS tubes for analysis with a FACSCalibur flow cytometer. To ensure data quality, living cells were gated based on the forward scatter (FSC) and side scatter (SCC) characteristics. The fluorescence signal in the FL3 channel representing the reactive oxygen species (ROS) sensor was measured. The mean fluorescence intensity of the FL3 channel was analyzed using the Flowing software version 2.5.1.

#### **3.2.6.2 Fluorescent Monitoring of Hydrogen Peroxide Levels**

Cytoplasmic and mitochondrial hydrogen peroxide ( $H_2O_2$ ) levels within living cells were monitored using stable cell lines expressing the roGFP-ORP1 sensor. This sensor is a fusion of roGFP, a redox-sensitive variant of the green fluorescent protein (GFP), and Opr1, a yeast peroxidase with high specificity towards  $H_2O_2$  [161]. Upon oxidation, roGFP shifted the excitation spectrum from ~488 nm to ~405 nm.

The functionality of the sensor was tested via flow cytometry. To this end, 250,000 cells were seeded in 6-well plates. On the next days, cells were trypsinized and centrifuged for 5 minutes at 1,500 g. The cell pellet was resuspended in PBS and transferred into FACS tubes. Cells were analyzed using FACSCalibur flow cytometer with the FL3 channel covering the spectrum of the reduced sensor. Living cells were gated based on the forward scatter (FSC) and side scatter (SCC) characteristics. Signal intensities were analyzed using the Flowing software version 2.5.1.

To determine the redox status of the sensor, cells were seeded into 96-well-white plates with 20,000 cells per well one day prior analysis. Fluorescence intensity was measured using the GloMax Discover plate reader. The redox-sensitive response of

roGFP-Orp1 was measured with excitation wavelengths of 405 nm and 475 nm. Emission was detected at 500-550 nm. The background signal of unstained cells was subtracted, and the ratio of fluorescence intensities (405 nm/475 nm) was calculated to determine the redox status.

### **3.2.7 Metabolomics Measurement**

1\*10<sup>6</sup> cells were seeded and allowed to attach overnight. After the media was aspirated, cells were washed with cold 154 mM ammonium. The residual buffer was removed, and the plates were rapidly immersed in liquid nitrogen. The frozen plates were transferred to -80°C until further usage. Consecutive metabolite extraction and mass spectrometry (3.2.7.1-3.2.7.2) were performed by Dr. Lisa Schlicker from the Almut Schulze Lab (DKFZ).

#### **3.2.7.1 Metabolite Extraction**

For extraction of polar metabolites, cells were once again washed with ice-cold 154 mM ammonium acetate. Subsequently, cells were scraped off in 0.5 mL ice-cold MeOH/H<sub>2</sub>O/Acetonitrile (50/20/30 v/v) containing internal standards, including stable isotope labeled amino acids and <sup>13</sup>C<sub>3</sub>-Malonyl-CoA as well as deuterium labeled tricarboxylic acid (TCA) cycle intermediates. After vortexing and sonication, samples were centrifuged at 13,000 g for 5 minutes and the resulting supernatant was applied onto a C18 8B-S001-DAK solid phase column, which has been previously activated using acetonitrile and equilibrated using methanol/water/acetonitrile (50/20/30 v/v). The remaining pellet underwent an additional extraction using 0.5 mL ice-cold methanol/water/acetonitrile (50/20/30 v/v). The eluate was then dried overnight in a refrigerated vacuum concentrator at 10°C. On the next day, the residual pellet was dissolved in 0.2 M sodium hydroxide and incubated for 20 min at 95°C and protein concentrations were quantified by BCA assay.

### 3.2.7.2 LS-MS Measurement

LC-MS measurement was conducted on an Ultimate 3000 system coupled to a Q Exactive Plus mass spectrometer. Dried metabolite extracts were dissolved in 100  $\mu$ L 5 mM ammonium acetate in acetonitrile-water solution (75/25, v/v). 3  $\mu$ L of the samples were applied onto an amide-HILIC column (2.6  $\mu$ m, 2.1x100 mm) with a constant temperature of 30°C. Subsequently, two different solvents were used for elution. Solvent A consists of 5 mM ammonium acetate in acetonitrile-water solution (5:95, v/v), and solvent B consisting of 5 mM ammonium acetate in acetonitrile-water solution (95:5, v/v). Gradient elution was applied with 98% solvent B for 2 min, followed by a linear decrease to 40% solvent B within 5 min. 40% of solvent B was maintained for 13 min, then returning to 98% solvent B within 1 min and maintaining 98% solvent B for 5 min for column equilibration before each injection. The flow rate was set at 350  $\mu$ L/min.

The eluent was directed to the HESI source from 1.5 min to 21.0 min post-sample injection with a sheath gas flow rate of 30 units, auxiliary gas flow rate of 10 units, a spray voltage of 3.6 kV (positive mode)/ 2.5 kV (negative mode), a capillary temperature of 320 °C and a S-lens RF level of 55.0 V.

Detection of different acyl-CoAs was acquired in positive mode with a scan range from 760 to 1100 m/z, a resolution of 70,000, an AGC target of  $1e^6$ , and a maximum injection time of 50 ms. For data-dependent MS2 (ddMS2), the resolution was set to 17,500, AGC target to  $5E4$ , stepped collision energies of 20, 50, and 80, and maximum injection time of 50 ms.

Detection of water-soluble metabolites was acquired in polarity switching mode within the scan range of 69-1000 m/z, with otherwise similar settings and ddMS2.

Peaks corresponding to the calculated metabolite masses, sourced from an in-house metabolite library, were integrated utilizing the EI-MAVEN software. The identification of metabolite was supported by fragmentation patterns [162]. Peak intensities were normalized by their respective internal standard and protein levels.

### 3.2.7.3 Data Analysis

Initial data processing was performed using the web-based platform MetaboAnalyst 5.0 [163]. The data was transformed using one-factor statistical analysis using a post hoc one-way ANOVA test. Pathway enrichment analyses were performed with significant ( $p < 0.05$ ) log<sub>2</sub> fold, respectively.

### 3.2.8 Analysis of Epigenetic Profile - EpiTOF

Epigenetic changes were addressed by cytometry by time-of-flight (CyTOF) to analyze a wide panel of histone modifications.

#### 3.2.8.1 Antibody Conjugation

Antibodies were conjugated to different metals by people from the lab of Moshe Oren, by Efrat Shema, Tomer-Meir Salame, or me using the Antibody Labelling Kit v3 by IONpath according to the manufacturer's instructions. An antibody panel was chosen to minimize spillover and noise between the different channels.

#### 3.2.8.2 Sample Preparation

MCF7 WT, LTED, and two different *GLYATL1* knockout cell lines were harvested and  $4 \times 10^6$  ( $2 \times 10^6$  in batch 1) cells per sample were centrifuged at 1,200 g for 5 minutes. To reduce cell loss, the pellet was resuspended in 200  $\mu$ L CyTOF PBS and transferred to a pre-coated canonical 96-well. The coating was performed with CyTOF staining buffer for at least 30 minutes. After centrifugation at 300 g for 5 minutes at room temperature, dead cells were stained with 100  $\mu$ L 1.25  $\mu$ M Cisplatin in CyTOF PBS and incubated for 30 seconds. The reaction was quenched by adding 100  $\mu$ L DMEM + 10% FBS prewarmed to 37°C and centrifuged for 15 minutes at 300 g. After aspirating the supernatant, the pellet was washed once with 200  $\mu$ L CyTOF staining buffer and centrifuged at 300 g for 5 minutes. The cell pellet was gently resuspended in a mixture of the extracellular antibodies diluted in 50  $\mu$ L/sample CyTOF staining Buffer and incu-

bated for 30 minutes at room temperature for staining extracellular proteins. After staining, the plate was centrifuged for 5 minutes at 300 g and washed twice with 200  $\mu$ L CyTOF staining Buffer. Thereafter, cells were resuspended in CyTOF nuclear antigen staining buffer working solution and incubated for 30 minutes at room temperature while mixing the solution every 10 minutes. After centrifugation for 5 minutes at 700 xg, the pellet was washed twice with 200  $\mu$ L CyTOF nuclear antigen staining perm, followed by resuspending the cell pellet in 150  $\mu$ L CyTOF nuclear antigen staining perm containing 1  $\mu$ L of a unique barcode for each sample. The solution was mixed immediately and incubated for 1 hour, mixing every 15 minutes to ensure complete barcoding. After two washing steps with 150  $\mu$ L CyTOF staining buffer, the cells were counted and equal amounts of cells per sample ( $1 \times 10^6$  cells batch 1,  $2 \times 10^6$  cells batch 2) were combined and distributed to new wells of the 96-well plate with a density of  $3 \times 10^6$  cells/well. The plate was centrifuged once again, and the cells were stained with a cocktail of intracellular and nuclear antibodies in a final volume of 100  $\mu$ L with a Nuclear Staining Buffer working solution. After 30 minutes of incubation time, cells were washed with 100  $\mu$ L CyTOF staining buffer twice and subsequently fixed with freshly prepared 200  $\mu$ L 4% paraformaldehyde in CyTOF PBS overnight. On the next day, the plate was centrifuged for 5 minutes at 700 g and cells were stained with 150  $\mu$ L of 125 nM iridium solution in 4% paraformaldehyde solution for 45 minutes. After centrifuging the plate at 700 xg for 5 minutes, cells were washed twice with CyTOF staining buffer followed by two washing steps with CyTOF CAS+. The cells were transferred into a 15 mL tube and acquired in a total volume of 50  $\mu$ L on the same day.

### **3.2.8.3 Sample Measurement**

Sample measurement was performed in the Life Science Core Facility for Mass Cytometry by Dr. Tomer-Meir Salame via a Fluidigm CyTOF Helios platform. Data was cleaned up by gating for intact live single cells. Additionally, cells with low core histone reads (<5) were filtered out and the barcoded cells were deconvoluted.

#### **3.2.8.4 CyTOF Data Analysis**

Analysis of the CyTOF data was performed by Dr. Eviatar Weizman and Luisa Schwarzmüller based on an R-based pipeline [164]. Briefly, the data was arcsinh transformed and regressed to H3 and H3.3 expression. Due to the low performance of the antibody detecting H3K9 acetylation, data from this antibody was excluded before z-scaling. Subsequently, clustering was performed based on the histone markers.

### **3.2.9 Data Analysis**

#### **3.2.9.1 Analysis of Publicly Available Data Sets**

To analyze patient survival, two comprehensive cancer datasets, The Cancer Genome Atlas (TCGA) and the Molecular Taxonomy of Breast Cancer International Consortium (METABRIC), were used.

For Kaplan-Meier survival analysis, clinical and survival data from TCGA were extracted. Patient groups were defined based on their molecular subtype and ranked based on their *GLYATL1* expression. The survival rate was compared using Kaplan-Meier curves. The log-rank test was used to assess statistical significance between the patient groups. Survival analysis of the METABRIC data set was performed using the web-based Km-plotter [165].

#### **3.2.9.2 Statistical Analysis**

Statistical analysis was performed using the GraphPad Prism version 5. Unless otherwise mentioned, data is presented as mean  $\pm$  standard error of the mean, each dot representing data of an independent biological replicate. P values  $\leq 0.05$  were considered statistically significant. P values  $\leq 0.05$ , 0.01, and 0.001 are indicated by one, two, or three asterisks respectively.

## 4 Results

### 4.1 *GLYATL1* Expression is Increased in Aromatase Inhibitor-Resistant Cell Lines

The Luminal A breast cancer subtype is characterized by high estrogen receptor expression and generally responds well to endocrine therapies such as tamoxifen or aromatase inhibitors. However, the development of resistance to this therapy approach is a severe clinical problem, leading to disease recurrence and progression. Understanding the mechanisms of resistance to endocrine therapy is thus important for developing new therapeutic strategies to effectively overcome resistance and improve the prognosis of patients.

To investigate endocrine therapy resistance *in vitro*, two luminal A breast cancer cell lines, MCF7 and T47D, were chronically deprived of estrogen for twelve months to mimic the effect of aromatase inhibition and to stimulate resistance acquisition. These long-term estrogen-deprived (LTED) models were kindly gifted by Prof. Dr. Luca Magnani (ICL London, MCF7) or generated in-house by two previous PhD students, Dr. Emre Sofyali and Dr. Simone Borgoni (T47D) [130, 131]. ATAC- and RNA-sequencing, conducted by Dr. Emre Sofyali, identified glycine-N-acyltransferase like 1/glutamine-N-acyltransferase (*GLYATL1*) as one of the most highly upregulated genes in resistant cell lines [131].

To validate the upregulation of *GLYATL1* observed in the sequencing data, I performed RT-qPCR on LTED and parental wildtype (WT) MCF7 and T47D cells. The analysis confirmed a significant increase in *GLYATL1* mRNA levels in LTED cells compared to wildtype by approximately 200-fold in MCF7 and 30-fold in T47D (Figure 10A). Furthermore, *GLYATL1* protein levels in MCF7 cell lines were assessed using a PRM-based targeted mass spectrometry approach, in collaboration with Luisa Schwarzmüller. Specific fragments corresponding to a single *GLYATL1* peptide (ALLVETEDILKL) were detected. While only marginal *GLYATL1* levels could be detected in the MCF7 wildtype cell line, the summed signal intensity levels significantly increased in LTED cells (Figure 10B). These results indicate that both *GLYATL1* mRNA and protein levels are considerably elevated in LTED cells, suggesting a potential role for *GLYATL1* in endocrine therapy resistance.

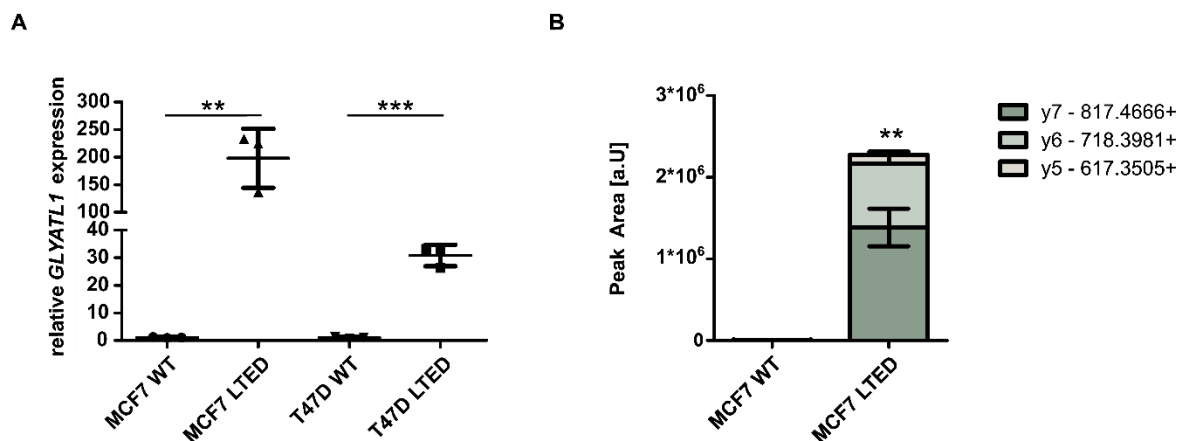


**Figure 10: Basal mRNA and protein GLYATL1 levels in wildtype and LTED cells.** *GLYATL1* mRNA levels were determined by RT-qPCR in MCF7 and T47D WT and LTED cells. mRNA expression was normalized on *ACTB* and *PUM1* levels and relative changes to the corresponding wildtype were calculated. (B) *GLYATL1* protein levels in MCF7 cells were analyzed using a PRM-based targeted mass spectrometry approach. Specific fragments of the *GLYATL1* peptide (ALLVETEDILKL) are indicated by color. Mass spectrometry data were generated and analyzed by Luisa Schwarzmüller. Data are represented as the mean  $\pm$  SEM, RT-qPCR results with  $n=3$  biological replicates with three technical replicates each, and LC-MS results with  $n=4$  biological replicates. Statistical significance was assessed using unpaired Student's t-test, where \*\*\* indicates  $p<0.001$ , and \*\* indicates  $p<0.01$ .

## 4.2 High *GLYATL1* Expression is Associated with Poor Patient Prognosis

To investigate the clinical relevance of *GLYATL1* expression in luminal A breast cancer, I performed Kaplan-Meier survival analyses using two independent datasets.

Luminal A breast cancer patients of the TCGA cohort ( $n=542$ ) were divided into two groups based on the median *GLYATL1* expression levels. Survival analysis revealed a significant correlation between elevated *GLYATL1* expression and reduced overall survival, with a p-value of 0.0185 (Figure 11A). Patients with high *GLYATL1* expression levels had a significantly lower survival probability compared to those with lower expression levels as indicated by a more pronounced decline in the survival curve over time.

## Results

Similarly, a recurrence-free survival analysis was performed using the METABRIC cohort, including ER-positive patients treated with tamoxifen (n=178). The analysis revealed a correlation between high *GLYATL1* expression and significantly shorter recurrence-free survival (Figure 11B). This correlation suggests an increased risk of disease recurrence despite tamoxifen treatment in patients with high *GLYATL1* expression. These consistent findings across the two cohorts highlight the potential clinical relevance of *GLYATL1* as an indicator of disease progression.

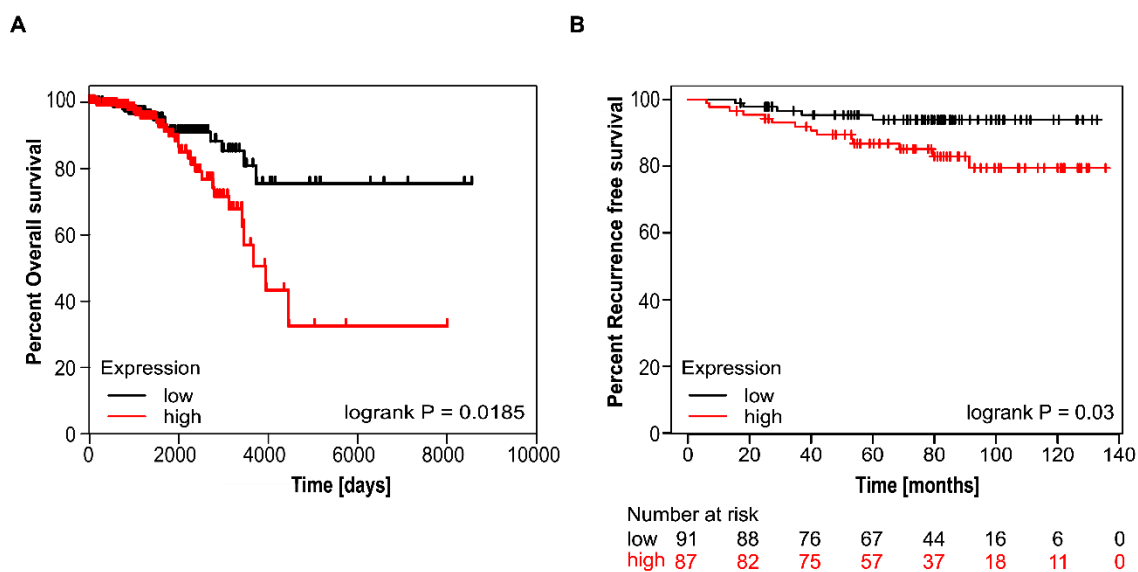


**Figure 11: Survival analysis based on *GLYATL1* expression in patients.** (A) Median-based survival analysis of luminal A breast cancer patients in the TCGA dataset of *GLYATL1* low (black) versus high (red) gene expression (n=542). (B) Median-based recurrence-free survival analysis of ER-positive breast cancer patients undergoing tamoxifen treatment in the METABRIC dataset of *GLYATL1* low (black) versus high (red) gene expression (n=178), plotted with Kaplan-Meier Plotter [165].

### 4.3 *GLYATL1* Expression is Correlated with Estrogen Supply

Given the observation of elevated *GLYATL1* levels in the context of endocrine therapy resistance, I further investigated the impact of drug withdrawal on *GLYATL1* expression. To this end, I cultured MCF7 LTED cells in the presence of 10 nM estrogen (+E2) for 12 weeks. mRNA samples were obtained at regular four-week intervals and changes in *GLYATL1* expression over time were monitored via RT-qPCR. The mRNA

levels demonstrated a rapid decline in *GLYATL1* expression within the initial four-week period, which then stabilized at a constant low level (Figure 12A blue squares).

Following the initial 12 weeks, estrogen was again withdrawn from the pre-treated cells. Following estrogen depletion, *GLYATL1* expression increased rapidly, surpassing even higher levels of mRNA compared to the original LTED cells in MCF7 (Figure 12A black triangles). Similar effects were observed in T47D cells with a slower recovery of *GLYATL1* expression levels upon re-addition of therapeutic stress (Figure 12B).

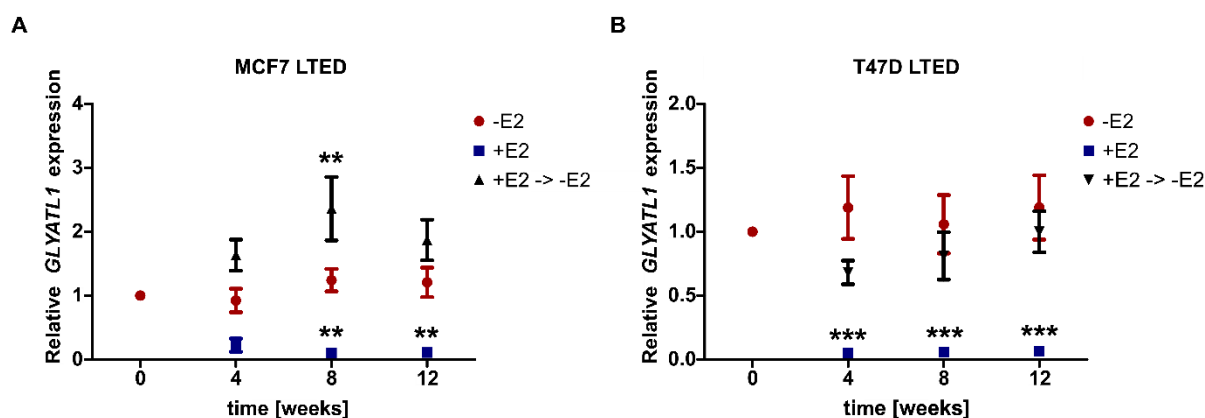


**Figure 12: Effect of Estrogen presence on *GLYATL1* expression.** MCF7 LTED (A) and T47D LTED (B) cells were cultured in the presence (+E2, blue) or absence (-E2, red) of estrogen for 12 weeks. After these initial 12 weeks, cells were once again deprived of estrogen for an additional 12 weeks (+E2 → -E2, black). mRNA levels were determined by RT-qPCR and normalized on *ACTB* and *PUM1*. Relative changes to LTED cultivated in estrogen-depleted media were calculated. Data are represented by mean  $\pm$  SEM of  $n \leq 4$  biological replicates (each with 3 technical replicates). Statistical significance was assessed using two-way ANOVA with Bonferroni post-test to compare samples to LTED cells growing in estrogen-depleted media at the indicated time point, where \*\*\* indicates  $p < 0.001$ , and \*\* indicates  $p < 0.01$ .

After having observed the long-term effect of estrogen presence on *GLYATL1* expression upon estrogen presence, I next tested the effect of short-term estrogen treatment of LTED cells. To this end, I treated LTED cells with wildtype media containing 10 nM estrogen for 48 hours and determined the *GLYATL1* mRNA levels via RT-qPCR. The *GLYATL1* levels in LTED cells were found to significantly decrease after 48 hours (Figure 13A).

In addition, the effect of short-term estrogen deprivation on *GLYATL1* expression was tested in wildtype cells. Following a 48-hour deprivation period, wildtype cells exhibited a non-significant trend of increased *GLYATL1* mRNA levels (Figure 13A). Similar effects were observed in T47D cells (Figure 13B).

Taken together, these findings indicate a strong inverse correlation between estrogen levels and *GLYATL1* expression. Thus, *GLYATL1* expression appears to be exclusive within the context of estrogen deprivation mimicking aromatase inhibition.

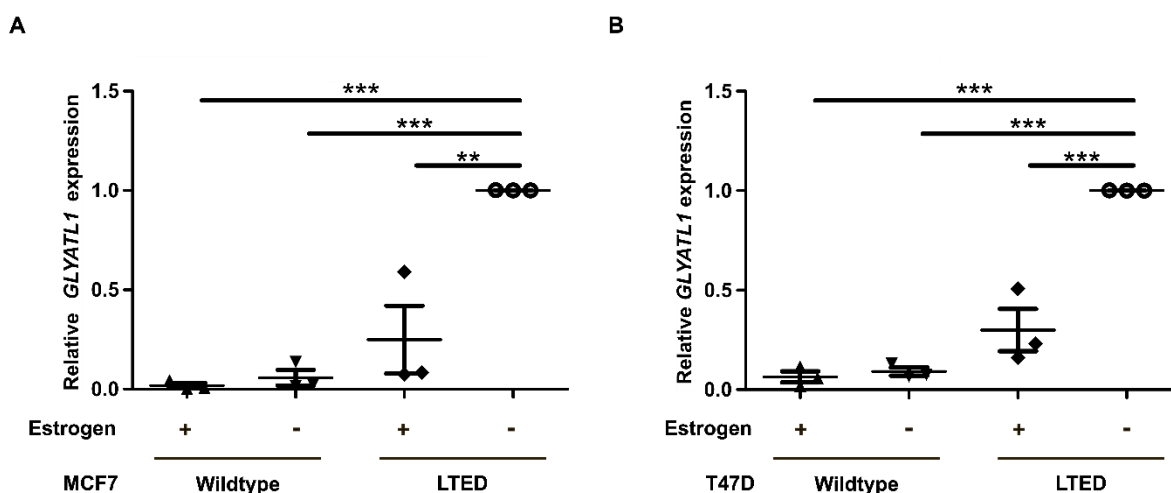


**Figure 13: Effect of short-term estrogen supply on *GLYATL1* expression.** *GLYATL1* mRNA levels were assessed following 48 hours of estrogen treatment in LTED cells or estrogen deprivation in wildtype MCF7 (A) and T47D (B) cell lines via RT-qPCR. mRNA levels were normalized on *ACTB* and *PUM1* expression and relative changes to LTED cells cultivated in estrogen-depleted media were calculated. Data are represented by mean  $\pm$  SEM of 3 biological replicates (each with 3 technical replicates). Statistical significance was assessed using one-way ANOVA, where \*\*\* indicates  $p < 0.001$ , and \*\* indicates  $p < 0.01$ .

#### 4.4 Regulation of *GLYATL1* Expression by ER $\alpha$ and FOXA1

Following the observation that *GLYATL1* expression is anti-correlated with estrogen supply, I next tested the involvement of different transcription in regulating *GLYATL1* expression. Based on the UCSC Genome Browser, several transcription factors showed binding sites in the promoter region of *GLYATL1* experimentally as identified in Transcription Factor Chromatin Immunoprecipitation (TF-ChIP) experiments suggesting a complex interplay of different transcription factors in *GLYATL1* regulation.

Amon other transcription factors, the estrogen receptor (*ESR1*) showed potential regulation of *GLYATL1* (Figure 14).

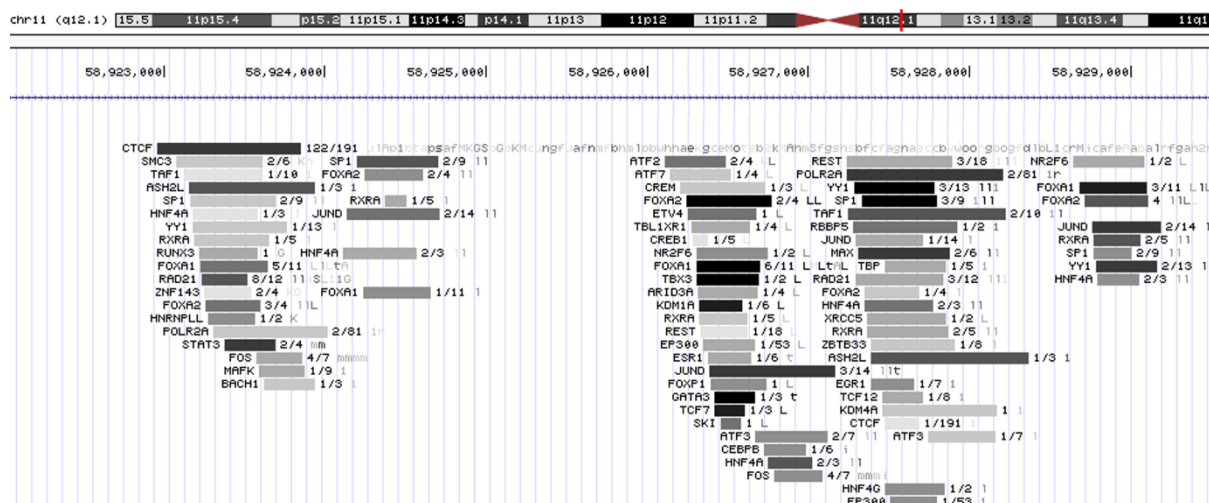


**Figure 14: Transcription factor occupancy of *GLYATL1* promoter.** Data from the UCSC Genome Browser (GRCh38/hg38, ENCODE track) showed identified binding sites of transcription factors based on TF-ChIP-sequencing experiments [166].

Moreover, the analysis of *ESR1* mRNA levels identified elevated expression in MCF7 and T47D LTED cells in comparison to their corresponding wildtype cells (Figure 15A). To investigate the potential involvement of the estrogen receptor in *GLYATL1* regulation, I performed a knockdown of *ESR1* for 72 hours and monitored the effect on *GLYATL1* mRNA levels via RT-qPCR. Along with the significant reduction of *ESR1* levels (Figure 15B), *GLYATL1* expression significantly decreased in MCF7 LTED as well as in T47D LTED cells (Figure 15C). Since the LTED cell lines were constitutively grown in estrogen-depleted media, this reduction suggests that ER mediates *GLYATL1* expression in an estrogen-independent manner.

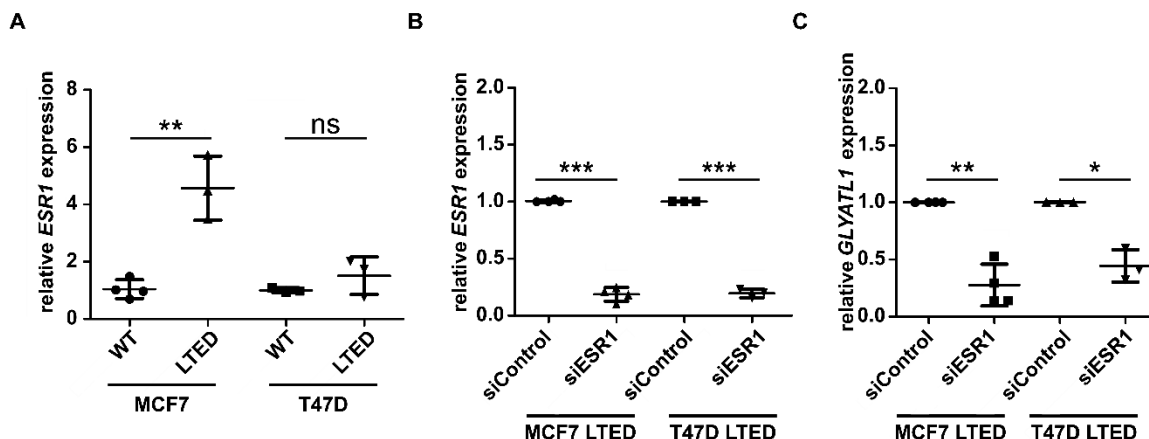


**Figure 15: Effect of *ESR1* knockdown on *GLYATL1* expression.** (A) Basal mRNA levels of *ESR1* were evaluated by RT-qPCR in WT and LTED MCF7 and T47D cells. (B, C) LTED cells were transfected with a pool of siRNAs targeting *ESR1* (si*ESR1*) or non-targeting siRNA (siControl) for 72h. Knockdown efficiency (B) and effect on *GLYATL1* expression (C) were validated by RT-qPCR. Values for mRNA expression were normalized to *ACTB* and *PUM1* expression levels. Data are represented by mean  $\pm$  SEM of  $\geq 3$  biological replicates (each with 3 technical replicates). Statistical significance was assessed using unpaired (A) or paired (B, C) Student's t-test, where ns indicates a non significant p value, \*\*\* indicates  $p < 0.001$ , \*\* indicates  $p < 0.01$ , and \* indicates  $p < 0.05$ .

Besides *ESR1*, another luminal transcription factor, called *FOXA1*, was experimentally identified as binding the *GLYATL1* promoter (Figure 14). *FOXA1*, also known as hepatocyte nuclear factor 3- $\alpha$ , has been shown to facilitate ER $\alpha$ -mediated transcription by acting as a “pioneer” factor. *FOXA1* opens compact chromatin structures by interacting with nucleosomal core histones, displacing linker histones at target enhancers and promoter sites, and thereby allowing subsequent transcription factor binding [167, 168].

Unlike *ESR1*, basal *FOXA1* mRNA levels were not significantly altered in LTED cells (Figure 16A). To investigate whether *FOXA1* is involved in ER $\alpha$ -mediated *GLYATL1* regulation, I performed a *FOXA1* knockdown (Figure 16B) and subsequently evaluated the impact on *GLYATL1* mRNA expression. The knockdown resulted in a significant reduction in *GLYATL1* mRNA levels in both MCF7 LTED and T47D LTED cell lines (Figure 16C).

Taken together, these results suggest that *ESR1* and *FOXA1* are involved in the regulation of *GLYATL1* expression under estrogen-deprived conditions.

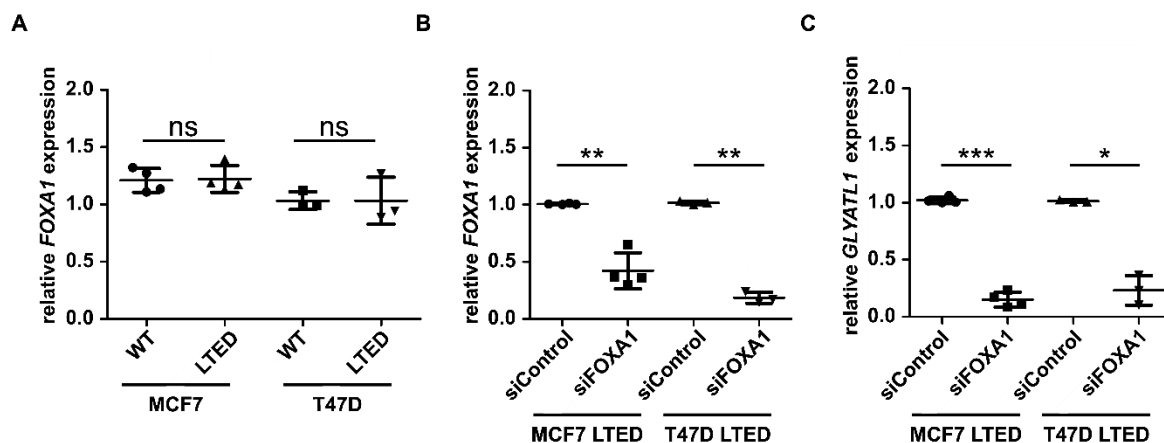


**Figure 16: Effect of *FOXA1* knockdown on *GLYATL1* expression.** (A) Basal mRNA levels of *FOXA1* were evaluated by qPCR in WT and LTED MCF7 and T47D cells. (B, C) LTED cells were transfected with a pool of siRNAs targeting *FOXA1* (siFOXA1) or non-targeting siRNA (siControl) for 72h. Knockdown efficiency (B) and effect on *GLYATL1* expression (C) were validated by qPCR. Values for mRNA expression were normalized to *ACTB* and *PUM1* expression levels. Data are represented by mean  $\pm$  SEM of  $\geq 3$  biological replicates (each with 3 technical replicates). Statistical significance was assessed using unpaired (A) or paired (B, C) Student's t-test, where ns indicates non-significant p-values, \*\*\* indicates  $p < 0.001$ , \*\* indicates  $p < 0.01$ , and \* indicates  $p < 0.05$ .

#### 4.5 Generation of a *GLYATL1*-specific Antibody

To gain a deeper understanding of the role of *GLYATL1* in the context of endocrine therapy resistance, protein-specific antibodies are a valuable tool for conducting targeted assays such as Western Blots and immunofluorescence. However, no commercially available antibody targeting *GLYATL1* was identified that demonstrated sufficient specificity. As a result, custom monoclonal antibodies were generated in collaboration with the DFKZ antibody core facility.

Mice were injected with a *GLYATL1*-specific peptide to stimulate a directed immune response. Sera of the mice were tested via Western Blot and immunofluorescence using HEK293FT cells transiently expressing Flag-tagged *GLYATL1*. B-cells from mice exhibiting specificity towards *GLYATL1* were isolated and fused to immortalized myeloma cells. The hybridoma “mother” clones were cultivated in selective media and screened for *GLYATL1* recognition via Western blotting and immunofluorescence. “Mother” clones exhibiting specific binding to *GLYATL1* were subcloned via single-cell

## Results

spotting in the Cellular Tool Core Facility. The individual “daughter” clones were then assessed further for their recognition of GLYATL1 via immunofluorescence and Western blotting.

I identified one subclone, designated #305, which exhibited distinctive immunofluorescence signals that co-localized with the control Flag signal, in transiently transfected HEK293FT expressing a Flag-tagged GLYATL1 construct (Figure 17A). However, clone #305 was unable to detect the lower endogenous level in MCF7 LTED cells even when undiluted. Additional purification via protein G affinity chromatography did not improve the quality and specificity of the clone. Moreover, this clone was unable to recognize GLYATL1 protein in Western blot analysis.

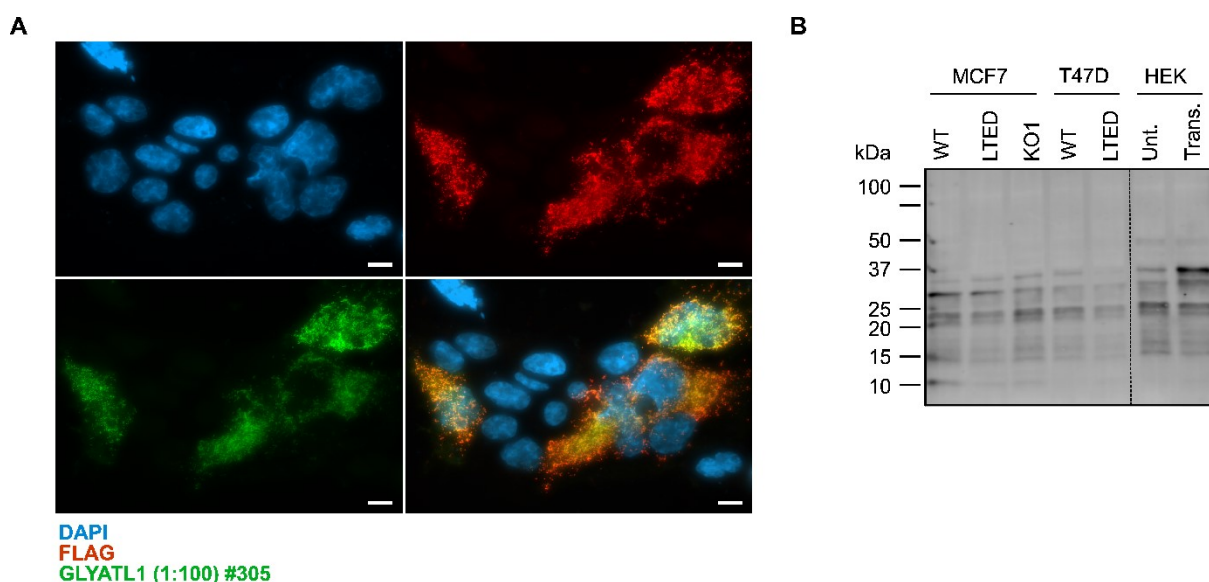


**Figure 17: Generation of GLYATL1 specific antibody.** (A) Daughter clone #305 was tested with a dilution of 1:100 (green) for GLYATL1 specificity via immunofluorescence in HEK293 FT cells transiently expressing Flag-tagged GLYATL1. Flag antibody (red) was used as a control. DNA was stained by DAPI (blue). Scale bar = 10  $\mu$ m. (B) Representative picture of Western blot using purified antibodies of daughter clones and protein lysates of indicated wildtype (WT), long-term estrogen deprived (LTED), *GLYATL1* knockout (KO1) MCF7 or T47D cells and either untransfected (Unt.) or transiently transfected (Trans.) HEK293FT cells expressing Flag-tagged *GLYATL1*.

Other “daughter” clones successfully demonstrated specific recognition of Flag-tagged GLYATL1 in Western blot analysis. Like #305, these clones were unable to recognize

lower endogenous levels even when undiluted. Additional Protein G affinity chromatography to concentrate the antibody did not improve the sensitivity of the antibodies, resulting in similar unspecific band intensities on a Western blot of wildtype, resistant, and *GLYATL1* knockout lysates (Figure 17B).

Since all attempts ended up not recognizing endogenous levels, we discontinued the generation of a specific antibody, and I instead continued with phenotypic assays to investigate the role of *GLYATL1*.

#### 4.6 *GLYATL1* Knockdown Reduces Cell Proliferation

To determine whether *GLYATL1* contributes to therapy resistance and facilitates cell growth in the absence of estrogen, I next investigated the effect of knocking down *GLYATL1* in LTED cells on proliferation. RNA silencing was performed with a pool of siRNAs targeting *GLYATL1* mRNA to minimize off-target effects. RT-qPCR indicated a mean reduction of ~90% in mRNA after eight days post-transfection in MCF7 and T47D LTED cells (Figure 18A).

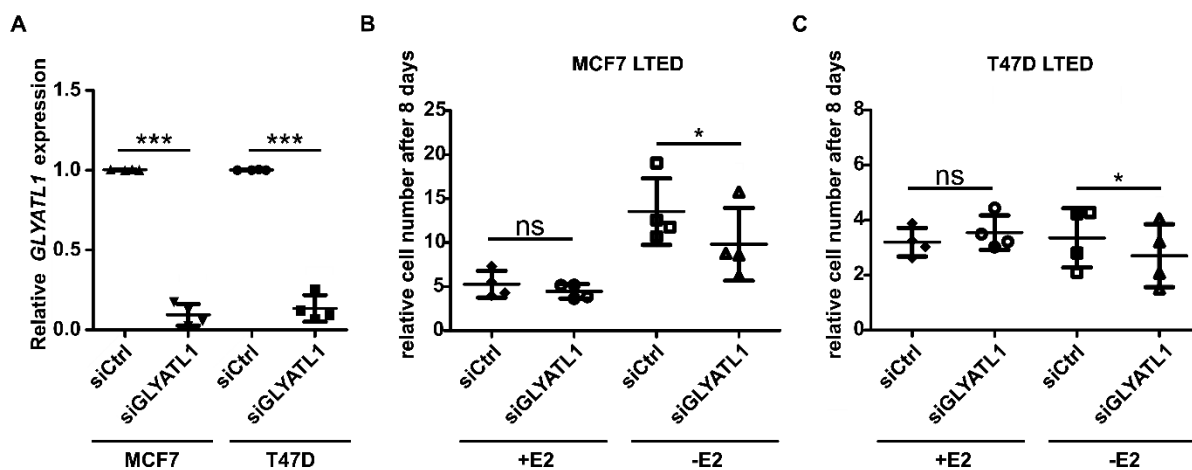


**Figure 18: *GLYATL1* knockdown reduces cell proliferation.** Knockdown of *GLYATL1* was performed via RNA interference in MCF7 (A, B) and T47D (B, C) LTED cells and verified via RT-qPCR (A). The proliferation rate in media with (+E2) and without (-E2) estrogen was measured via microscopy-based nuclear count (B, C). Data are presented as mean  $\pm$  SEM of 4 biological (RT-qPCR with 3 technical replicates and proliferation assay with 6 technical replicates). Statistical significance was assessed using paired Student's t-test, where ns indicates non-significant p-values, \*\*\* indicates  $p < 0.001$ , and \* indicates  $p < 0.05$ .

The effect of *GLYATL1* knockdown on proliferation was monitored in media containing estrogen and estrogen-depleted media. In the presence of estrogen, the knockdown of *GLYATL1* did not affect the proliferation in MCF7 LTED cells. However, knockdown resulted in a significant disadvantage in proliferation in estrogen-depleted media (Figure 18B). A similar trend was observed in T47D LTED cells (Figure 18C), indicating that *GLYATL1* exerts a significant influence on proliferative behavior in the absence of estrogen. However, this effect was diminished in the presence of estrogen, supporting the importance of *GLYATL1* in the context of endocrine therapy resistance.

### **4.7 *GLYATL1* Knockout Has a Proliferation Disadvantage**

To gain a more comprehensive understanding of the biological role of *GLYATL1*, knockout cell lines were generated for subsequent downstream experiments. This knockout approach allows for permanent disruption of *GLYATL1* expression, eliminating any residual gene expression as observed by partial silencing that could partially compensate for the biological function. The knockout was achieved through the CRISPR/Cas9 gene-editing approach and performed by Dr. Emre Sofyali. Specifically, a single guide RNA (sgRNA) targeting exon four was utilized to induce targeted deletions.

Following the initial editing, I deconvoluted this heterogeneous pool of edited cells in collaboration with the Cellular Tool Core Facility at the DKFZ to generate cells with a single clonal background. Sanger sequencing of the genomic target region of the individual clones identified two different clones harboring the same 20-base pair homozygous deletion (Figure 19).



**Figure 19: Scheme of *GLYATL1* knockout.** CRISPR Cas-9 approach using a sgRNA targeting exon four resulted in two clonal knockout cell lines (KO) with 20 bp deletion evaluated by Sanger sequencing.

The protein knockout was validated through a PRM-based targeted mass spectrometry approach, performed by Luisa Schwarzmüller. A significant reduction in *GLYATL1* levels was observed in the two different *GLYATL1* knockout cell lines (Figure 20A). Even though the deletion in both knockout clones was identical, the levels of identified fragments differed between the two different knockout clones. While the summed mean of the signal was reduced by almost 99% in knockout clone 1, higher signal levels of *GLYATL1* fragments were detected in knockout clone 2, which led to a summed mean reduction by 76%. Since no internal standard was spiked in, the limit of quantification could not be determined in this experiment. Thus, it was not possible to determine whether the observed signal detected in the knockout clones could be considered a specific signal or background noise.

These *GLYATL1* knockout clones were used to validate the observed influence on proliferation. Compared to LTED cells, both *GLYATL1* knockout cell lines exhibited an almost 3-fold decrease in proliferation rate in estrogen-depleted media over eight days (Figure 20). This significant reduction in proliferation rate indicates that the knockout of *GLYATL1* exacerbates the previously observed negative effects on cell proliferation following *GLYATL1* knockdown using siRNA and underlines the importance of *GLYATL1* on cellular growth under estrogen-depleted conditions.

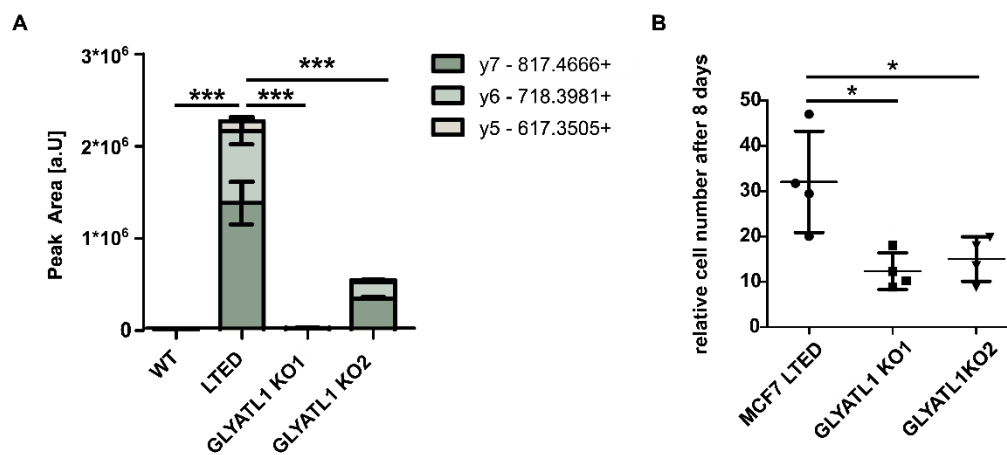


**Figure 20: *GLYATL1* knockout reduces cell proliferation.** (A) Protein levels of *GLYATL1* in MCF7 determined by PRM-based targeted mass spectrometry approach. Fragments of a single *GLYATL1* peptide are indicated. Mass spectrometry data was generated and analyzed by Luisa Schwarzmüller. (B) The proliferation rate in media without estrogen was measured via nuclear count. Data are represented as mean  $\pm$  SEM,  $n=3$  (PRM-based MS), and  $n=4$  (proliferation assay, with 6 technical replicates). Statistical significance was assessed using one-way ANOVA with Bonferroni post-test, where \*\*\* indicates  $p<0.001$ , and \* indicates  $p<0.05$ .

#### 4.8 *GLYATL1* Overexpression Alone Does not Confer Endocrine Therapy Resistance

After having seen a disadvantage in proliferation with *GLYATL1* knockdown and knockout in resistant cell lines, I next investigated the putative potential of *GLYATL1* overexpression to confer a resistant phenotype in wildtype cell lines. MCF7 and T47D wildtype cell lines were lentivirally transduced by the Cellular Tools Core Facility at the DKFZ to stably overexpress V5-tagged *GLYATL1* under the strong CMV promoter and enhancer (*GLYATL1* OE). Wildtype cells stably transfected with the same backbone lacking the *GLYATL1* sequence served as controls to exclude transduction-related effects (empty vector).

To characterize the effects of *GLYATL1* overexpression, I first determined the *GLYATL1* mRNA levels via RT-qPCR. Compared to the empty vector control, *GLYATL1* mRNA levels were significantly elevated in MCF7 and T47D overexpressing cell lines (Figure 21A, B).

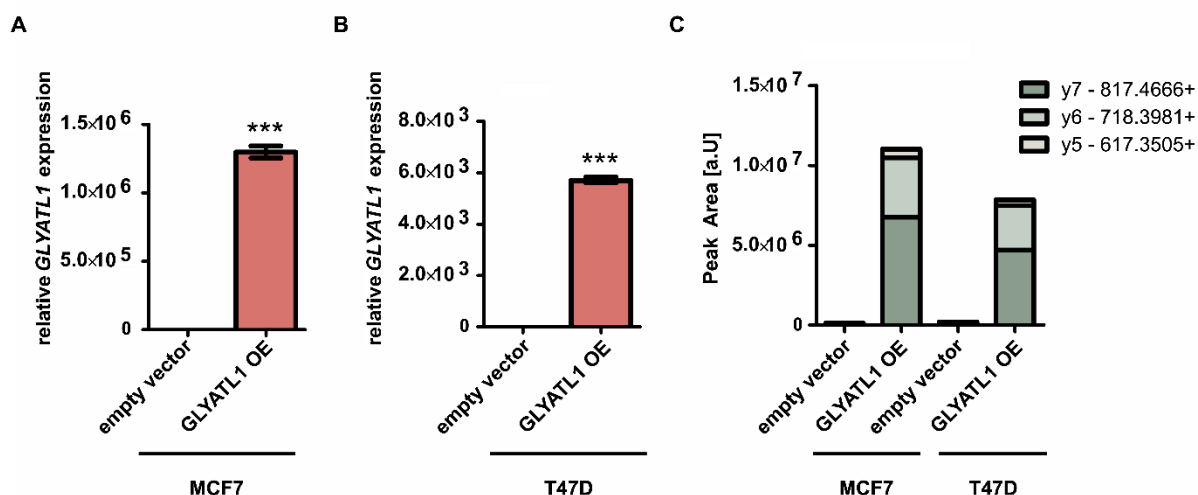


**Figure 21: Validation of *GLYATL1* overexpressing cell lines.** (A, B) Levels of *GLYATL1* mRNA in stable *GLYATL1* overexpressing (OE) and empty vector MCF7 (A) and T47D (B) cell lines. mRNA levels were quantified via RT-qPCR and normalized to *ACTB* and *PUM1* levels. Data are represented by mean  $\pm$  SEM of 3 biological replicates (each with 3 technical replicates). (C) Protein levels of *GLYATL1* in the overexpressing and empty vector cell lines determined by PRM-based targeted mass spectrometry approach. Fragments of a single *GLYATL1* peptide are indicated. Mass spectrometry data was generated and analyzed by Luisa Schwarzmüller. RT-qPCR data are represented as mean  $\pm$  SEM,  $n=3$  (with 6 technical replicates), and a single protein lysate was measured via LC-MS. Statistical significance was assessed using unpaired Student's t-test (A, B), where \*\*\* indicates  $p < 0.001$ .

In collaboration with Luisa Schwarzmüller, I further applied a PRM-based targeted mass spectrometry approach to verify the upregulation on protein level. Consistent with the increased mRNA levels, the overexpressing cell lines showed an approximately 89-fold increase in *GLYATL1* protein levels in MCF7 and an approximately 40-fold increase in T47D cells compared to the corresponding empty vector control (Figure 21C).

After verifying the *GLYATL1* overexpression, I next tested the influence of overexpression in wildtype to potentially cope with aromatase inhibition. To this end, I performed a cell proliferation assay over nine days in the presence of estrogen (+E2) or deprived of estrogen (-E2). Under these conditions, no proliferative advantage was observed in MCF7 *GLYATL1* overexpressing cell lines (Figure 22A, B). In contrast, T47D *GLYATL1* overexpressing cells even exhibited a significant proliferative disadvantage after nine

## Results

days of incubation in estrogen-containing media compared to empty vector control. However, the proliferation disadvantage was abolished in the absence of estrogen (Figure 22C, D).

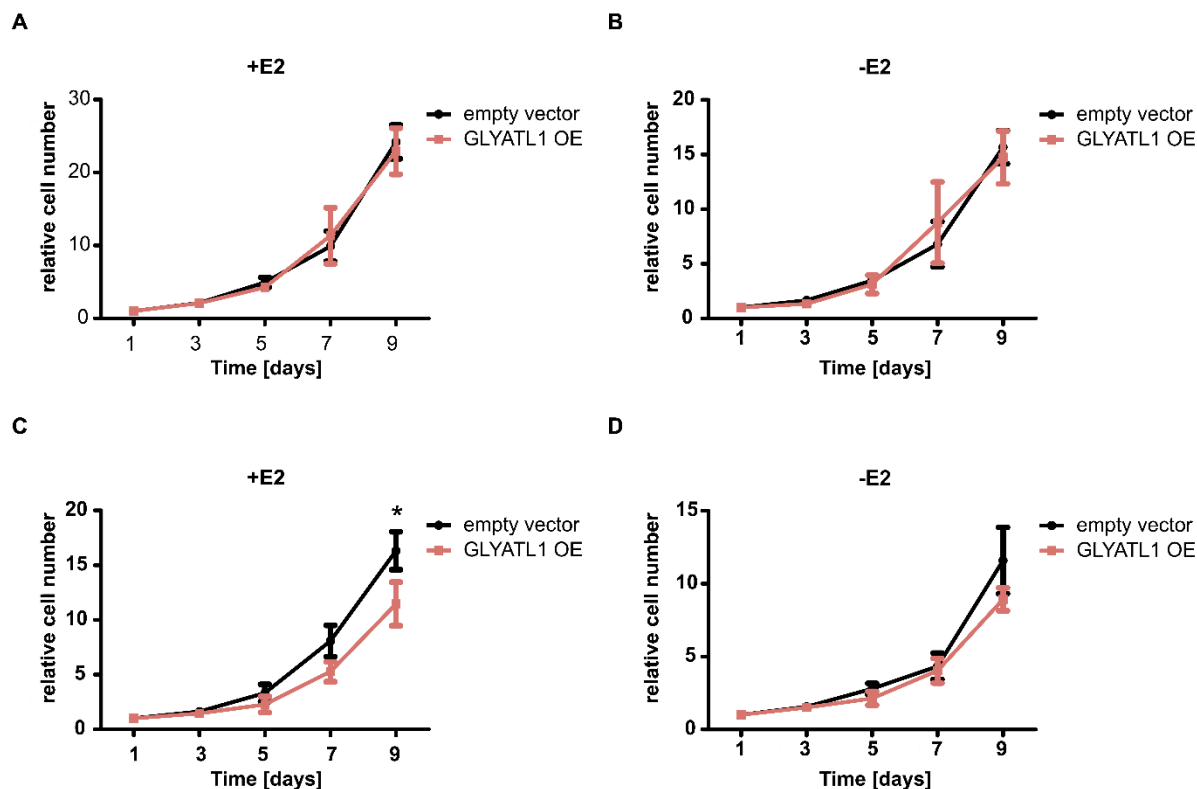


**Figure 22: Effect of *GLYATL1* overexpression on MCF7 cell proliferation under endocrine therapy condition.** MCF7 (A, B) and T47D (C, D) *GLYATL1* overexpression (GLYATL1 OE) and empty vector cells were seeded and treated with the presence and absence of estrogen ( $\pm$ E2). Microscopy-based nuclei counting was performed every second day. Proliferation rates were normalized to seeding control. Data presents as mean  $\pm$  SEM, n=3 (each with 6 technical replicates). Statistical significance was assessed using two-way ANOVA, where \* indicates  $p < 0.05$ .

Taken together, these results indicate that the used *GLYATL1* overexpression system alone does not provide a proliferation advantage under estrogen-deprived conditions suggesting that *GLYATL1* cannot confer resistance towards aromatase inhibition in the examined period. However, while *GLYATL1* overexpression alone was insufficient to induce resistance, *GLYATL1* contributed to a proliferative phenotype in an acquired resistance setting as shown earlier (see 4.6, 4.7). Next, I aimed to investigate the underlying mechanisms on how *GLYATL1* contributed to maintaining resistance.

## 4.9 Interaction Partner of GLYATL1

To gain insight into the cellular role of GLYATL1, I analyzed its interactome using a BioID-based proximity labeling approach in MCF7 cell lines. This method is based on a small biotin ligase from *Aquifex aeolicus* (BioID2), which biotinylates proteins in close proximity to the target protein within an approximately 10 nm labeling radius. Following labeling, the biotinylated proteins can be purified by streptavidin pull-down. This allows for the identification of direct and indirect interactors, as well as proteins in close vicinity that do not physically interact with the protein of interest via Western blotting and mass spectrometry (Figure 23A) [158, 169, 170].

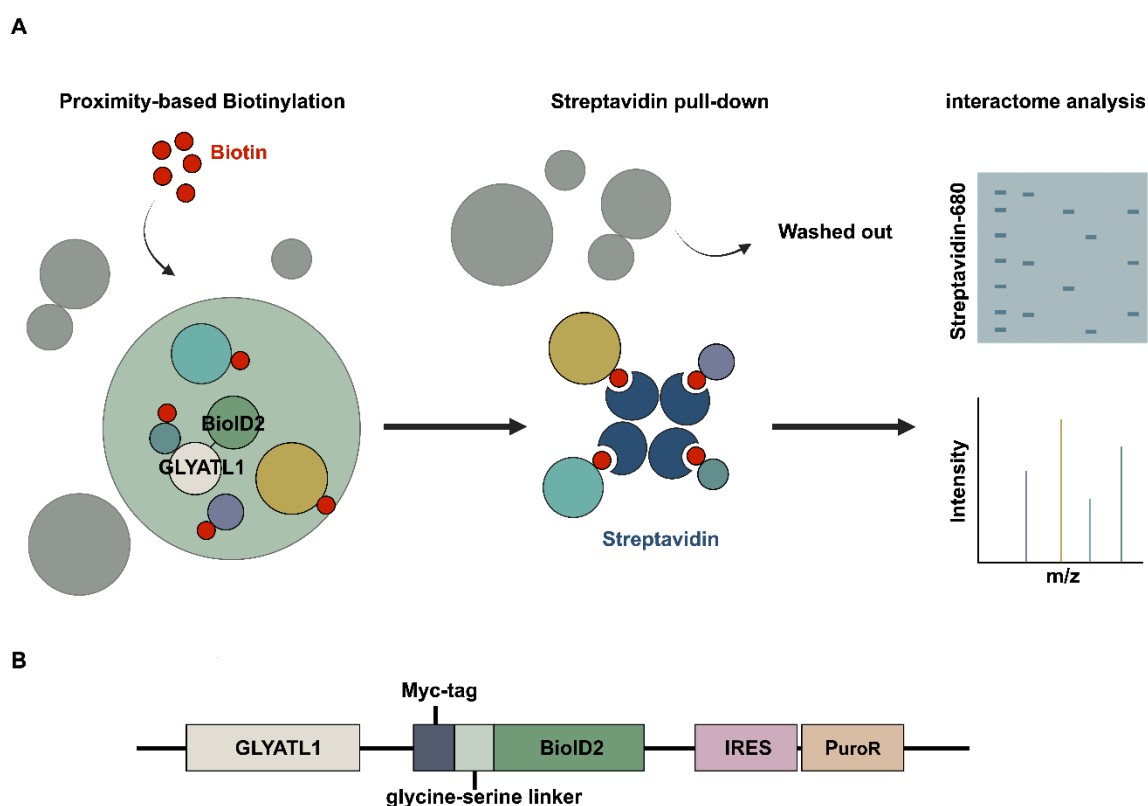
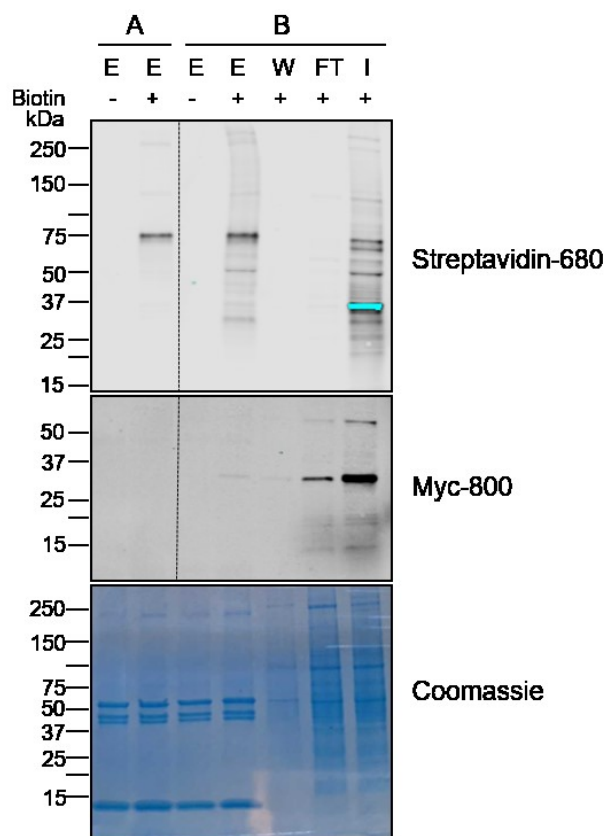


**Figure 23: BioID2 experiment.** (A) Scheme of experimental flow. The addition of biotin to cells expressing BioID2 construct leads to proximity-based biotinylation of proteins, which can be pulled down with Streptavidin beads and further analyzed by Western blot and mass spectrometry. Adapted and modified from Varnaitė et al. [171]. (B) Schematic illustration of used BioID2 constructs.

## Results

In collaboration with the Cellular Tool Core facility, we generated a plasmid with BioID2 fused to the C-terminus of *GLYATL1*, which thereby enables the targeting and biotinylation of interacting proteins as well as nearby proteins of *GLYATL1*. The backbone plasmid was kindly gifted from Prof. Dr. Stefan Pusch and contained further a Myc tag as a detectable epitope and a 25-nm glycine-serine linker to enhance the flexibility and therefore magnify the biotinylation range of the BioID2 tag. A puromycin resistance (PuroR) cassette under an internal ribosome entry site (IRES) element enabled the selection of positive clones expressing the construct (Figure 23B).

The fusion construct was transduced by lentiviral infection into MCF7 cell lines by the Cellular Tools Core facility, followed by selection with puromycin. Following the transfection of the cells, I incubated the cells with biotin for 18 hours to allow for sufficient biotinylation of target proteins. Subsequently, I lysed the cells, pulled down biotinylated proteins using streptavidin beads, and analyzed them via Western blotting with streptavidin coupled to a fluorophore (Figure 24).



A: rwpMXs\_MCS\_MYC\_Linkers\_BioID2 IRES-Puro (29 kDa)  
 B: rwpMXs\_GLYATL1\_MYC\_Linkers\_BioID2 IRES-Puro (63 kDa)

**Figure 24: Western blots of Streptavidin pull-downs of indicated BiOD constructs.** Eluate (E), Wash (W), flow-through (FT), and Input (I) samples were loaded. Biotinylated proteins were evaluated with streptavidin-680 (top), and myc-tagged constructs were evaluated with MYC-antibody (middle). All proteins in the sample were evaluated with Coomassie-stained gel.

The streptavidin-680 blot demonstrated biotinylated proteins exclusively present in cell lysates treated with biotin. Furthermore, pull-down using streptavidin beads resulted in the successful recovery of biotinylated proteins in the elution fraction, as evidenced by the minimal protein levels observed in the flow-through and wash fractions. The protein band pattern in the elution fraction for the GLYATL1 construct were found to be distinct from those of the control lacking the GLYATL1 sequence, indicating the specific biotinylation and enrichment of GLYATL1-interacting proteins.

To get reliable results using mass spectrometry, the protein concentration in the elution samples have to reach a minimum concentration, which has to be detectable on Coomassie-stained gel. Coomassie-staining of the gel loaded with the same samples revealed a consistent protein pattern between 37 and 55 kDa in all elution samples irrespective of biotin treatment and the used construct (Figure 24, Coomassie, Lane 1-4). Since this protein pattern could be observed in samples not treated with biotin and is missing in the input, flow-through and wash sample, the observed bands potentially originate from the streptavidin beads themselves rather than from biotinylated proteins. Beside this consistent band pattern, no detectable differences could be observed between the control construct and the GLYATL1-construct samples suggesting that the protein concentrations were likely below the detection threshold. Attempts to increase of the input amount to 5  $\mu$ g did not result in improved detection.

In the Myc blot, the fused GLYATL1 construct was predominantly found in the flow-through (FT) and input with minimal detection in the elution and wash fraction. While the anticipated molecular weight of the fusion protein is 67 kDa, the Myc signal was observed at  $\sim$ 34 kDa, which aligns with the calculated size of GLYATL1 alone. This suggests that the fusion protein might have been instable within the cell, resulting in a reduction of biotinylated proteins within the lysates, which cannot be detected in the Coomassie stain. However, the banding pattern observed in the streptavidin-680 blot indicates that the full construct including the biotin ligase had still been expressed,

resulting in the biotinylation of proteins in close proximity to the ligase. To inhibit the potential proteasomal degradation of the full-length construct, cells were treated with 10  $\mu$ M MG132, a specific proteasome inhibitor [172], at the time point of biotin treatment. However, even after MG132 treatment, the Coomassie-stained SDS gel still did not show any specific bands (Data not shown) suggesting that the degradation might still occur or other factors are contributing to the lack of detectable biotinylated proteins on the gel.

### **4.10 GLYATL1 is Localized in the Mitochondria**

Since the initial approach to identify interaction partners for elucidating the function of GLYATL1 was unsuccessful, I next investigated its cellular localization to narrow down the potential functions of GLYATL1 based on its distribution within the cell.

Bioinformatics-based analysis predicted different cellular localizations for the GLYATL1 protein. DeepLoc 2.0 algorithm predicted that GLYATL1 is localized within the cytoplasm and contains a predicted nuclear localization and export signal [173, 174]. In contrast, the WoLFPSORT prediction tool indicated a probability of mitochondrial localization [175, 176].

To test for potential mitochondrial localization, I used a fluorescent probe staining mitochondrial cristae to analyze potential co-localization in HEK293FT cells. Given that the generated specific monoclonal antibody targeting GLYATL1 was not sensitive enough to target endogenous levels (see 4.5), transient expression of Flag-tagged GLYATL1 was utilized to investigate the cellular localization. Confocal microscopy images demonstrated an overlap between the Flag-GLYATL1 signal and the mitochondrial probe, indicating a distinct mitochondrial localization within the cell. This mitochondrial localization was further confirmed in transfected MCF7 and T47D WT cells (Figure 25).

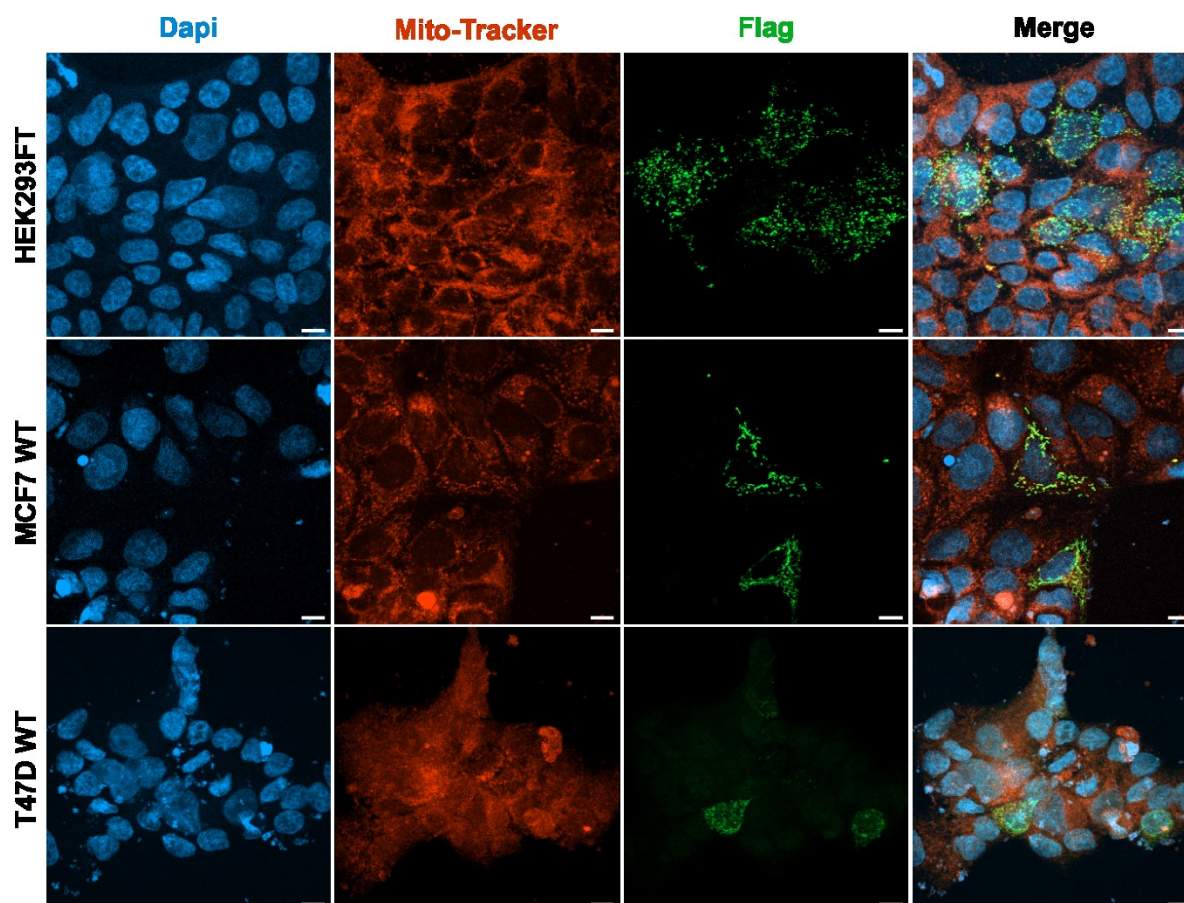


**Figure 25: Distinct mitochondrial localization of GLYATL1 by immunostaining.** HEK293FT, MCF7, and T47D wildtype (WT) transient expressing Flag-tagged GLYATL1 were subjected to immunostaining to evaluate localization within the cell. In addition, Live-Orange labeling mitochondria was introduced and nuclei were stained with DAPI. Data was generated on a Zeiss LSM 900 Airyscan microscope, scale bar = 10  $\mu$ m.

#### 4.11 Influence of GLYATL1 on Acyl-CoA Abundance and Water-soluble Metabolites

Having observed a mitochondrial localization of GLYATL1, I next focused on its mechanistic role in contributing to resistance. Since mitochondrial proteins are involved in various metabolic processes [177] and given that GLYATL1 is annotated as an enzyme that catalyzes the transfer of an acyl group to glutamine (Figure 9), I investigated the dependency on glutamine in MCF7 wildtype, resistant, and *GLYATL1* knockout cells. To this end, I cultivated the cells in media with varying concentrations of glutamine, ranging from 0 to 4.5 mM. After cultivation for eight days, I determined the relative cell

## Results

proliferation to cells grown in media with 2 mM glutamine representing the glutamine concentration in normal growth media (Figure 26A).

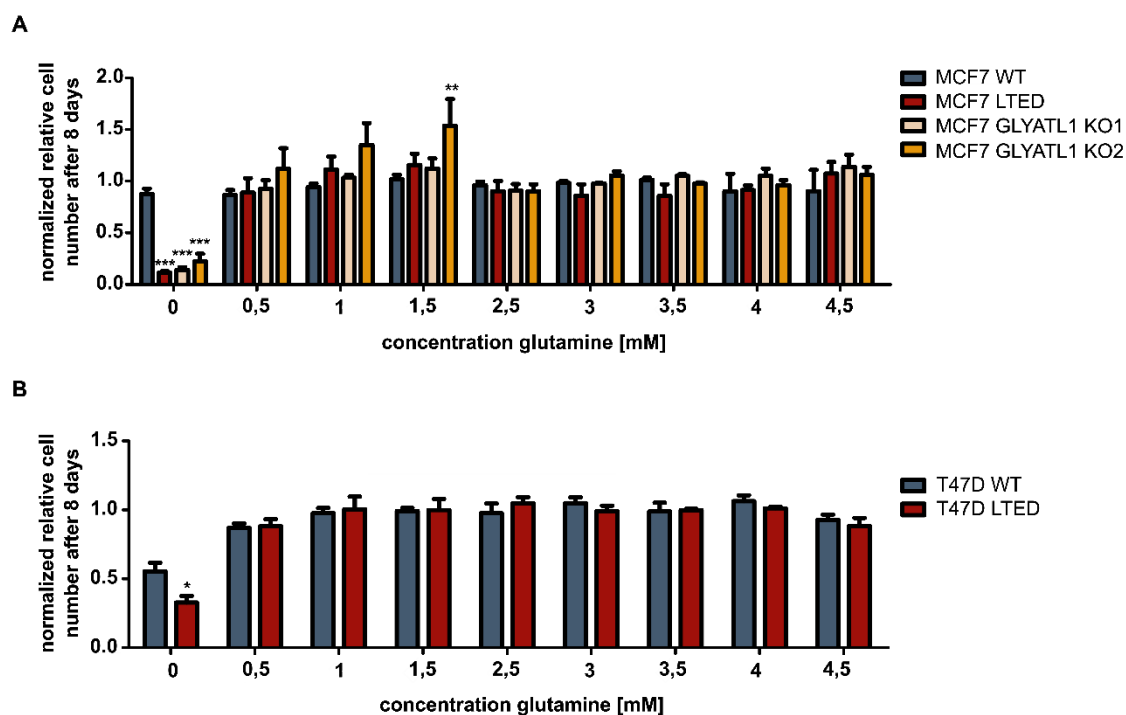


**Figure 26: Glutamine dependency of wildtype, LTED, and *GLYATL1* knockout cells.** MCF7 (A) and T47D (B) wildtype (WT), aromatase inhibitor-resistant (LTED), and two *GLYATL1* knockout (KO) cell lines were cultivated in media with varying glutamine concentrations for eight days. The proliferation rate was measured via microscopy-based nuclear count. Proliferation was normalized on cells growing in 2 mM glutamine (normal growth condition). Data are presented as mean  $\pm$  SEM of 3 biological replicates (each with 6 technical replicates). Statistical significance was assessed using two-way ANOVA with Bonferroni post-test. Indicated significance levels are compared to WT, where \*\*\* indicates  $p < 0.001$ , \*\* indicates  $p < 0.01$ , and \* indicates  $p \leq 0.05$ .

The wildtype cells displayed consistent proliferation rates regardless of glutamine levels. In contrast, LTED and both *GLYATL1* knockout cell lines exhibited a significant decrease in growth rate when cultured in glutamine-deficient media compared to wildtype. However, the proliferation rate was not significantly altered between the LTED and *GLYATL1* knockout cell lines. This reduced proliferation indicates a dependence on glutamine in both LTED and *GLYATL1* knockout cells. The similarity in de-

pendence observed between the knockout cells and LTED cell lines, however, suggests that *GLYATL1*, and its potential catalytic activity, are not inducing the glutamine dependency.

Similar to MCF7, the proliferation of T47D wildtype and LTED cells remained unaffected by high glutamine concentration. Under glutamine-depleted conditions, both wildtype and LTED cells exhibited a decrease in proliferation with a significantly lower proliferation in the LTED cells (Figure 26B).

In collaboration with Dr. Lisa Schlicker from the Almut Schulze lab at the DKFZ, I next attempted to determine the potential acyl donor of the *GLYATL1*-catalyzed reaction. To this end, we measured the levels of various intracellular N-acyl-CoA species in wildtype, resistant, and *GLYATL1* knockout MCF7 cell lines (Figure 27).

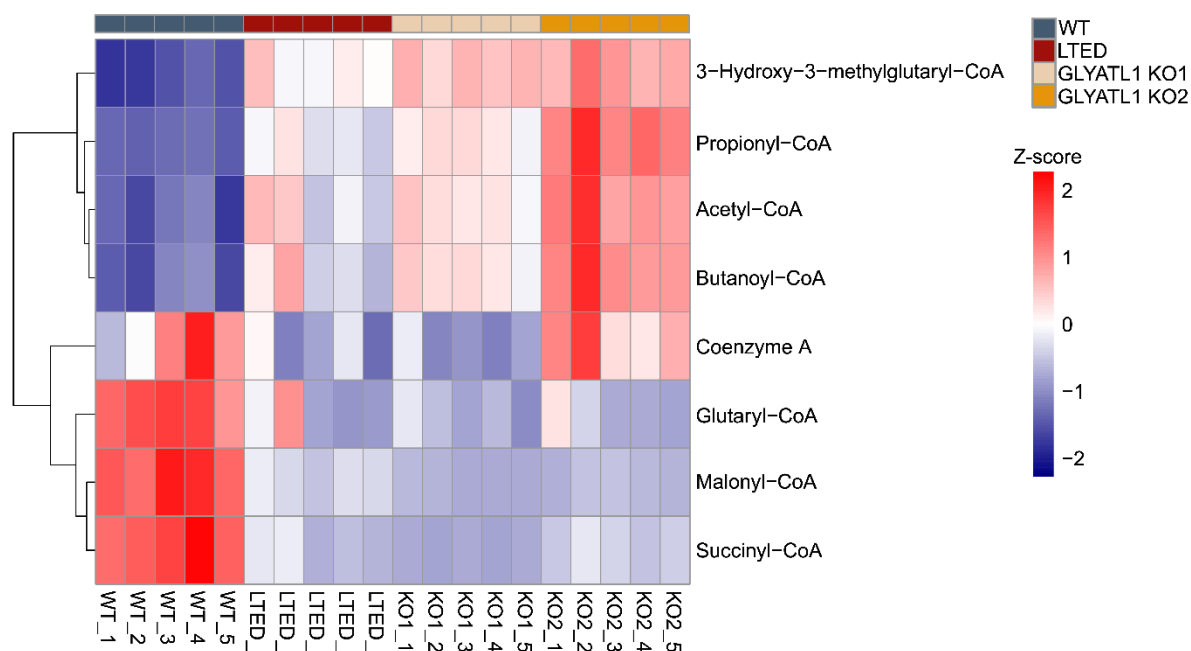


**Figure 27: Altered abundance of various intracellular Acyl-CoA species.** Heatmap showing z-scored values of various acyl-CoA species measured via LC-MS in MCF7 wildtype (WT), aromatase inhibitor-resistant (LTED), and two *GLYATL1* knockout (KO) cell lines. The signal was normalized on internal standard and protein concentration. Samples were measured and pre-processed by Dr. Lisa Schlicker. Biological replicates (n=5) are displayed separately.

Significant differences were observed between wildtype and resistant cells. In particular, a significant accumulation of acetyl-, propionyl-CoA, and 3-Hydroxy-4-methylglutaryl-CoA was observed in the LTED cells. Conversely, Coenzyme A levels were significantly decreased in LTED compared to WT cells.

In contrast, no accumulation of any specific N-acyl-CoA species was observed in *GLYATL1* knockout clone 1. However, *GLYATL1* knockout clone 2 exhibited a significant accumulation of Co-A, acetyl-CoA, and propionyl-CoA in KO2 in comparison to LTED. Since this accumulation was only observed in one knockout clone, this effect might be independent of *GLYATL1* but rather attributed to clonal variability or potential compensatory mechanisms in the clones. Taken together these results indicate significant changes in acyl-CoA abundances in LTED cells compared to wildtype. However, these changes are stable irrespective of *GLYATL1* expression indicating that *GLYATL1* does not influence the levels of the measured acyl-CoA and potentially not use them as acyl donors.

To evaluate the influence of *GLYATL1* on the global metabolome, we measured water-soluble metabolites to identify pathways potentially affected by *GLYATL1*. As one (out of five) LTED replicates exhibited poor signal, this sample was excluded from the subsequent statistical analysis. Principal component analysis (PCA) revealed distinct clustering of wildtype, resistant, and *GLYATL1* knockout cell lines samples, with the greatest separation observed along the PC1 axis. This shift along the PC1 axis separating wildtype from the other cell lines explained about ~67% of the total variance (Figure 28). A shift in the PC2 axis separates the samples of the *GLYATL1* KO2 cell line from the LTED and *GLYATL1* KO1 samples, indicating that *GLYATL1* KO1 displays a more similar metabolically profile to LTED than to knockout clone 2. This finding was previously observed in the analysis of different acyl-CoAs.

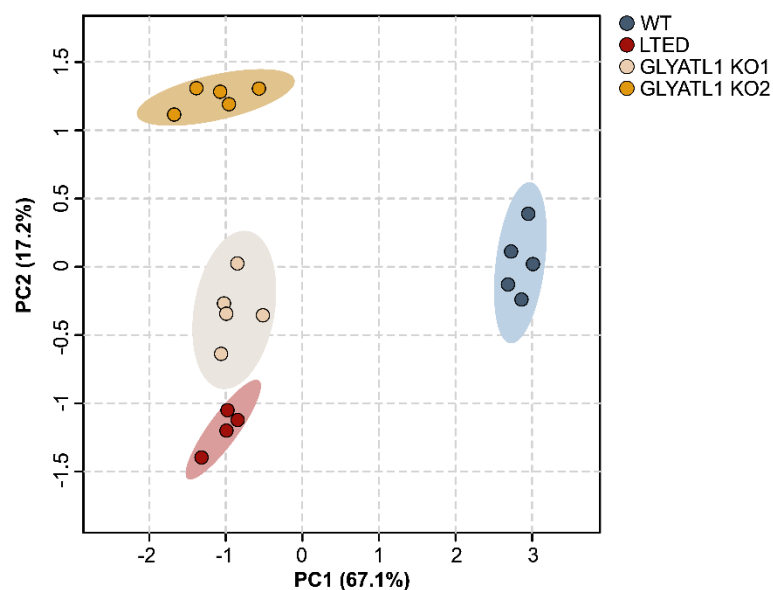


**Figure 28: Principal component analysis of full metabolome data.** The first two principal components are plotted explaining 67.1% (PC1) and 17.2% (PC2) variance. Biological replicates ( $n \geq 3$ ) are indicated as individual dots in their respective color. Data was measured by Dr. Lisa Schlicker. Analysis was performed using Metaboanalyst v 5.0 [163].

The analysis of the water-soluble metabolites in the measured MCF7 cell lines revealed significant differences across the conditions (Figure 29A). In particular, wildtype cells exhibited elevated levels of most metabolites compared to LTED samples. Out of the 91 measured and identified metabolites, 58 metabolites were significantly elevated in the wildtype cells with an adjusted p-value smaller equal 0.05. Only succinic acid showed significant enrichment in the LTED cells. Conversely, the intracellular levels of succinic acid were significantly diminished in both *GLYATL1* knockout cell lines compared to LTED cells. Additionally, both *GLYATL1* knockout cell lines displayed significant alterations in an additional 21 metabolites, where 17 of these metabolites showed a significant reversion in intracellular levels in the LTED cells compared to wildtype cells.

# Results

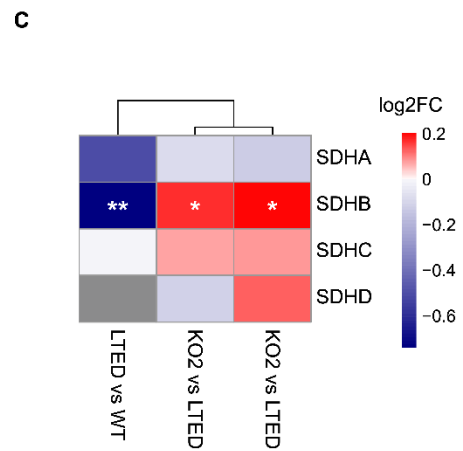
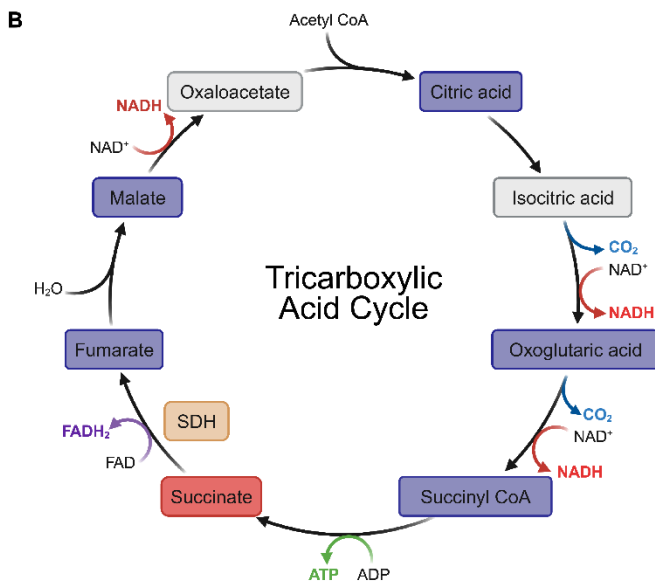
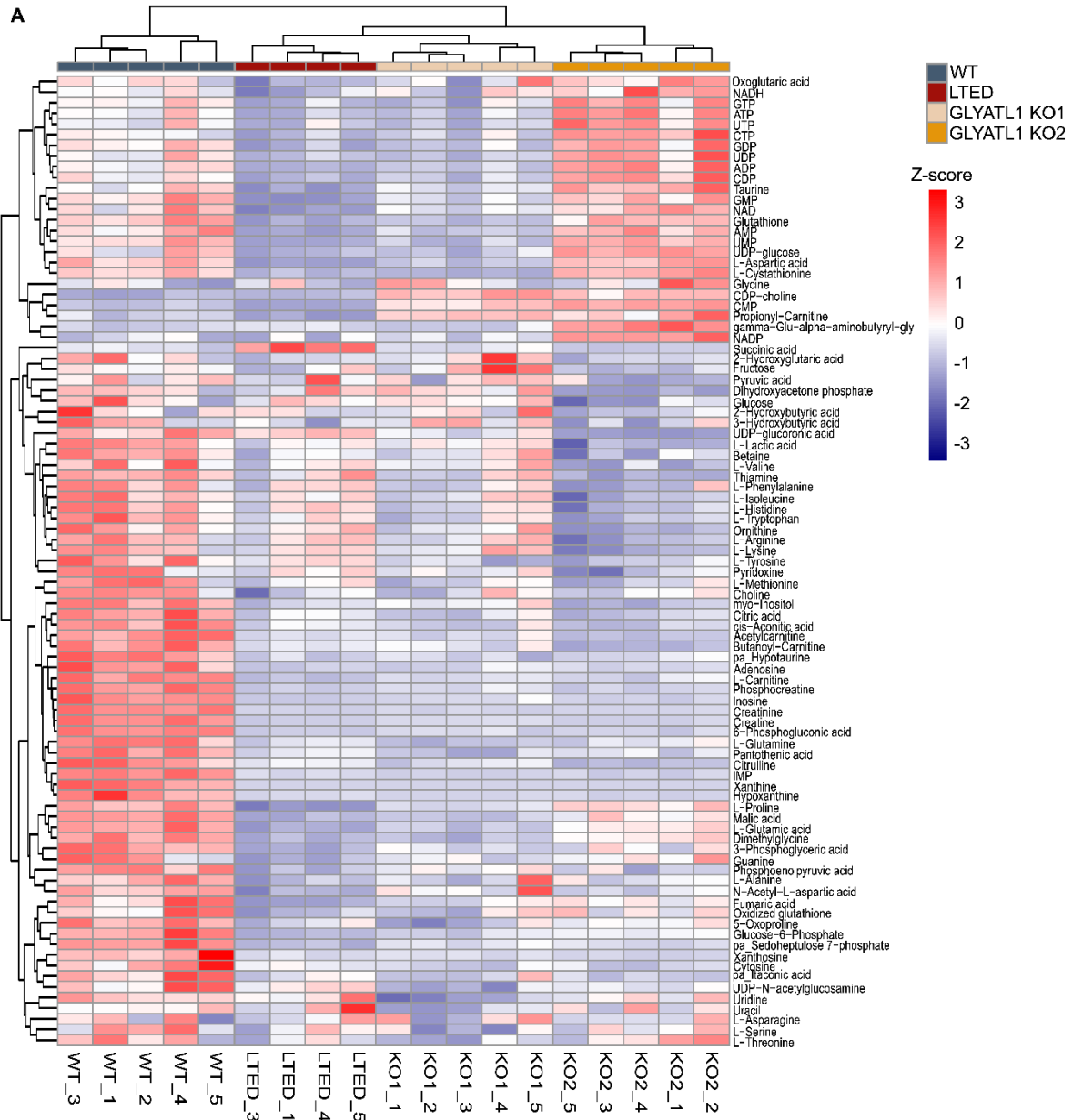


**Figure 29: Full metabolome of wildtype, resistant, and *GLYATL1* knockout MCF7 cell lines.** (A) Hierarchically clustered heatmap showing z-scaled intensities of all measured metabolites. Biological replicates ( $n \geq 3$ ) are displayed separately. (B) Schematic illustration of the tricarboxylic acid cycle. Colors represent higher (red) or lower (blue) abundance of intermediates in LTED cells compared to wildtype cells. Abundance of Intermediates in grey boxes was not determined in this study. The enzyme succinate dehydrogenase (SDH) complex catalyzes the conversion of succinate to fumarate. Scheme was adapted from Haddad et al. [178] and modified with BioRender.com. (C) Heatmap displaying  $\log_2$  fold-changes ( $\log_2FC$ ) in RNA levels of the SDH complex members determined by RNA sequencing. Positive  $\log_2$  fold-changes are indicated in red, negative  $\log_2$  fold-changes are indicated in blue, and undefined levels are colored in grey. Statistical significance is indicated by asterisks with adjusted p-values \*\*  $p < 0.01$ , and \*  $p < 0.05$

Among the metabolites involved in the tricarboxylic acid cycle (TCA), all analyzed intermediates were commonly less abundant in the LTED cells compared to wildtype with the only acceptance of succinic acid, which significantly accumulated (Figure 29B). In contrast, in the *GLYATL1* knockout cell lines, the abundances are reverted in all intermediates except citrate, where the  $\log_2$  fold-change remained negative, however not significant. In the TCA cycle, succinate is converted into fumarate by the succinate dehydrogenase (SDH) complex, which consists of multiple subunits specifically SDHA, SDHB, SDHC, and SDHD [179]. In line with the accumulation of succinate in the LTED cells compared to wildtype cells, differential gene expression analysis of RNA sequencing data, generated by Dr. Emre Sofyali and me, revealed a significant downregulation of *SDHB* in the LTED cells, which is converted in the *GLYATL1* knockout cells (Figure 29C). Furthermore, *SDHC* was found to follow a similar trend not reaching significant levels. These transcriptomic changes could indicate that the impaired succinate dehydrogenase activity, primarily attributed to reduced *SDHB* and *SDHC* expression, enhanced succinate accumulation in the LTED cells, which is affected by *GLYATL1* expression.

To further explore these metabolic changes, Luisa Schwarzmüller and I performed two independent pathway enrichment analyses using metabolites that showed a significant ( $p_{adj} \leq 0.05$ ) increase or decrease in  $\log_2$  fold-changes. However, neither analysis showed significant differences of any distinct pathway between LTED and wildtype samples or between the *GLYATL1* knockout cell lines and LTED cells (Data not shown).

In summary, I observed a glutamine dependence in LTED and both *GLYATL1* knockout cell lines, suggesting that this dependence is independent of *GLYATL1* and its potential catalytic activity. Furthermore, significant differences in various acyl-CoA species were measured between wildtype and LTED. However, no common accumulation of any measured acyl-CoA species was observed in both knockout cell lines, indicating that *GLYATL1* may not utilize any of the analyzed acyl-CoA species as a substrate. An analysis of water-soluble metabolites revealed significant alterations between the different cell lines, especially between wildtype and LTED with minor changes in *GLYATL1* knockout cell lines. However, these changes did not converge on specific metabolic pathways but indicated a striking accumulation of succinate exclusively in the LTED cells.

### 4.12 Effect of *GLYATL1* on Reactive Oxygen Species

Besides the involvement in metabolic pathways, mitochondrial proteins also balance the abundance of intracellular reactive oxygen species (ROS) to prevent cellular damage and maintain redox homeostasis. These mitochondrial proteins contribute to the generation of ROS and quench ROS levels via antioxidant defense mechanisms [180-182]. By modulating ROS levels, mitochondrial proteins thus help manage levels of oxidative stress within the cell, which arises from an imbalance between antioxidants and oxidants in favor of oxidations, leading to disrupted redox signaling [183].

To test the hypothesis that *GLYATL1* might influence the abundance of intracellular reactive oxygen species, I measured the basal oxidative stress levels in MCF7 wildtype, LTED, and the two *GLYATL1* knockout cells using the fluorescence probe CellROX (Figure 30). Flow cytometric analysis revealed remarkably decreased oxidative stress levels upon resistance (WT versus LTED), although this decrease was not significant due to the high variance of the assay. Furthermore, basal oxidative stress levels increased upon *GLYATL1* knockout. The increase was significant in *GLYATL1* KO2 cells, with KO1 cells showing a similar trend. The drop in oxidative stress levels upon resistance towards aromatase inhibition was confirmed in T47D cells. This anti-correlation of *GLYATL1* expression and basal oxidative stress levels suggests that

GLYATL1 negatively influence intracellular ROS levels, which might consequently lead to different downstream signaling.

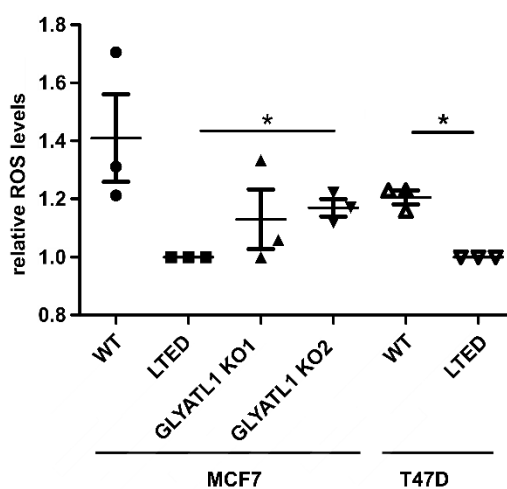


**Figure 30: Basal oxidative stress levels in MCF7 and T47D cells.** Levels were measured via flow cytometry assay using the fluorescent CellROX probe in indicated MCF7 and T47D cells. Living cells were gated and the median signal of the FL3 channel was calculated. Data are presented as mean  $\pm$  SEM of 3 biological replicates. Statistical significance was assessed using one sample t-test, where \* indicates  $p < 0.05$ .

The increase in ROS causes the question of which ROS species is influenced by GLYATL1. To assess the effect of GLYATL1 on  $H_2O_2$  species, I utilized the redox-sensitive green fluorescent protein variant (roGFP2) sensor fused to  $H_2O_2$ -specific peroxidase Orp1, gifted by Prof. Dr. Tobias Dick's group. Upon interaction of  $H_2O_2$  with Orp1, the catalytic cysteine of Orp1 is oxidized by  $H_2O_2$ , resulting in the formation of an intramolecular disulfide bridge. Consequently, Orp1 mediates proximity-based oxidation through a thiol-disulfide exchange mechanism, resulting in the formation of a disulfide bridge on the adjoining roGFP2. This formation results in a shift of the excitation spectrum of roGFP2 from approximately 490 nm to around 405 nm (Figure 31A). Consequently, the fluorescence ratio of 400/490 nm excitation at 520 nm emission indicates the redox changes in roGFP2 and can be employed to monitor intracellular alterations in  $H_2O_2$ -specific ROS levels [184-187].

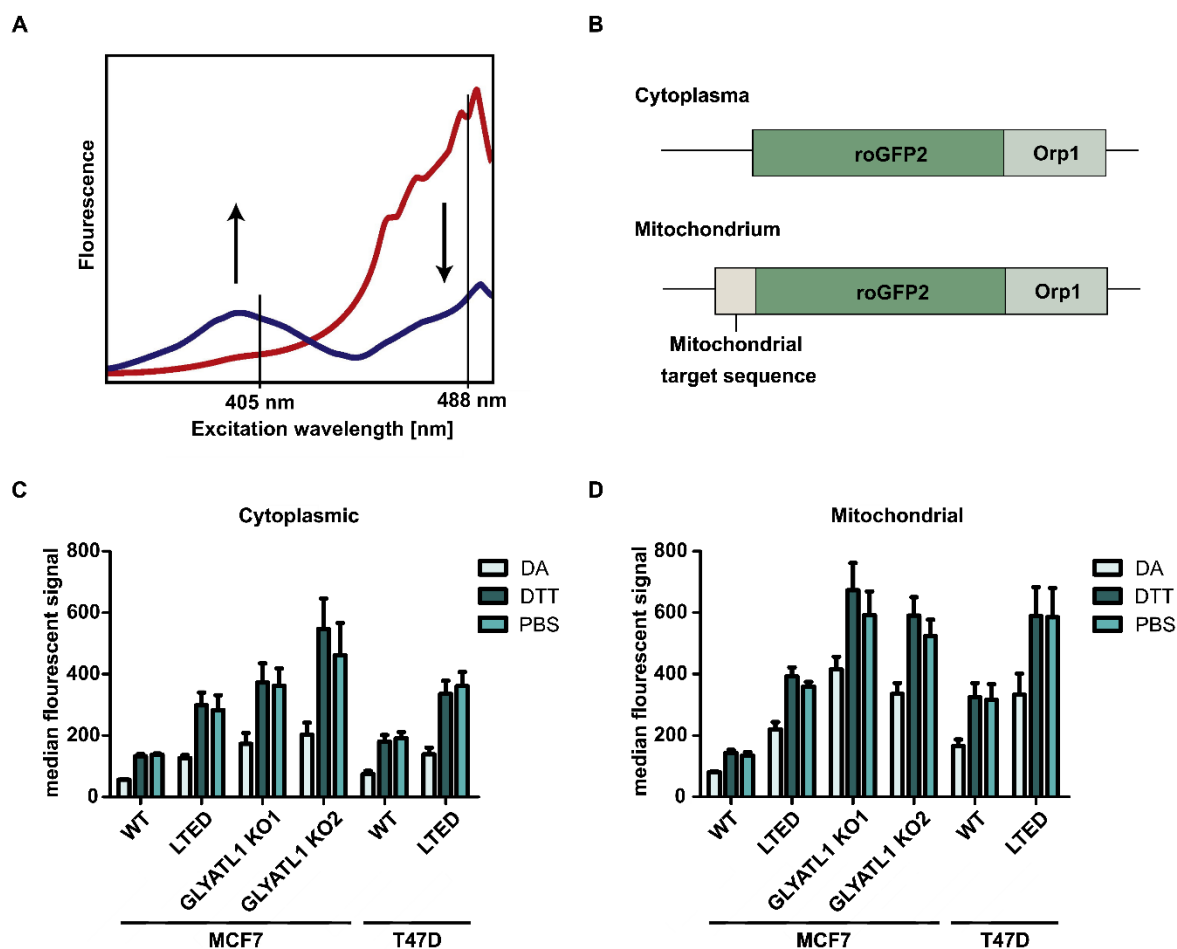


**Figure 31: H<sub>2</sub>O<sub>2</sub>-specific ROS levels.** (A) The excitation spectrum of roGFP2 sensor, adapted from Morgan et al [186]. Blue line represents the excitation spectrum of the oxidized sensor and the red line represents the excitation spectrum of the reduced sensor. (B) Schematic illustration of roGFP2-Orp1 constructs. (C) Result of FACS experiment using cytoplasmic and mitochondrial (D) roGFP2-Orp1 sensor in indicated cell lines. Median fluorescence of living cells is displayed after treatment with 10 mM dithiothreitol (DTT), to completely reduce the sensor, 1 mM diamide (DA), to completely oxidize the sensor, or untreated (PBS). Mean of three biological replicates (n=3) ± SEM is displayed.

In addition to investigating cytosolic changes in H<sub>2</sub>O<sub>2</sub>-specific ROS species, changes in the mitochondrial cell compartment were investigated by an introduced mitochondrial target sequence at the N-terminus of the roGFP2-Orp1 construct (Figure 31B). In collaboration with the Cellular Tools Core Facility, we utilized these plasmids to generate MCF7 and T47D wildtype, LTED, and *GLYATL1* knockout cell lines stably expressing either cytosolic or mitochondrial localized sensor.

To test the functionality of the sensor, I performed a flow cytometry analysis on the different cell lines using 488 nm excitation to measure the signal of the reduced sensor. The signal range was examined by treating the cells with either 10 mM dithiothreitol (DTT) to completely reduce the sensor or 1 mM diamide (DA) to completely oxidize the sensor. Basal levels were measured with untreated cells (PBS) (Figure 31C, D).

The sensor roGFP2 exhibited an elevated fluorescent signal in all cell lines following DTT treatment and a significant reduction in signal intensity following complete oxidation, thereby verifying the sensor's proper functionality. Values from untreated samples showed high fluorescent signals, indicating low levels of H<sub>2</sub>O<sub>2</sub>-specific ROS levels. Across all cell lines, the relative levels towards DTT showed only marginal changes, indicating that basal levels exhibited similar signal intensities as in the completely reduced sample suggesting that the cells were not highly stressed. However, the sensor intensity exhibited notable variability between the different cell lines, necessitating normalization for comparison between different cell lines. Therefore, the ratio of basal levels and fully reduced sensor (DTT conditions) were calculated (Figure 32A, B). While the mitochondrial sensor demonstrated no significant alterations between the different cell lines (Figure 32B), analysis of the cytoplasmic H<sub>2</sub>O<sub>2</sub>-specific ROS species revealed a small yet statistically significant increase in the signal ratio between LTED and *GLYATL1* knockout 2 cells (Figure 32A).

To further evaluate this change, I tested the cells harboring the cytoplasmic sensor in the GloMax® Discover microplate reader, which allows excitation at 405 and 475 nm. However, the ratio of reduced and oxidized sensor (405/475 nm), did not show any significant changes between the different cell lines, suggesting that H<sub>2</sub>O<sub>2</sub>-specific ROS species appear to be unaffected by *GLYATL1* (Figure 32C). Given that previous analysis using the CellROX sensor has demonstrated increased oxidative stress levels upon *GLYATL1* knockout, this suggests that *GLYATL1* may influence other ROS species than H<sub>2</sub>O<sub>2</sub> such as superoxide or hydroxyl radicals.

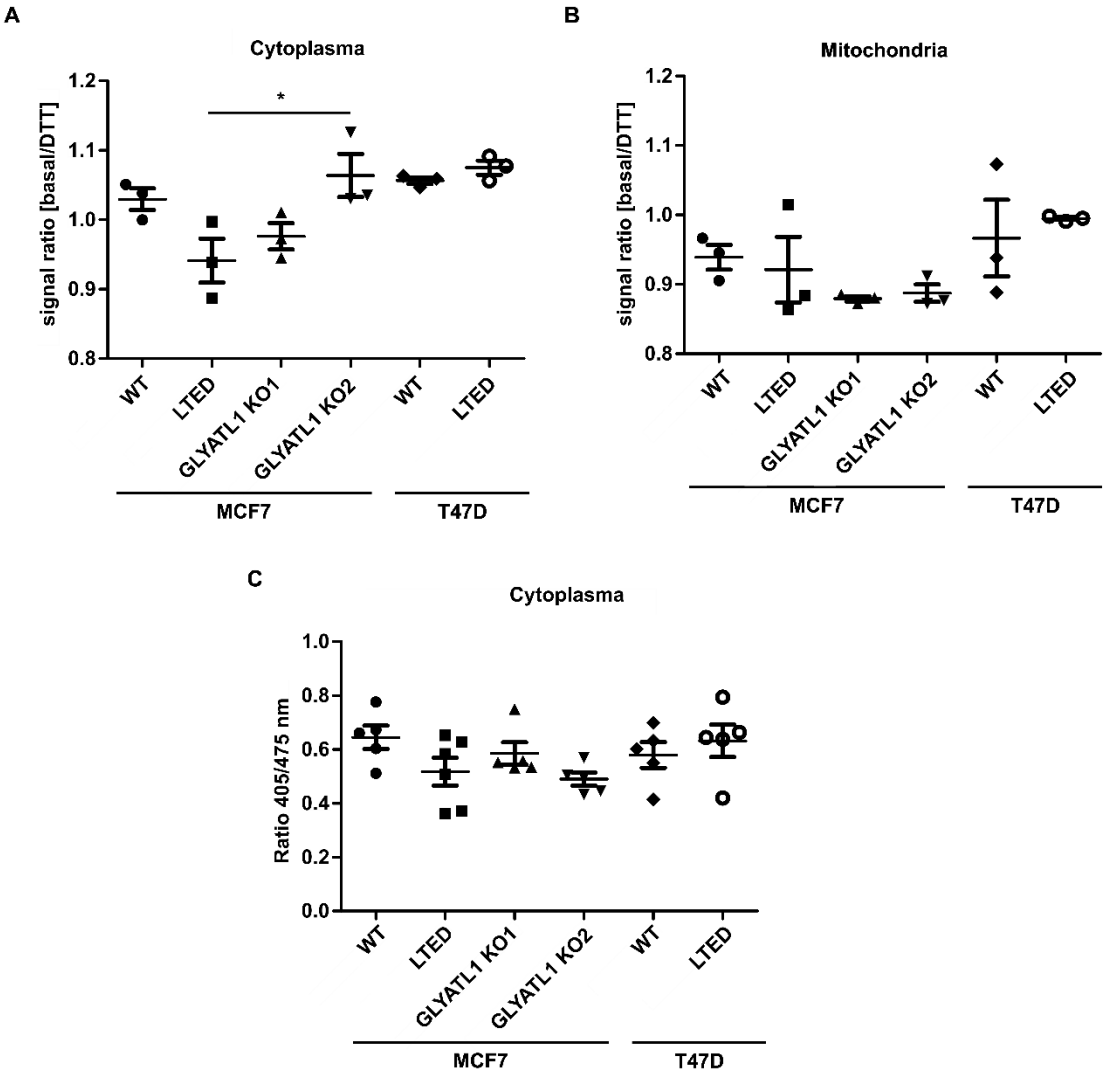


**Figure 32: Cytoplasmic and mitochondrial H<sub>2</sub>O<sub>2</sub>-specific ROS levels.** Levels in indicated cell lines stably expressing roGFP2-Orp1 construct without (A) or with (B) mitochondrial localization sequence were measured in flow cytometry-based assay and relative levels towards treatment with 10 mM dithiothreitol (DTT) were calculated (A, B). Levels of cytoplasmic H<sub>2</sub>O<sub>2</sub>-specific ROS were further measured excitation at 405 and 475 nm. Data is presented as mean of three (A, B) or five (C) biological replicates (with 6 technical replicates for (C)) ± SEM. Statistical significance was assessed using one-way ANOVA, where \* indicates p<0.05.

### 4.13 Downstream Effect of Resistance on Epigenetic Modifier

Having observed a GLYATL1-mediated change in oxidative stress levels, I next attempted to analyze potential downstream effects. It is well established that free radicals can influence the epigenetic landscape in various ways, including different histone modifications, with a particular emphasis on acetylation.

ROS can modulate the enzymatic activity of various histone acyltransferases (HATs) and histone deacetylases (HDACs). Histone acetyltransferases mediate histone acetylation, which is associated with open chromatin and gene activation. In contrast, histone deacetylases remove acetyl groups from histones, leading to chromatin condensation and transcriptional repression [188]. ROS can induce post-translational modifications on these histone-modulating proteins affecting their activity and cellular localization [189, 190]. Additionally, redox-sensitive transcription factors can regulate the expression or activity of HDACs and HATs in a ROS-dependent manner or influence the availability of required cofactors. Consequently, histone acetylation plays a crucial role in the cellular response to oxidative stress by the chromatin status and consequently the transcription of antioxidant genes [189, 191, 192].

To assess the potential influence of epigenetic modifiers in the context of resistance towards aromatase inhibition on histone acetylation, I analyzed changes in the expression of histone-modifying genes. RNA sequencing data, generated by Dr. Emre Sofyali, had revealed significant alterations in the expression of various lysine acetyltransferases (KATs), sirtuins (SIRTs), and histone deacetylases (HDACs) between the resistant and the parental wildtype cells (Figure 33A).

Among the most upregulated lysine acyltransferases, *KAT2B* exhibited significant upregulation in MCF7 LTED cells, while *KAT6B* showed significant downregulation in the same cells. Conversely, T47D cells displayed an inverted expression pattern for these two lysine acetyltransferases. Additionally, *HDAC9* demonstrated a significant upregulation in T47D LTED cells with MCF7 LTED cells showing the same trend, not reaching significance.

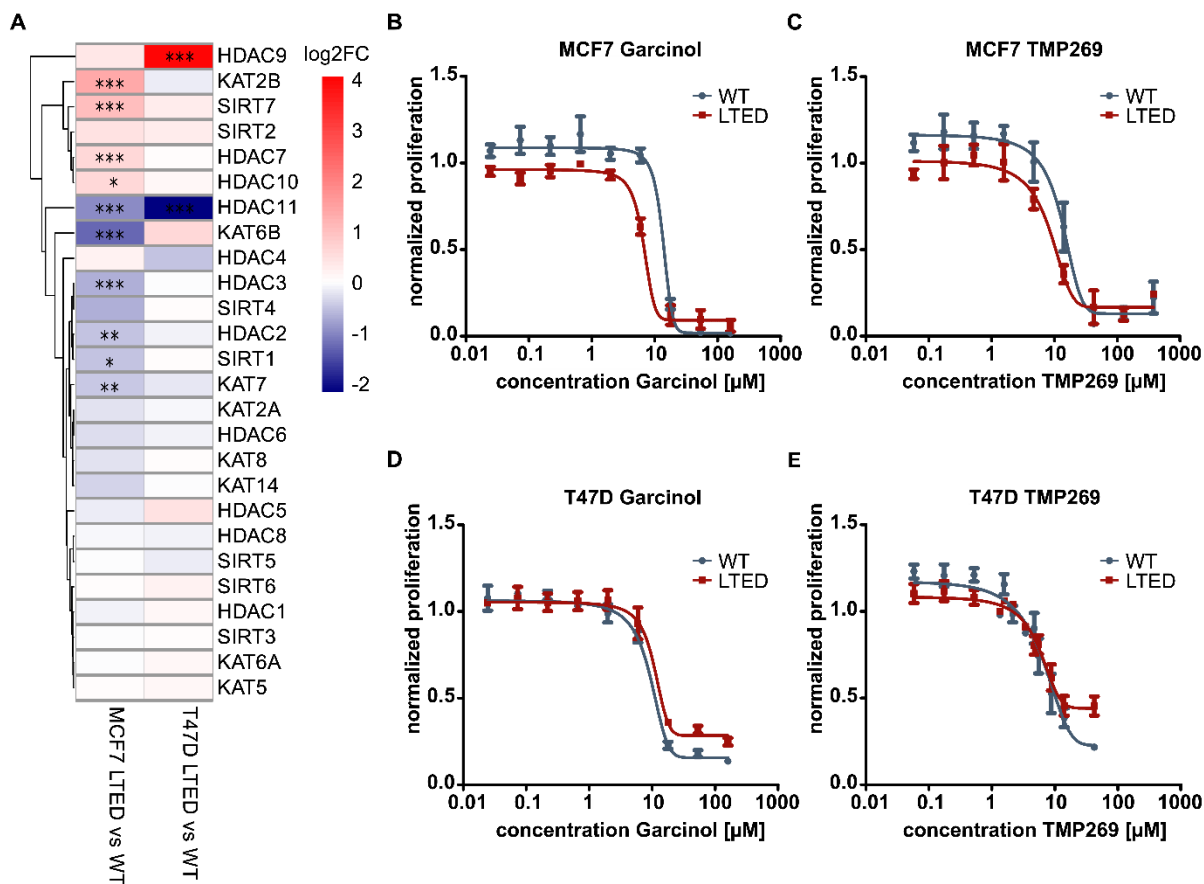


**Figure 33: Altered HDAC and KAT expression and IC<sub>50</sub> determination of specific inhibitors.** (A) Heatmap of log 2-fold changes (log<sub>2</sub>FC) in gene expression in response to long-term estrogen deprivation derived from RNA sequencing data generated by Dr. Emre Sofyali. (B, C, D, E) Dose-response curve of garcinol (B, D) and TMP269 (C, E) in MCF7 (B, C) and T47D (D, E) wildtype (blue) and LTED (red) cells. The proliferation rate was measured via nuclear count after eight days and normalized on DMSO control. Data are presented as mean ± SEM of 3 biological replicates (each with 6 technical replicates). Statistical significance is indicated by asterisks with adjusted p-values \*\*\* p < 0.001 \*\*, p < 0.01, and \* p < 0.05.

To study the effects of inhibiting these factors on cell proliferation, small molecule inhibitors Garcinol, targeting KAT2B [146], and TMP269, targeting HDAC4, HDAC5, HDAC7, and HDAC9 [147], were utilized. Initially, I determined the IC<sub>50</sub> values for both wildtype and resistant cells (Figure 33B-E) by evaluating the effect of varying inhibitor concentrations on proliferation. MCF7 LTED cells exhibited a lower IC<sub>50</sub> value compared to wildtype cells, indicating higher sensitivity to both inhibitors. Specifically, the IC<sub>50</sub> value for Garcinol decreased from 11.74 μM in wildtype cells to 7.09 μM in LTED

cells. Similar effects were observed with the HDAC5/9 inhibitor TMP269, where the IC50 values decreased from 13.45  $\mu\text{M}$  in wildtype cells to 7.28  $\mu\text{M}$  in LTED cells. No significant changes were found in T47D (Table 9).

**Table 9: Summary of experimental determined IC50 values of Garcinol and TMP269.**

Dose-response experiments (Figure 33) were performed to determine IC50 and Confidence Intervals (CI) in MCF7 and T47D cell lines (n=3).

Target	Inhibitor	MCF7 WT IC50 $\pm$ (CI) [ $\mu\text{M}$ ]	MCF7 LTED IC50 $\pm$ (CI) [ $\mu\text{M}$ ]	T47D WT IC50 $\pm$ (CI) [ $\mu\text{M}$ ]	T47D LTED IC50 $\pm$ (CI) [ $\mu\text{M}$ ]
KAT2B	Garcinol	11.74 (9.402 to 14.67)	7.09 (6.035 to 8.318)	8.60 (7.218 to 10.25)	9.49 (7.334 to 12.28)
HDAC5/9	TMP269	13.45 (10.28 to 17.58)	7.28 (4.764 to 11.12)	6.64 (4.640 to 9.507)	5.75 (4.530 to 7.305)

Next, I investigated the effects of inhibiting KAT2B and HDAC4/5/7/9 in media with or without estrogen. The respective IC50 concentrations determined in the corresponding LTED cells were utilized and proliferation was monitored in wildtype and LTED cells over eight days in media containing estrogen and media depleted of estrogen (Figure 34). No significant differences were observed following the inhibition of HDAC4/5/7/9 using TMP269 in MCF7 cells, as well as in T47D cells. In contrast, Garcinol led to a significant reduction in proliferation in MCF7 LTED cells. Moreover, the effect was attenuated upon the presence of estrogen in the growth media as indicated by higher proliferation rate suggesting an increased importance of KAT2B after estrogen deprivation. T47D LTED did not show any significant changes in response to Garcinol treatment. However, Garcinol significantly diminished proliferation in T47D wildtype cells growing with estrogen compared to estrogen-depleted conditions.

Together these data suggest that KAT2B appears to be more critical in MCF7 LTED cells, while the role of KAT2B in T47D wildtype cells depends on the presence of estrogen. Since no significant effect of HDAC4/5/7/9 inhibition in all tested conditions was observed, this led to the suggestion that these HDACs may not be the major regulators of proliferation in MCF7 as well as in T47D cells.

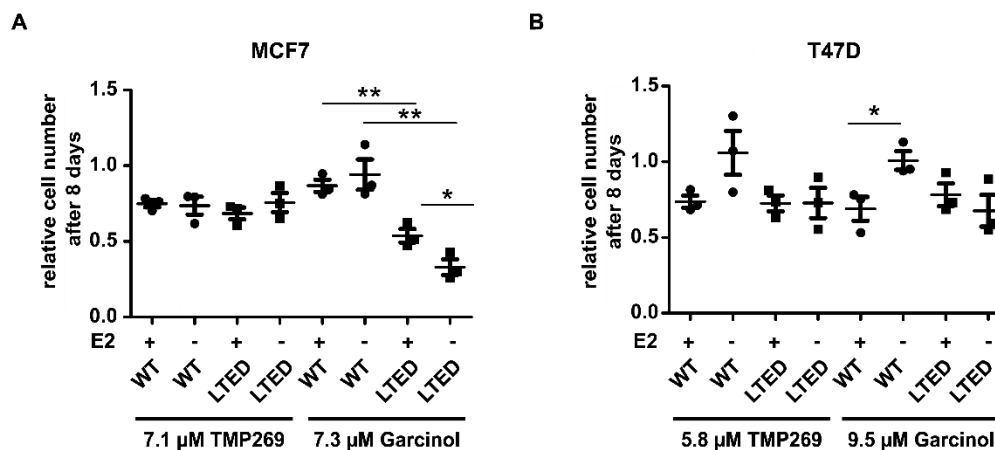


**Figure 34: Effect of HDAC and KAT inhibition on proliferation.** The effect of HDAC 4/5/7/9 inhibition by TMP269 and KAT2B inhibition by Garcinol was analyzed in MCF7 (A) and T47D (B) wildtype and resistant cell lines in the presence and absence of estrogen (E2). The proliferation rate after eight days was measured via nuclear count and normalized on DMSO control. Data are presented as mean  $\pm$  SEM of 3 biological replicates (each with 6 technical replicates). Statistical significance was assessed using unpaired Student's t-test, where \*\* indicates  $p < 0.01$ , and \* indicates  $p < 0.05$ .

Since no specific inhibitor for KAT6B was available, a pool of different siRNAs was utilized to knockdown *KAT6B* expression. Following transfection, knockdown efficiency was tested via RT-qPCR revealing a significant knockdown of 60 to 70% (Figure 35C). While knockdown of *KAT6B* resulted in no significant changes in proliferation in wildtype MCF7 cells, in a significant increase in proliferation was measured in MCF7 LTED cells, regardless of the presence or absence of estrogen (Figure 35A). Similar effects were observed in T47D cells (Figure 35B). Taken together, these data indicate that KAT6B may exert a negative influence on proliferation, specifically in resistant cells, but not in wildtype cells.

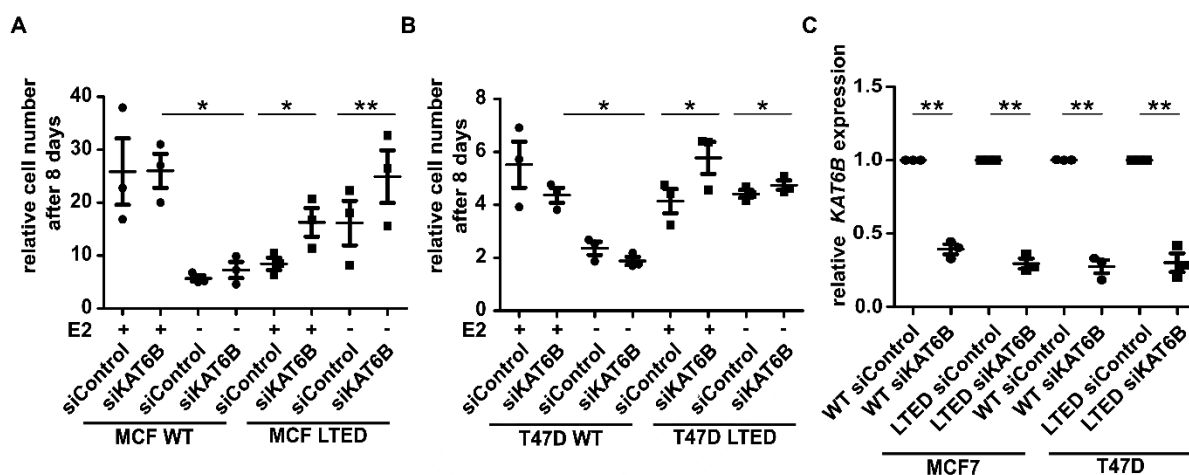


**Figure 35: Effect of *KAT6B* knockdown on proliferation.** A pool of siRNAs was used to knockdown *KAT6B* and the effect on proliferation after eight days was tested via microscopy-based nuclei count in MCF7 (A) and T47D (B) wildtype and LTED cell lines. Cells were cultured during this period in the presence or absence of estrogen (E2). Knockdown efficiency was verified by RT-qPCR (C). Values of mRNA expression were normalized on *ACTB* and *PUM1* levels. Data are represented of mean  $\pm$  SEM of 3 biological replicates (each with 6, proliferation assay, or 3, RT-qPCR, technical replicates). Statistical significance was assessed using paired Student's t-test, where \*\* indicates  $p < 0.01$ , and \* indicates  $p < 0.05$ .

#### 4.14 Global Changes in the Epigenetic Landscape

Having observed the influence of *KAT2B* and *KAT6B* on proliferation in the context of resistance towards aromatase inhibitors, we next sought to investigate their downstream effects on the epigenetic landscape. *KAT2B* is known to catalyze the acetylation of histone residue H3K9 along with H3K14 [193, 194]. To investigate this, Dr. Emre Sofyali conducted an ELISA experiment to assess the acetylation status of H3K9 and H3K14 histone residues in MCF7 wildtype and LTED cells. The results revealed an increase in histone H3K9 and H3K14 acetylation in LTED cells compared to wildtype cells (Figure 36A, B) [131].

Additionally, Dr. Emre Sofyali performed a *GLYATL1* knockdown to investigate the influence of *GLYATL1* on these histone residues. Upon *GLYATL1* knockdown in MCF7 LTED cells, both H3K9 and H3K14 exhibited a more deacetylated status, indicating that *GLYATL1* plays a role in modulating the acetylation of these histone residues and thereby affecting the epigenetic landscape (Figure 36C, D). These results collectively

## Results

suggest that H3K9 and H3K14 are acetylated under estrogen-deprived conditions and that GLYATL1 is indirectly involved in the regulation of these modifications. This highlights the potential impact of GLYATL1 on the epigenetic regulation of gene expression.

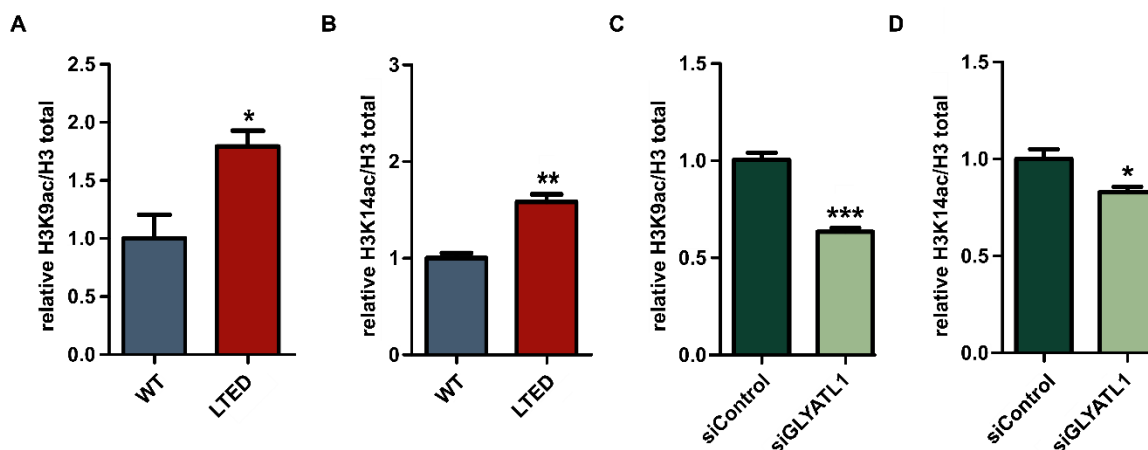


**Figure 36: Analysis of Histone 3 K9 and K14 acetylation levels.** H3K9ac (A) and H3K14ac (B) levels in wildtype and LTED MCF7 cells were detected by histone ELISA using purified core histones. (C, D) MCF7 LTED cells were transfected with a pool of siRNA targeting GLYATL1 (siGLYATL1) or non-targeting siRNAs (siControl). After 96 hours, core histones were purified. H3K9ac (C) and H3K14ac (D) levels were determined by histone ELISA and normalized to total H3 levels. Data are represented as mean  $\pm$  SD,  $n=3$  (each with 2 technical replicates). Statistical significance was assessed using unpaired Student's t-test, where \*\*\* indicates  $p < 0.001$ , \*\* indicates  $p < 0.01$ , and \* indicates  $p < 0.05$ . Data was generated and analyzed by Dr. Emre Sofyali.

To further investigate the levels of a broad range of histone modifications, I profiled the epigenetic landscape using an Epigenetic-focused cytometry by Time-of-Flight (EpiTOF) approach in cooperation with the Moshe Oren lab and the Flow Cytometry unit at the Weizmann Institute. This analytic technology incorporates concepts of flow cytometry with mass spectrometry and therefore allows multiplexed analysis of proteins at a single-cell level. To target epigenetic modifications, various metal-tagged antibodies targeting altered histone residues can be used to study a broad range of modifications [195, 196]. The custom-designed antibody panel consisted of three core histone antibodies for normalization, eight known cell identity markers to distinguish subpopulations, and sixteen antibodies targeting different histone modifications (Table 10).

**Table 10: Antibody panel of the EpiTOF experiment.** Panel consisted of antibodies targeting core histones, for subsequent normalization, eight cell identity markers, and sixteen histone modifications.

<b>Core histones</b>	<b>Cell identity markers</b>		<b>Histone modifications</b>	
H3	EpCAM	K5	H3K4me	H3K27me3
<b>H3.3</b>	<b>CD24</b>	<b>KI-67</b>	<b>H3K4me3</b>	<b>H3K36me2</b>
H4	CD49F	K8/18	H3K9ac	H3K36me3
	<b>CD44</b>	<b>ER</b>	<b>H3K9me</b>	<b>H3K64ac</b>
			H3K9me2	H4K16ac
			<b>H3K9me3</b>	<b>H4K20me3</b>
			H3K27ac	H2Aub
			<b>H3K27me2</b>	<b>pH3</b>

We conducted two separate EpiTOF runs, each involving MCF7 wildtype, LTED, and the two *GLYATL1* knockout clones. Data analysis was performed in collaboration with Dr. Eviatar Weizman and Luisa Schwarzmüller. Following arcsine transformation and data normalization based on the core histone markers H3 and H3.3, the median values for all cells within each cell line were calculated and compared. Due to insufficient staining for the antibody targeting H3K9 acetylation, this marker was excluded from further analysis.

Among the fifteen histone markers, four markers (H3K27ac, H3K27me2, H3K4me3, and H3K64ac) consistently exhibited a similar trend in both EpiTOF runs and demonstrated consistent changes in the same direction for the two knockout clones in each run (Figure 37). These markers exhibited significant alterations in their levels in response to resistance and showed reversed changes upon *GLYATL1* knockout. In particular, all changes (WT versus LTED and LTED versus KO) were statistically significant in batch 2, whereas in batch 1, the changes in H3K27ac and H3K4me3 did not reach significance in the comparison of WT and LTED.

These findings indicate that the observed changes in histone modifications, particularly H3K27ac, H3K27me2, H3K4me3, and H3K64ac, may be associated with the development of resistance and are influenced by the presence or absence of *GLYATL1*.

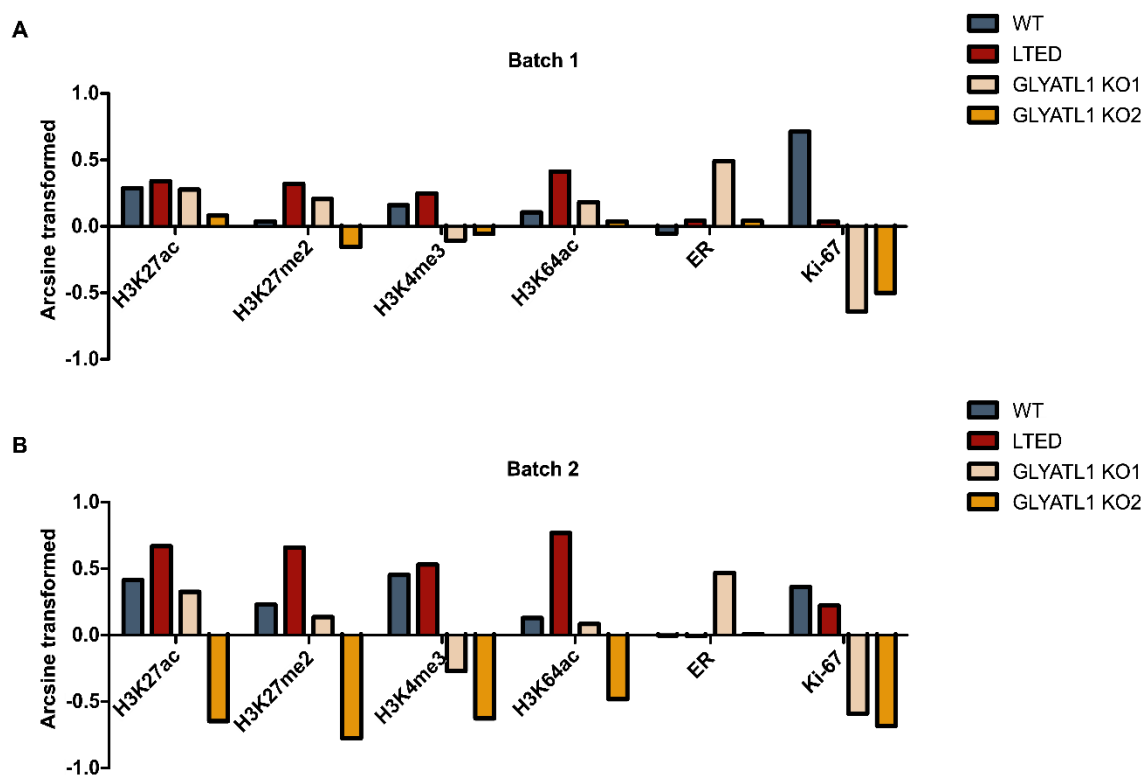


**Figure 37: Analysis of the Epigenetic profile and cell identity markers using EpiTOF.**

Two independent EpiTOF runs (A: batch 1, B: batch 2) were performed. Data was arcsine transformed and normalized on core histone H3 and H3.3. Median values per cell line were calculated and markers with similar patterns in both runs were displayed.

Additionally, the global analysis showed significant alterations in cell identity markers ER, and Ki-67. The estrogen receptor (ER) exhibited the highest levels in *GLYATL1* knockout clone 1, whereas clone 2 showed similar low levels, which were insignificantly different compared to LTED cells. The proliferation marker Ki-76 showed the highest levels in wildtype cells and decreased levels in LTED cells, with a further decrease upon *GLYATL1* knockout, consistent with the experimentally observed decrease in proliferation rate in both *GLYATL1* knockout cell lines (compare Figure 18).

To highlight the complex interplay between various histone modifications and cell identity markers, Spearman correlation matrices were generated (Figure 38).

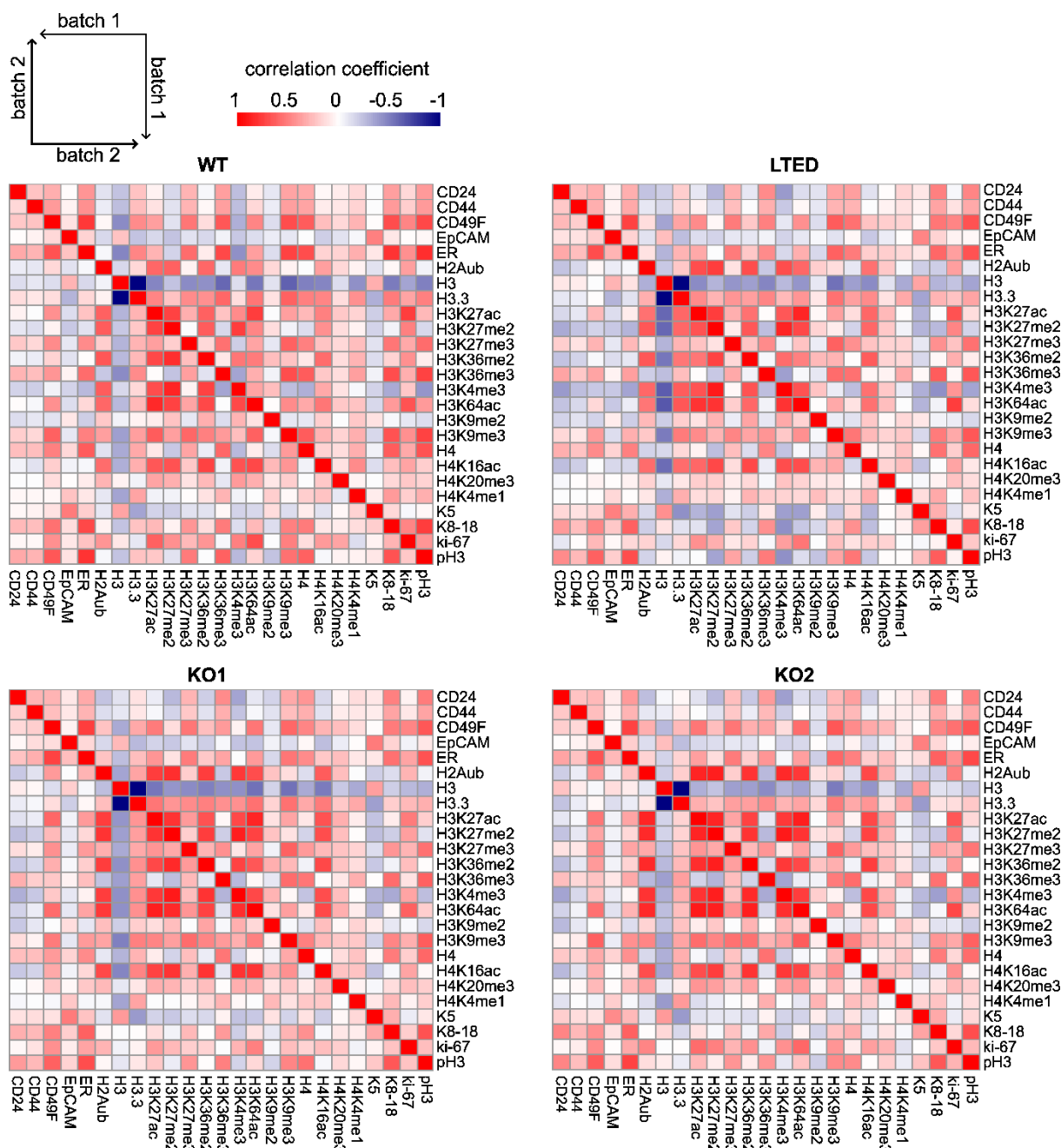


**Figure 38: Spearman Correlation Matrix of Histone Modifications and Cell Identity Markers from both EpiTOF run.** The heatmap displays Spearman correlation coefficients between various histone and cell identity markers in MCF7 WT, LTED, and two GLYATL1 knockout cell lines (KO1, KO2) using the data generated in both EpiTOF runs. Positive correlations are shown in red, while negative correlations are shown in blue. The diagonal represents self-correlations.

These correlation matrices unveiled consistent patterns across all cell lines and both experimental batches. Specifically, a consistently high correlation could be observed

## Results

---

between various histone marks including H3K27ac, H3K64ac, H3K4me3, H3K36me2, H3K16ac, H3K27me2, and H2Aub, suggesting a complex interplay between these histone modifications in regulating gene expression.

Moreover, the majority of the analyzed histone and cell identity markers exhibited a positive correlation with the non-canonical histone variant H3.3, while showing a negative correlation with the canonical histone H3. In contrast, the basal marker K5 displayed a consistent positive correlation with H3 and a negative correlation with H3.3.

In addition to the consistent patterns observed, there were slight differences between the two batches. In the first batch, the correlation coefficients for example H3K27ac with H3K4me3, H3K27me2 with H3K64ac, and H3K4me3 with H3K64ac were lower in wildtype cells compared to LTED and the two knockout cell lines, which could hint on functional alterations caused by resistance. However, these differences could not be replicated in the second EpiTOF run.

To gain insights into the epigenetic heterogeneity within the cell lines, we performed a clustering approach based on histone markers to gain insights into the epigenetic heterogeneity within the cell lines. The delta area plots, which highlight the amount of extra cluster stability gained when increasing the number of clusters, was analyzed to determine the optimal number of clusters (Figure 39A, B). The plot revealed that using more than eight clusters did not increase the cluster stability anymore, indicating that clustering the data into eight groups best fits the dataset. Consequently, Meta8 was employed for subsequent clustering analyses.

Meta8 clustering based on histone modifications of the data generated in the first run resulted in two major clusters and six clusters with less than 5% of the cells each (Figure 39C). Signal intensities in each cluster did not reveal total shifts in populations but rather minor changes as observed in density plots. However, neither the observed changes nor the characteristics per cluster could be replicated in a second EpiTOF run. The identified clusters in the two runs differed significantly, and no common trends were observed between the runs, indicating high variability and a lack of reproducibility.

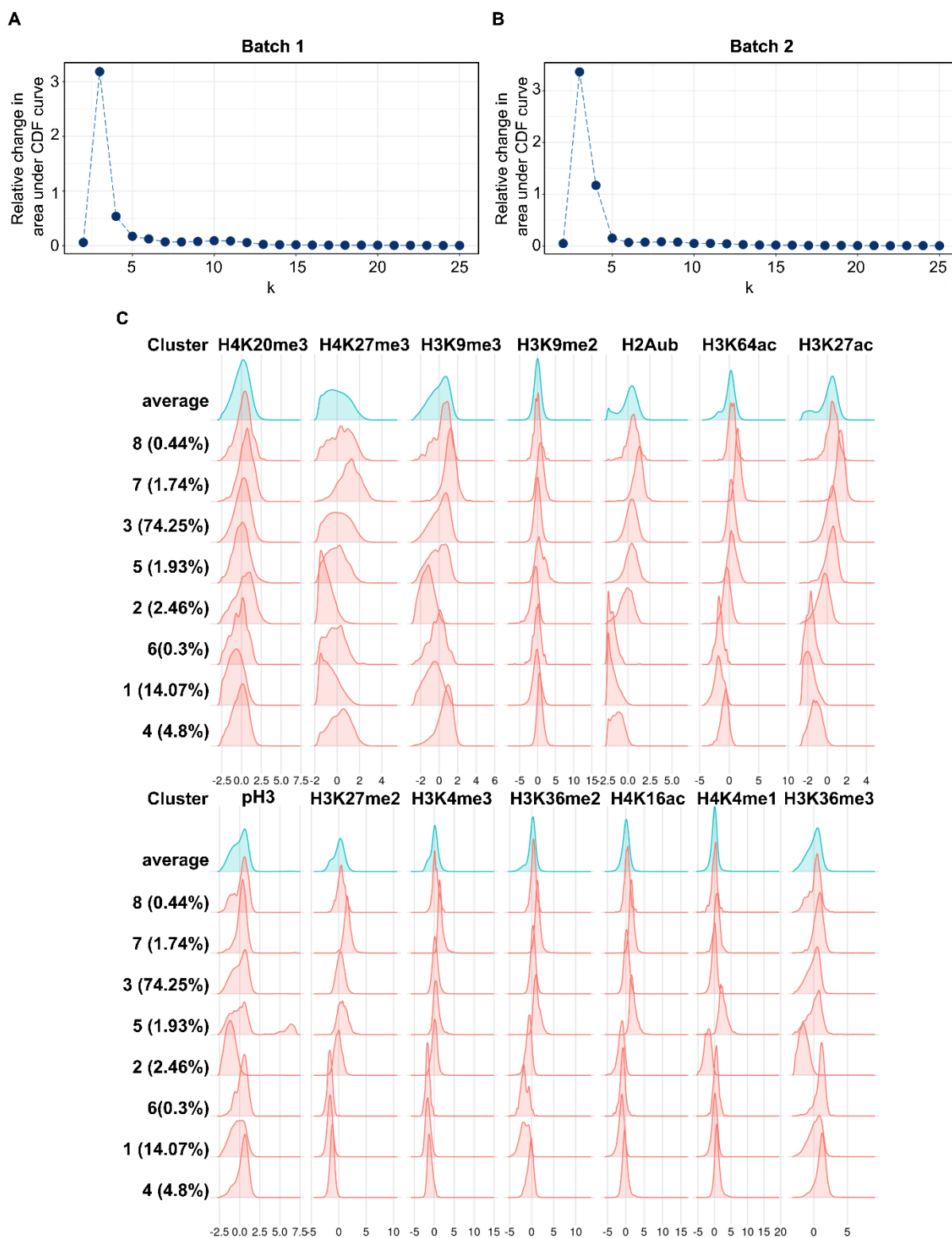


**Figure 39: Cluster-based analysis of EpiTOF data.** Delta area plots of batch 1 (A) and batch 2 (B) indicate a relative increase in cluster stability when clustering data into k groups. (C) Distribution of intensities of the stated histone modifications in each cluster of batch 1.

Red densities represent marker expression for cells in the given cluster. Numbers in brackets display the percentage of cells in that specific cluster. Blue densities are calculated over all the cells and serve as a reference. Analysis was performed by Dr. Eviatar Weizman.

Taken together, we could observe that *GLYATL1* is involved in remodeling epigenetic modifications, specifically affecting the acetylation status of H3K9, H4K14, H3K27, and H3K64 as well as H3K27 dimethylation, and H3K4 trimethylation. However, using the EpiTOF approach we were unable to identify changes in distinct epigenetic states within the different cell lines due to the lack of reproducibility.

### **4.15 Differential Pathways and Transcription Factor Activity upon *GLYATL1* Knockout**

After highlighting global changes in the epigenetic landscape upon *GLYATL1* knockout, I next investigated changes in the transcriptomes to further assess downstream effects influenced by *GLYATL1*. To this end, I conducted RNA sequencing on MCF7 LTED and the two *GLYATL1* knockout cell lines. Furthermore, transcriptional alteration upon *GLYATL1* knockdown 72 hours post-transfection in MCF7 cells was determined to identify the direct short-term effect of *GLYATL1* downregulation. Data analysis was performed in collaboration with Dr. Veronica de Melo Costa and Luisa Schwarzmüller. Principal component analysis revealed a major shift along the PC1 axis of the *GLYATL1* knockout cell lines and a shift between the two knockout cell lines on the PC2 axis. The knockdown of *GLYATL1* resulted in less pronounced changes compared to the knockout, as evidenced by a smaller shift in the PCA plot relative to the control transfected cells (Figure 40A).

The transcriptomic analysis revealed distinct differences between *GLYATL1* knockout and knockdown cells and their respective control. As already indicated in the PCA plot, smaller changes were observed in the *GLYATL1* knockdown LTED cells compared to *GLYATL1* knockout cell lines (Figure 40B). Specifically, 192 genes were downregulated with a log<sub>2</sub> fold change less or equal to -1, and 142 genes were upregulated with

a log<sub>2</sub> fold change of greater or equal to 1 in comparison to non-targeting siRNA-transfected MCF7 LTED cells. In contrast, the knockout cells exhibited major transcriptomic changes with over 360 genes consistently down- and upregulated in the two KO cell lines, indicating that the absence of *GLYATL1* triggers extensive reprogramming of gene expression. Knockdown and knockout of *GLYATL1* resulted in a consistent downregulation of 27 genes and a consistent upregulation of 15 genes. In addition to the consistently upregulated genes, each knockout cell line exhibits unique up-and-down-regulation of distinct genes, suggesting a clonal heterogeneity between the two knockout cell lines.

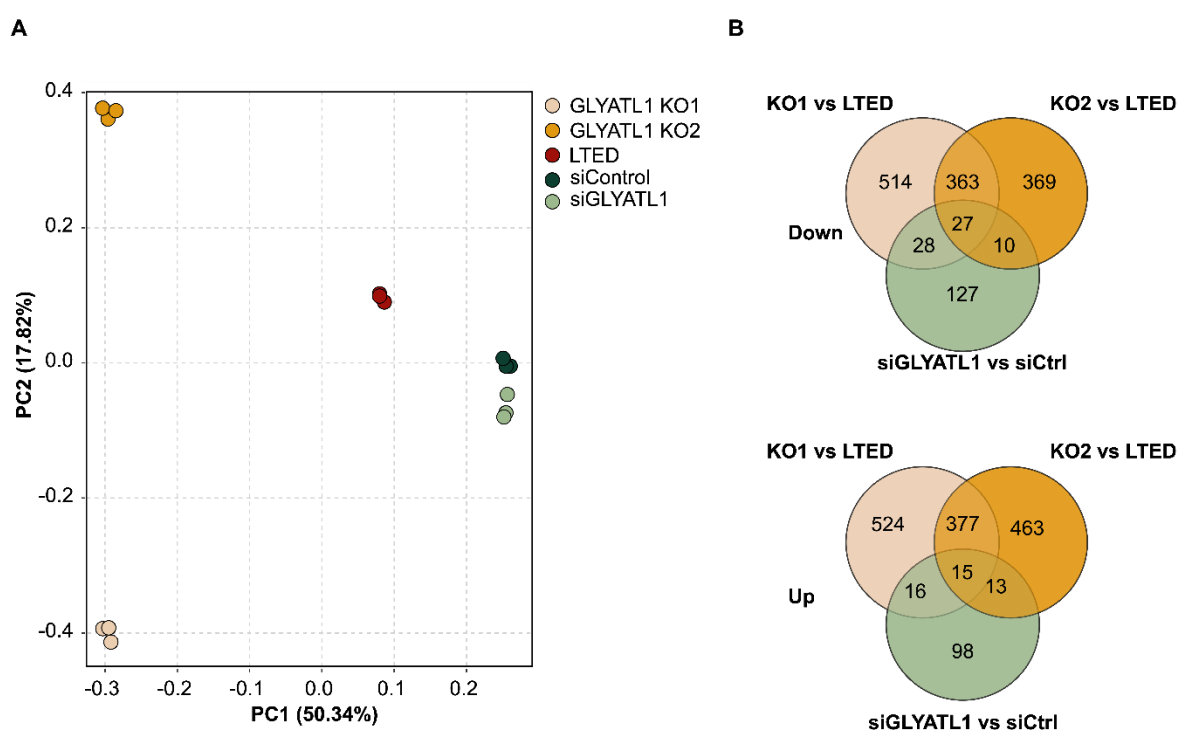


**Figure 40: Transcriptomic changes upon *GLYATL1* deregulation in MCF7. (A)** Principal component analysis (PCA) using RNA sequencing data of three biological replicates per condition ( $n=3$ ) indicated by colored dots. The first two principal components are plotted explaining 50.34% (PC1) and 17.82% (PC2) variance. Analysis was performed by Dr. Veronica de Melo Costa. **(B)** Venn diagram of down- (top) and up- (bottom) regulated genes with significant log<sub>2</sub> fold-change of indicated comparisons  $\leq -1$  or  $\geq 1$ .

Gene set enrichment analysis was conducted utilizing the hallmark gene collection from the Molecular Signature Database to evaluate the effect of *GLYATL1* disruption on specific pathways [197]. The Normalized Enrichment Score (NES) was deemed

significant with a False Discovery Rate (FDR) q-value of less or equal to 0.25 (Figure 41A and Supplementary Table 1).

The analysis revealed significant alterations across multiple cellular processes and signaling pathways. I further assessed the normalized enrichment scores of these pathways for the comparison MCF7 LTED and wildtype cells using the RNA sequencing data, generated by Dr. Emre Sofyali. Among these gene sets, five of them had an FDR q-value less than 0.25 and showed a reverse enrichment compared to *GLYATL1* knockout or knockdown (Figure 41B).

In the *GLYATL1* knockout and knockdown cells, negative enrichment scores were commonly observed for gene sets associated with cell cycle and proliferation, particularly G2M checkpoints and E2F target pathways. Further, a negative enrichment was observed for genes involved in the mitotic spindle in the *GLYATL1* knockdown cells. Collectively, these findings suggest a reduced proliferative behavior in the absence of *GLYATL1* expression, which is in line with the experimentally observed reduction in proliferation in response to both *GLYATL1* knockdown and knockout (compare Figure 18 and Figure 20).

Furthermore, a notable enrichment of cytokine-mediated pathways that influence the JAK-STAT and NF $\kappa$ B pathways was observed in response to *GLYATL1* disruption. Specifically, genes associated with the inflammatory response and the pro-inflammatory cytokine TNF $\alpha$  via NF $\kappa$ B pathways were upregulated in both the *GLYATL1* knockdown and knockout cell lines. Furthermore, especially the knockout cell lines exhibited a strong upregulation of the interferon alpha and gamma response pathways. Genes involved in interferon signaling alpha and gamma were negatively enriched in the LTED cells compared to wildtype indicating a strong inverse correlation between *GLYATL1* expression and interferon signaling mediated by JAK-STAT activation.

In line with the observed upregulation of JAK-STAT-mediated pathways, analysis of both *GLYATL1* knockout cell lines and the *GLYATL1* knockdown cells demonstrated enrichment of genes involved in the IL2-STAT5 and IL6-JAK-STAT3 signaling pathways. While the IL6-JAK-STAT3 signaling pathway did not reach significance in *GLYATL1* KO1, it did show significant positive enrichment in the knockdown condition. Collectively, these positive enrichment of immune-related pathways and partial reversion in the LTED cells compared to wildtype, suggest an involvement of *GLYATL1* in

various cytokine-induced downstream signaling such as NF $\kappa$ B and JAK-STAT signaling.

Additionally, a consistent upregulation of the stress response was observed across all conditions, as indicated by the activation of the p53 pathway, along with an enrichment of genes involved in apoptosis. This suggests an increased tendency to apoptosis and ancillary response to stress, which could be potentially triggered by the observed increased ROS levels following *GLYATL1* downregulation (compare Figure 30).

Moreover, the angiogenesis pathway was significantly upregulated across all conditions indicating that *GLYATL1* depletion might promote angiogenic signaling, which could impact tumor growth and progression.

Furthermore, early and late estrogen response pathways were significantly enriched in the *GLYATL1* KO1 cell line and partially significant in the *GLYATL1* knockdown condition. Conversely, these gene sets are negatively enriched in the LTED cells compared to wildtype cells. The positive enrichment in the *GLYATL1* knockdown and KO1 cell line is strikingly surprising since the LTED, *GLYATL1* knockdown, and knockout cells were cultured in estrogen-depleted media during the whole time. Thus, the enrichment of estrogen-responsive genes is possibly induced by an estrogen-independent activation of the estrogen receptor and the subsequent downstream signaling rather than by estrogen itself.

In addition, the epithelial-mesenchymal transition phenotype showed positive enrichment across all conditions, although not reach statistical significance in the *GLYATL1* KO2 cell line. Furthermore, the *GLYATL1* knockdown cells showed an exclusive enrichment of Notch and Hedgehog signaling pathways, with Notch signaling being significantly upregulated, while Hedgehog signaling demonstrated a significant negative enrichment score. Conversely, genes of the Hedgehog signaling pathway were positively enriched in the LTED cells compared to wildtype cells. These unique alterations suggest a specific cellular response to the short-term partial loss of *GLYATL1* expression. However, this response appears to be abolished by the long-term loss of *GLYATL1*, indicating that the knockout cell lines undergo adaptive changes over time.

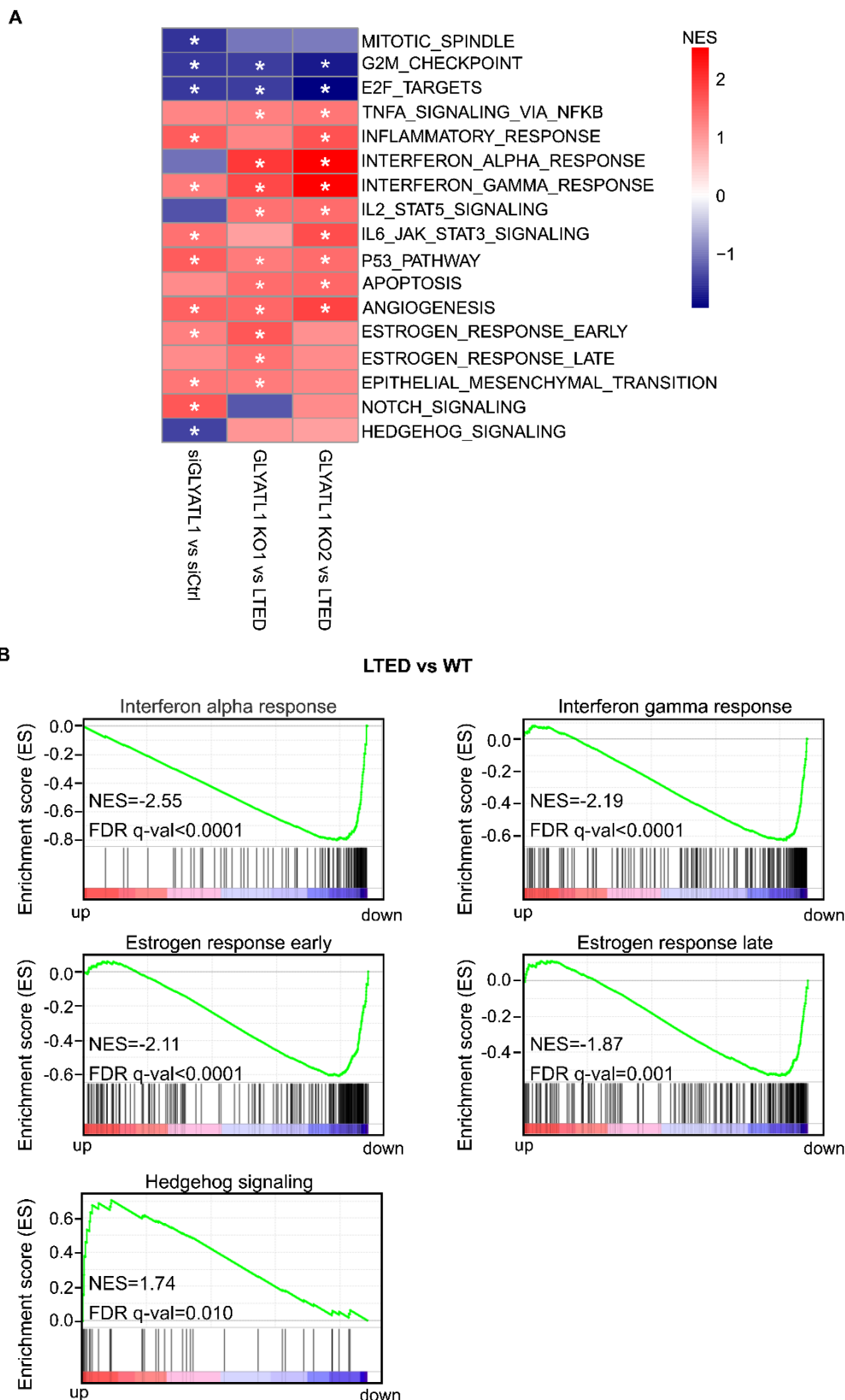


**Figure 41: Gene Set Enrichment Analysis of RNA sequencing results.** Heatmap visualization of the Gene Set Enrichment Analysis (GSEA) results using the hallmark gene collection from the Molecular Signature Database across three comparisons: siGLYATL1

vs siControl, *GLYATL1* KO1 vs LTED, and *GLYATL1* KO2 vs LTED. Color intensity represents the Normalized Enrichment Score (NES), with red indicating positive enrichment (up-regulation) and blue indicating negative enrichment (downregulation). Statistically significant results (False Discovery Rate (FDR)  $q$ -value < 0.25) are labeled by an asterisk. (B) GSEA of LTED of interferon and estrogen response in LTED compared to WT MCF7 cells.

To gain a further understanding of cellular changes, the activity of 14 major pathways was predicted using the PROGENy algorithm with the limma  $t$ -values generated with the RNA sequencing results as input [152, 198] with the help of Luisa Schwarzmüller. The algorithm does not indicate an absolute repression or activation of pathways but rather a relative ratio to the respective control. An absolute activation score of 2 is considered significant. The analysis highlights both common and distinct changes in pathway activities in LTED compared to wildtype cells and in response to *GLYATL1* perturbations (Figure 42).

The TGF $\beta$  pathway was the only pathway with a predicted significant decrease in activity in both *GLYATL1* knockout clones and the knockdown cells. Conversely, the TGF $\beta$  signaling pathway was predicted to be upregulated in LTED cells compared to wildtype cells. This reversion in pathway activity highly suggests a positive influence of *GLYATL1* on TGF $\beta$  signaling, which is abolished by *GLYATL1* downregulation.

Furthermore, a consistent upregulation of the p53 pathway was predicted for both *GLYATL1* knockout clones and the knockdown cells, which is consistent with the observed enrichment of genes involved in p53 signaling as observed in gene set enrichment analysis (compare Figure 41).

Beyond these commonalities in pathway deregulation upon *GLYATL1* disruption, unique changes in pathway activity were predicted exclusively in the *GLYATL1* knockout cells. Specifically, in these knockout cells, a consistent upregulation of the EGFR pathway and the JAK-STAT pathways was predicted, with the JAK-STAT pathway reaching the highest score in these cells. The JAK-STAT signaling pathway reached the lowest score in LTED cells compared to wildtype cells. This highly significant reversion in pathway activity suggests that high *GLYATL1* expression, as observed in the LTED cells, negatively influences the JAK-STAT signaling activity and that this inhibitory effect is attenuated in response to long-term loss of *GLYATL1* expression. This

anti-correlation of *GLYATL1* expression and JAK-STAT activation was further supported by the gene set enrichment analysis (compare Figure 41).

Furthermore, upregulation of estrogen signaling was predicted in both knockdown and *GLYATL1* KO1 cell lines, contrasting the predicted downregulation in KO2 and LTED cells. This increased activity of estrogen signaling in the *GLYATL1* KO1 and knockdown cells validates the positive enrichment of estrogen-responsive genes as observed in the GSEA (Figure 41).

Additionally, both knockout cell lines exhibited further differences. The Trail, NF $\kappa$ B, and TNF $\alpha$  pathways are commonly upregulated in the *GLYATL1* KO2 cells, which is consistent with the significant positive enrichment scores of apoptosis and TNF $\alpha$  signaling via NF $\kappa$ B as observed in the GSEA (Figure 41). Furthermore, the hypoxia pathway was predicted to be downregulated uniquely in *GLYATL1* KO1, while the knockdown cells showed significant downregulation of Wnt and androgen signaling.

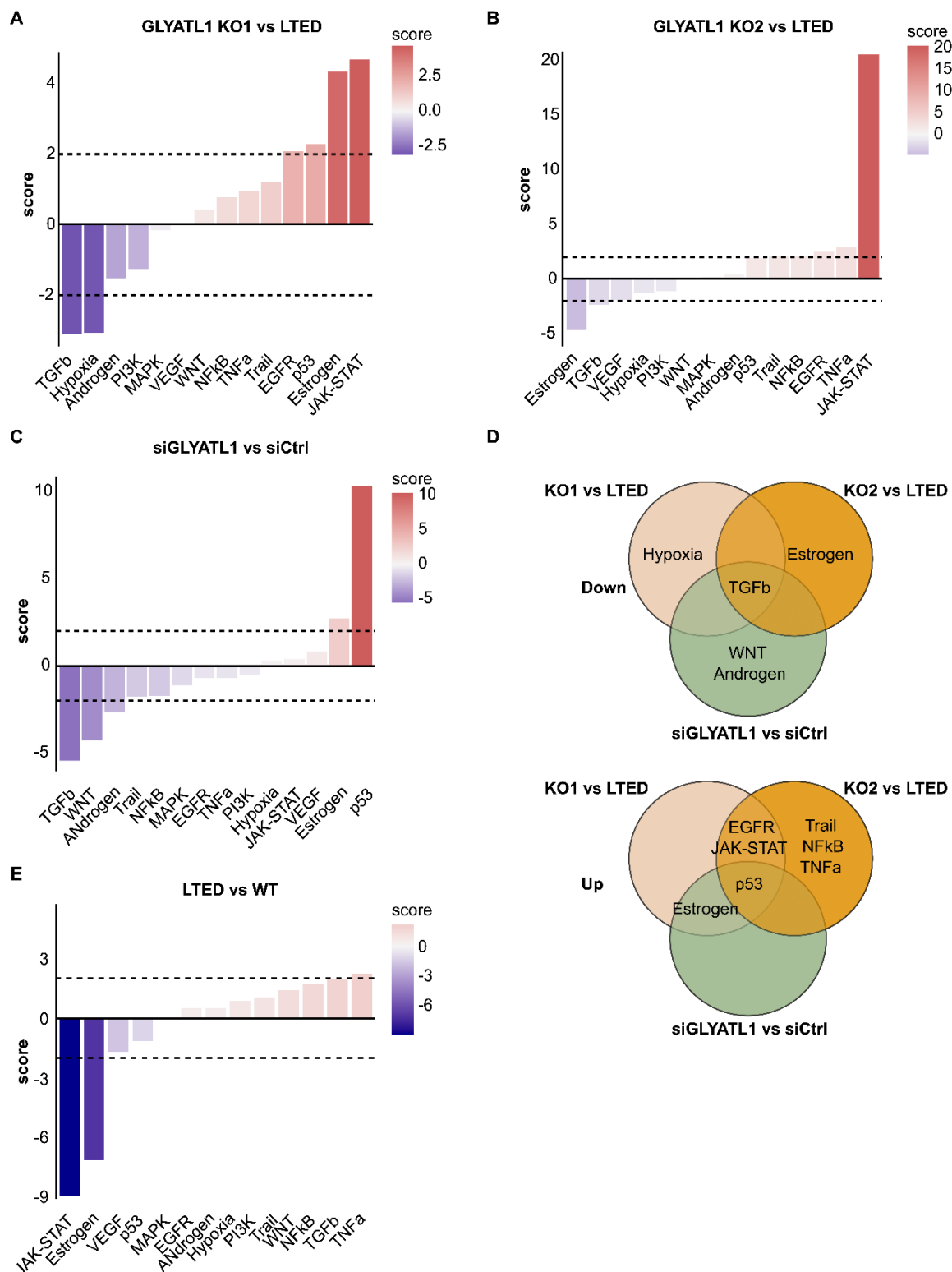


**Figure 42: Pathway activity prediction of *GLYATL1* knockdown and knockout conditions.** The activity of fourteen cellular pathways was predicted using PROGENy [152, 198] for the comparisons (A) *GLYATL1* KO1 versus LTED, (B) *GLYATL1* KO2 versus LTED and (C) knockdown of *GLYATL1* versus control knockdown based on the limma t-values calculated with the RNA sequencing results. Score  $\geq 2$  and  $\leq -2$  were considered significant

## Results

---

as indicated by the dashed lines. Higher activity is colored in red and diminished activity in blue compared to the respective control. (D) Venn diagrams displaying predicted down- and upregulated pathways across indicated comparisons. (E) PROGENy analysis of RNA sequencing data generated by Dr. Emre Sofyali comparing MCF7 LTED versus wildtype cells.

In addition, to investigate differentially activated pathways, I next used DoRothEA to predict differential transcription factor activities based on the RNA sequencing results [153-155], with the help of Luisa Schwarzmüller. Transcription factors with a score higher than 2 or lower than -2 are deemed significant and revealed notable common and pivotal changes in *GLYATL1* knockdown and knockout cell lines (Figure 43).

Common downregulation of activity was found in eight transcription factors. In particular, the activity of transcription factors of the E2F family regulating gene expression of genes particularly related to cell cycle control, namely E2F1, E2F2, E2F3, and E2F4, were downregulated upon *GLYATL1* knockdown and knockout. In addition, the activities of the transcription factors, CEBPG, SMAD5, NFIC, and GLI2 involved in various cellular processes such as cell survival, cell differentiation, and angiogenesis, are further predicted to be commonly downregulated.

Besides the common downregulation of these transcription factor activities, both knockout cell lines additionally showed predicted downregulated activity of transcription factors involved in differentiation, cell proliferation, epigenetic control, cell cycle, and apoptosis, namely SMAD1, TCF3, HES1, DNMT1, ID1, ID2, ID3, SOX2, SOX17, TBX2, and TFDP1. Furthermore, transcription factor activity in *GLYATL1* knockdown condition shared down-regulation of activity privately with *GLYATL1* KO1 (FOXA2, SREBF1, SREBF2, RORA) and with *GLYATL1* KO2 (PAX8, TFAP2A, NR4A2, DLX5). Moreover, 41 transcription factors showed unique downregulation in activity upon *GLYATL1* knockdown. Among these transcription factors, seven transcription factors showed a reverse effect in either one *GLYATL1* knockout cell line, KO1 (BHLHE41, CTNNB1, ARX) or KO2 (SP1, NFKB, KLF6), or in both (CDX2).

In contrast, KLF4 was predicted to be consistently more active in both knockout and knockdown conditions. KLF4 is involved in various cellular processes such as cell cycle, immune response, and repression of epithelial-to-mesenchymal transition [199]. Furthermore, both knockout cell lines showed higher predicted activity of transcription

factors involved in differentiation (CDX1, CDX2, TP73), immune regulation (CIITA, STAT1, STAT2), stress response (HIF1A, EPAS1, TP73, ATF3), and apoptosis (TP73, ATF3). Moreover, transcription factor activity in *GLYATL1* knockdown condition shared up-regulation of activity privately with *GLYATL1* KO1 (TP63, ERG, GLI3, NOTCH1) and with *GLYATL1* KO2 (ATF4, NFE2L2, FOXP3). Knockdown of *GLYATL1* resulted in unique upregulation of activity in seven transcription factors (HDAC1, BRCA1, KLF5, MSX2, NANOG, FOXA1, NR2C2), in which FOXA1 showed a reverted effect in *GLYATL1* KO1 and MSX2 in KO2. Furthermore, ESR1 showed unique upregulation in activity in *GLYATL1* knockout clone 1.

I further assessed the transcription factor activity for the LTED cells compared to wildtype. Out of 39 significantly altered transcription factor activities, only two transcription factors, namely STAT2 (score of -10.3) and IRF1 (score of -4.5), showed a significant reversal in activity between LTED versus wildtype cells and *GLYATL1* knockout versus LTED.

Combining the results of the Gene Set Enrichment analysis, pathway activity predictions using the PROGENy algorithm and transcription factor activity prediction from DoRothEA revealed a recurring trend across various pathways:

I could find a consistent correlation of *GLYATL1* expression with proliferation-related processes, as evidenced by negative enrichment scores for gene sets related to G2M checkpoints and E2F targets in response to *GLYATL1* disruption. This is complemented by lower predicted E2F transcription factor activity and a shared decrease in TGF $\beta$ -pathway activity.

Furthermore, the downregulation of *GLYATL1* resulted in the upregulation of immune and stress response pathways, indicated by the overrepresentation of genes involved in p53, interferon, and interleukin signaling pathways. This is further supported by increased activation of STAT transcription factor and increased JAK-STAT pathway activity. Activity and/or enrichment of these pathways are partially reverted in the LTED compared to wildtype cells suggesting an involvement of *GLYATL1* in suppressing these pathways.

The GSEA and pathway prediction results indicate increased activity in estrogen-related pathways in the *GLYATL1* knockout clone 1. Moreover, transcription factor activity prediction shows that the key mediator of estrogen signaling, ESR1, is more active

## Results

in the knockout clone 1 indicating that despite growing in estrogen-depleted media, *GLYATL1* knockout clone 1 still shows elevated estrogen signaling potentially through estrogen-independent ER activation.

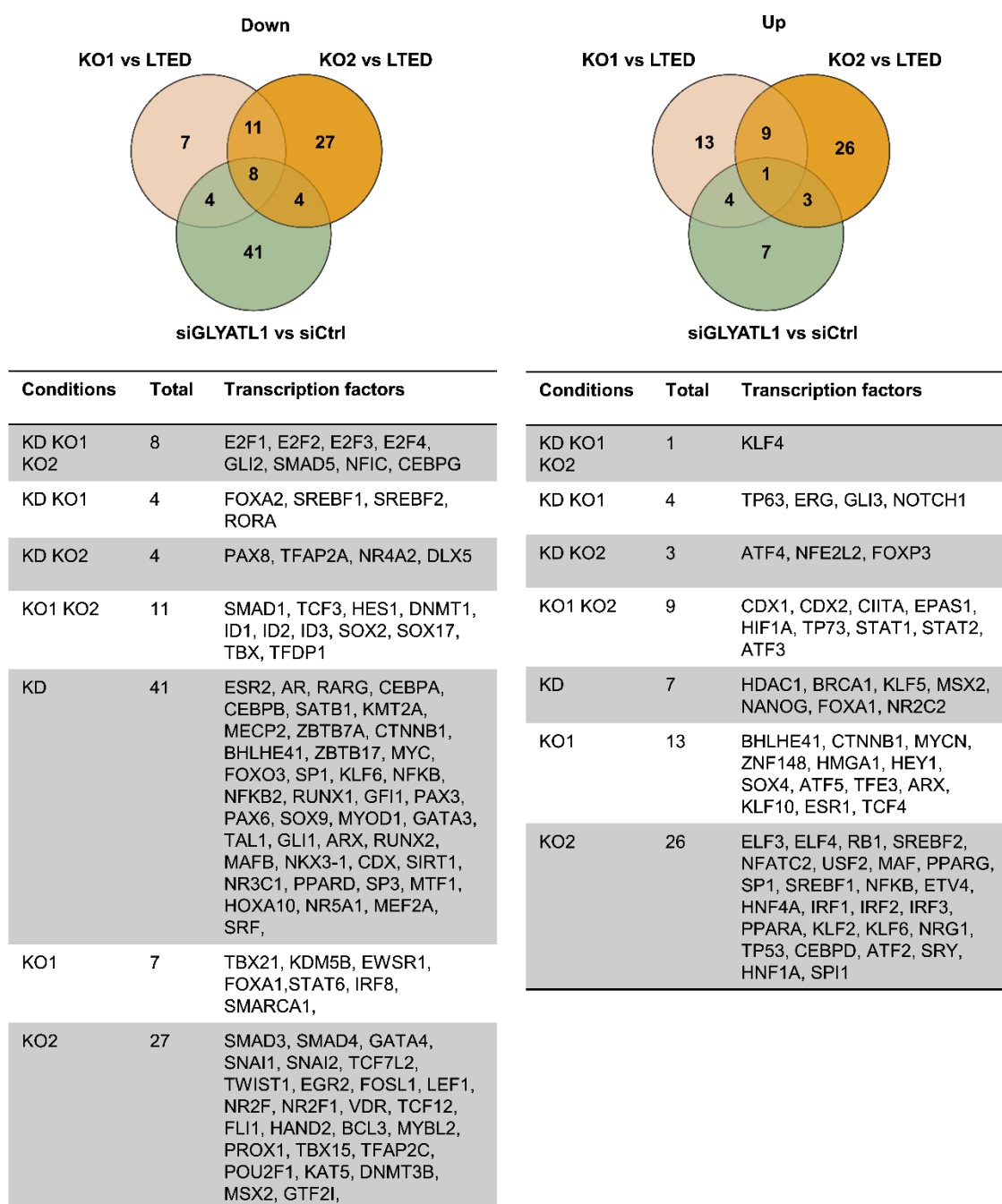


**Figure 43: Transcription factor activity prediction.** The activity of transcription factors was predicted using DoRoThEA [153-155] for the comparisons of *GLYATL1* KO1 versus LTED (KO1), *GLYATL1* KO2 versus LTED (KO2), and knockdown of *GLYATL1* versus control knockdown (KD) based on the limma t values calculated with the RNA sequencing results. Venn diagrams and tables show transcription factors with significant (activity score

$\leq -2$ ,  $\geq 2$ ) down- (left) and up- (right) regulated activity. Tables show deregulated transcription factors in detail.

#### 4.16 Deregulated Histone Modulator upon *GLYATL1* Knockout

Since analysis of the epigenetic landscape indicated an influence of *GLYATL1* on modifications of several histone residues, I next utilized the RNA sequencing data to analyze the expression of various histone modifiers. The acetylation status of lysine residues is modulated by histone acetyltransferases (HAT/KAT), which transfer acetyl groups to lysine residues, and by histone deacetylases and sirtuins (HDAC and SIRT), which remove the acetylation group. To better understand the influence of *GLYATL1*, I included the data generated by Dr. Emre Sofyali comparing the results of LTED and wildtype cells (Figure 44A).

Several histone modifiers showed significant deregulation in response to *GLYATL1* disruption, with some histone showing the opposite trends in LTED cells compared to wildtype cells. Specifically, *KAT2B* was significantly upregulated in the LTED cells but significantly downregulated in both *GLYATL1* knockout cells with *GLYATL1* knockdown cells showing the same trend. As observed with the inhibitor Gracinol, the proliferation of the LTED cells is highly dependent on proper *KAT2B* activity (Figure 34A). Thus, the downregulation of *KAT2B* potentially contributed to the observed reduced proliferation in the *GLYATL1* knockout and knockdown cell lines. Since *KAT2B* is known to acetylate histone H3K9 and H3K14 acetylation, downregulation of *KAT2B* could consequently contribute to the reduced acetylation of H3K9 and H3K14 as observed by Dr. Emre Sofyali in response to *GLYATL1* knockdown (Figure 36).

Furthermore, *HDAC2* and *HDAC3* expression is significantly downregulated in the LTED cells compared to wildtype and reversibly upregulated in response to *GLYATL1* disruption. Given the mentioned expression levels and the ability of HDACs to deacetylate histone residues, *HDAC2* and *HDAC3* potentially influence the acetylation status of H3K27 and H3K64, which were found to be the highest in the LTED cells and diminished in the wildtype and *GLYATL1* knockout cell lines (Figure 37). While the knowledge of histone modifiers acting on H3K64 is limited, H3K27 is known to be primarily acetylated by CREBBP/EP300 [200]. *CREBBP* and *EP300* showed a trend to

be higher expressed in the LTED cells and lower in response to *GLYATL1* disruption and the wildtype cell. This expression pattern correlates with the experimentally validated H3K27 acetylation status as observed in the EpiTOF experiment (Figure 37).

Beyond histone acetylation, lysine and arginine residues can be methylated, influencing gene expression by either activating or repressing it. Histone methyltransferases catalyze the transfer of a methylation group, while histone demethylases reverse methylation. Diverse histone enzymes affecting the methylation status are significantly deregulated in the LTED cells and in response to *GLYATL1* knockout and knockdown (Figure 44B).

Compared to wildtype cells, the expression pattern of only ten histone modifiers is significantly altered in the LTED cells, including *SETD5-7*, *KDM1B*, *SUV39H2*, *KDM3A*, *KDM4B*, *KDM4D*, *KDM7A*, and *PRMT9*, with some of these showing reverse expressing pattern in response to *GLYATL1* disruption. In contrast, *GLYATL1* knockdown and knockout led to significant deregulation of multiple additional histone modifiers acting on various H3 and H4 residues. These alterations suggest broader changes in histone methylation beyond those analyzed in this study.

The EpiTOF results revealed significantly higher H3K4 trimethylation and H3K27 dimethylation in the LTED cells, which are reduced in the wildtype and *GLYATL1* knockout cells (Figure 37). In line with this observation, the expression of *KDM5B* and *C*, which demethylates H3K4 is upregulated in the *GLYATL1* knockout cells and partially in the *GLYATL1* knockdown cells, which could contribute to demethylating H3K4 in these cells.

While *GLYATL1* knockout cell lines show mostly similar expression patterns, *GLYATL1* knockdown showed a partially reversed expression pattern for example in *KDM5B*, *SUB39H1*, *NSD1*, *NSD2*, and *KDM6B*, which could hint to a possible long-term adaptation mechanism in response to the loss of *GLYATL1* expression.



## Results

in the PC2 axis, separates the LTED samples from both *GLYATL1* knockouts, however did not further separate the wildtype cells from the knockout cell lines. Additionally, the third principal component (PC3) demonstrated separation between the two *GLYATL1* knockout lines, explaining 13.9% of the variance and highlighting specific differences and unique characteristics between the both knockout cell lines (Figure 45A).

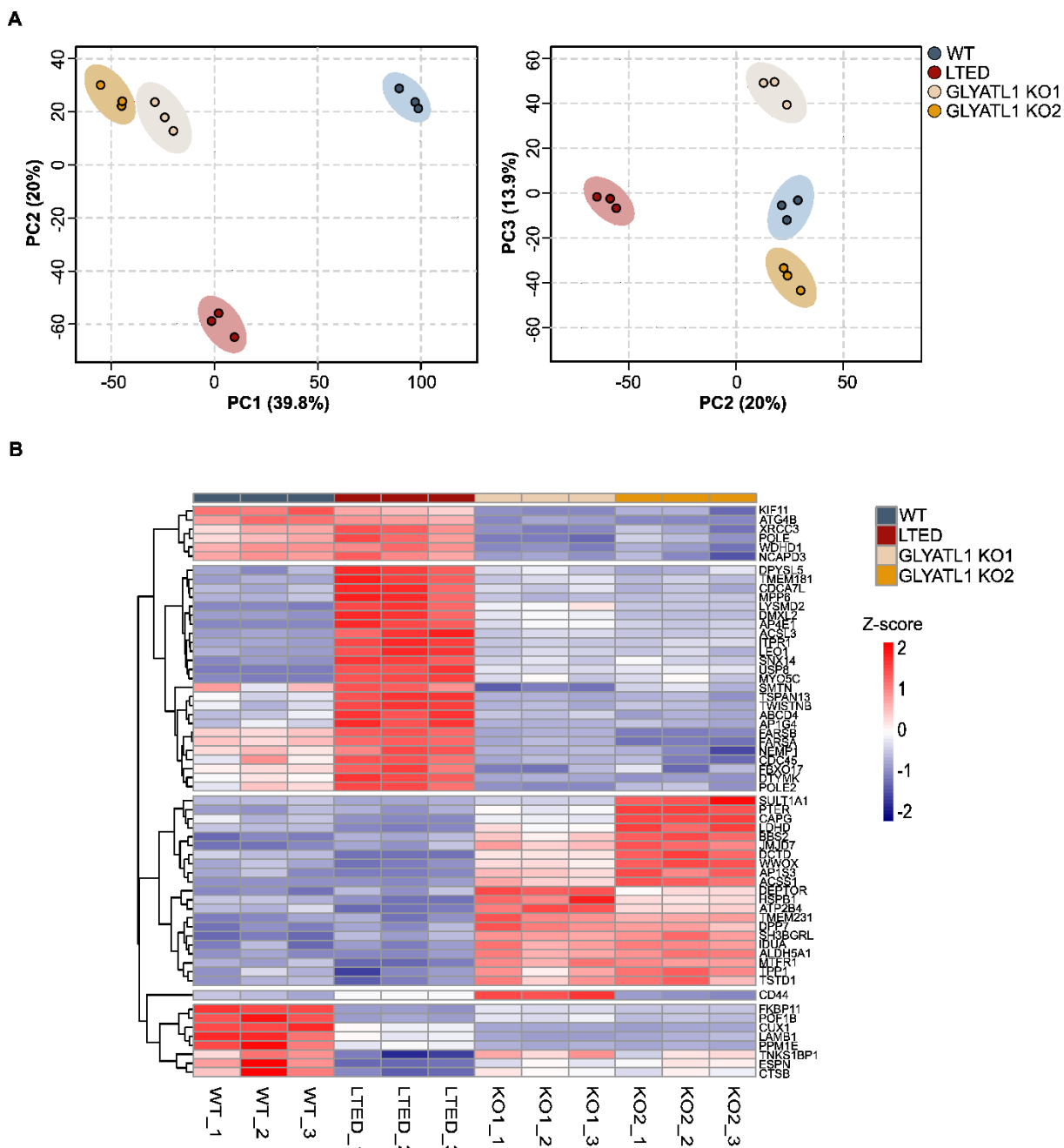


**Figure 45: Analysis of full proteome.** (A) Principal component analysis (PCA) using full proteome data. The first three principal components are plotted explaining 39.8% (PC1), 20.0% (PC2) and 13.9% (PC3) variance. (B) Hierarchically clustered heatmap showing z-

scaled intensities of proteins with significant ( $p$ -value  $\leq 0.05$ , determined by Student's unpaired t-tests using Perseus software) changes in both *GLYATL1* knockout cell line with an absolute log<sub>2</sub> fold-change of at least 1 in any sample. Biological replicates ( $n=3$ ) are displayed separately. Data was analyzed by Luisa Schwarzmüller.

To investigate common changes in response to *GLYATL1* knockout, I analyzed proteins with significant changes in both *GLYATL1* knockout cell lines with an absolute log<sub>2</sub> fold-change of at least 1 revealed several protein patterns (Figure 45B). Proteins in the first and third clusters showed no alteration upon resistance acquisition but displayed significant changes upon *GLYATL1* knockout.

Furthermore, 25 proteins exhibited a significant increase in expression upon resistance and showed reverse patterns upon *GLYATL1* knockout (Cluster 2). Among these proteins, the RNA polymerase-associated protein LEO1 was found to be highly expressed in LTED cells and low expressed in both *GLYATL1* knockout cell lines. Furthermore, Acyl-CoA Synthetase Long-Chain Family Member 3, ACSL3, was found to exhibit elevated expression in LTED and reduced expression in wildtype and *GLYATL1* knockout cell lines.

To identify over- and underrepresented pathways upon resistance (LTED vs WT) and after *GLYATL1* knockout, I performed Gene Set Enrichment Analysis (GSEA) on the full proteome data using the hallmark gene collection from the Molecular Signature Database. The analysis revealed several significant pathway alterations across the different comparisons (Table 11).

In the comparison of LTED and WT, unique changes were observed affecting cholesterol homeostasis with a positive normalized enrichment score of 1.87. Furthermore, myogenesis, interferon alpha, and interferon gamma response demonstrated an underrepresentation of genes in the LTED. Conversely, a significant overrepresentation of the genes involved in the interferon alpha response was observed in the *GLYATL1* KO2 cell line, which was already observed in GSEA analysis using transcriptomic data (Figure 41).

Gene sets related to cell cycle control and proliferation, particularly those involved in the mitotic spindle and G2M checkpoint, were collectively underrepresented following *GLYATL1* knockout supporting similar observations from the GSEA analysis using the

RNA sequencing data. Consistent with this, the E2F targets gene set was significantly downregulated in the *GLYATL1* KO2 cell line. Furthermore, this reduction in proliferative behavior was observed experimentally (compare Figure 20).

While both *GLYATL1* knockout cell lines shared this common trend in proliferation-affecting pathways, the estrogen signaling pathway displayed inconsistent behavior between them. Late and early estrogen signaling was consistently underrepresented in both LTED and *GLYATL1* KO2 cell lines, but these gene sets were significantly overrepresented in the *GLYATL1* KO1 cell line.

Taken together, the proteome data strongly support the enrichment of gene sets related to several cellular key pathways including cell cycle regulation, immune response, estrogen signaling, cellular stress, and DNA damage response, as already observed with transcriptomic data. This consistency highly strengthens the reliability of the observed biological processes that were found to be affected by *GLYATL1* in endocrine therapy-resistant cell lines.

**Table 11: Gene set enrichment analysis of full proteome data** using the hallmark gene collection from the Molecular Signature Database. Analysis was performed with significantly ( $p_{adj} \leq 0.05$ ) expressed proteins across the indicated comparisons. Values indicate the Normalized Enrichment Score (NES) and the False Discovery Rate (FDR) q-value with statistically significant results (FDR q-value < 0.25) with bold text.

Hallmark gene set	<i>GLYATL1</i> KO1 vs LTED		<i>GLYATL1</i> KO2 vs LTED		LTED vs WT	
	NES	FDR q-val	NES	FDR q-val	NES	FDR q-val
MITOTIC_SPINDLE	-1.88	<b>0.012</b>	-2.21	<b>0.001</b>	1.56	0.313
G2M_CHECKPOINT	-2.66	<b>0.000</b>	-2.82	<b>0.000</b>	-0.54	0.966
E2F_TARGETS	-	-	-2.74	<b>0.000</b>	-	-
INTERFERON_ALPHA_ RESPONSE	-	-	2.11	<b>0.004</b>	-2.45	<b>0.001</b>
INTERFERON_GAMMA_ RESPONSE	-	-	-	-	-1.85	<b>0.024</b>
P53_PATHWAY	-	-	0.56	0.943	-2.01	<b>0.010</b>
UV_RESPONSE_UP	-	-	-1.29	<b>0.230</b>	0.69	0.843
ESTROGEN_ RESPONSE_EARLY	2.30	<b>0.001</b>	-1.19	0.296	-2.81	<b>0.000</b>
ESTROGEN_RESPONSE_LATE	1.53	<b>0.092</b>	-1.72	<b>0.041</b>	-2.43	<b>0.000</b>
CHOLESTEROL_ HOMEOSTASIS	-	-	-	-	1.87	<b>0.078</b>
MYOGENESIS	-	-	-	-	-1.37	<b>0.243</b>

## 5 Discussion

Endocrine therapy is the keystone treatment for estrogen-positive breast cancer and significantly improves patient outcomes. However, 40-50% of the patients with late-stage disease do not respond to that treatment approach or develop resistance towards these antiestrogen drugs [75]. Therefore, studying the molecular mechanisms behind resistance is crucial for understanding and developing new therapeutic options that can overcome treatment resistance and improve long-term survival rates for breast cancer patients.

Recent studies in-house by Dr. Emre Sofyali revealed *GLYATL1* as a highly upregulated gene in endocrine therapy-resistant MCF7 and T47D breast cancer cell lines [131]. While there is an emerging number of studies, where deregulated *GLYATL1* levels were found in several cancer entities [135-138], the function of this protein remains elusive. In the scope of this thesis, I used phenotypic, metabolic, epigenetic, transcriptomic, and proteomic analysis to investigate the function of *GLYATL1* in the context of endocrine therapy resistance in luminal A breast cancer cell lines.

### 5.1 *GLYATL1* Expression Anticorrelates with Estrogen Supply

Endocrine therapy-resistant in-vitro breast cancer cell lines provide robust models for studying alterations in cellular processes in response to antiestrogen treatment. In this study, I utilized MCF7 and T47D cell lines that were deprived of estrogen to simulate aromatase inhibitor treatment. In these long-term estrogen-deprived cells, *GLYATL1* mRNA and protein levels are significantly elevated suggesting a potential role in therapy-resistant mechanisms (Figure 10).

Reintroducing estrogen to the growth media for a short period (48h) to simulate drug withdrawal, resulted in a rapid decrease in *GLYATL1* expression (Figure 13). The suppressive effect of estrogen on *GLYATL1* expression was further enhanced by time, as after a four-week interval of estrogen addition the expression remained at a minimal level (Figure 12).

Conversely, subsequent estrogen depletion in 12-week pre-treated LTED cells inverted the effect and *GLYATL1* expression increased rapidly, surpassing even higher

levels of mRNA compared to untreated LTED cells. These findings suggest that the LTED cells are capable of rapidly adjusting to fluctuations in estrogen availability and point to a potential negative influence of estrogen on regulating *GLYATL1* expression. This adjustment of *GLYATL1* expression underlines the importance of *GLYATL1* exclusively in the context of aromatase inhibition.

## 5.2 Regulatory Interplay between ER and FOXA1 Regulates *GLYATL1* Expression under Estrogen-Deprived Conditions

Despite the role of estrogen in the regulating of *GLYATL1* expression, I further observed the involvement of ER itself and FOXA1 in *GLYATL1* gene expression regulation, as the knockdown of these transcription factors negatively influences *GLYATL1* expression (Figure 15, Figure 16). Since the promoter region of *GLYATL1* harbors binding sites for both transcription factors (Figure 14), this regulation might be guided directly.

Considering that the LTED cells were cultivated in estrogen-depleted media, the ER-mediated *GLYATL1* transcription seems to be independent of estrogen. The *ESR1* mRNA levels are increased in the LTED compared to wildtype, particularly in MCF7. This upregulation of *ESR1* has been commonly observed in LTED cells and is associated with estrogen-independent ER-mediated growth [126, 127].

In the group of Prof. Dr. Magnani, from which we kindly got the MCF7 cell lines, they performed CHIP sequencing studies to analyze ER-bound chromatin with peak-calling techniques. In the LTED cells, they identified several peaks in the regulatory elements of genes indicating an activated estrogen-independent ER signaling. While no peaks were detected in the *GLYATL1* promoter of wildtype cells, a distinct peak in LTED cells was identified that corresponded with the peaks in the *GLYATL1* promoter region found in the ATAC sequencing results by Dr. Emre Sofyali [131]. This suggest that ER could bind directly to the promoter region of *GLYATL1* solely in the LTED cells and induce *GLYATL1* expression in an estrogen-independent manner.

Furthermore, they demonstrated that cholesterol biosynthesis is highly upregulated in the MCF7 LTED cells compared to the parental wildtype cells. This constitutive activation can lead to the accumulation of cholesterol derivative, including 27-hydroxycholesterol, which can induce ER chromatin binding and downstream gene expression [201]. Preliminary analysis of proteomic and transcriptomic data by Luisa Schwarzmüller and me confirmed the significant upregulation of cholesterol biosynthesis in the used MCF7 LTED cells compared to wildtype cells (Data not shown). Further inhibition of central players in cholesterol synthesis, such as 3-hydroxy-3-methyl-glutaryl-coenzyme A reductase by statins [202], and subsequent expression analysis could verify the influence of cholesterol biosynthesis on *GLYATL1* expression in the used cellular context.

Since the estrogen response signaling is significantly downregulated in the LTED cells compared to wildtype cells (compare Figure 41B, Figure 42E, Table 11) and the *GLYATL1* expression is significantly downregulated in response to estrogen supply (compare 5.1), these observations could suggest that the ER transcription factor activity is limited to a specific subset of genes and could indicate the involvement of additional regulatory mechanisms.

One regulatory mechanism could comprise the ER “pioneer” factor FOXA1. In contrast to the upregulation of *ESR1*, *FOXA1* mRNA levels remained unchanged in the LTED cells suggesting that FOXA1 might be recruited to the *GLYATL1* promoter region through additional regulatory mechanisms. The binding of FOXA1 to chromatin is enhanced by DNA hypomethylation within the promoter region [203], methylation of histone residue H3K9 [204], and posttranslational modification of FOXA1 by O-GlcNAcylation [205]. Indeed, recent studies in the group by Dr. Emre Sofyali identified augmented hypomethylated CpGs in the promoter region of *GLYATL1* in the LTED cells compared to wildtype cells [131]. These changes in the DNA methylation status could consequently lead to alternative FOXA1 recruitment to the promoter locus, which subsequently facilitated ER-binding by remodeling chromatin structure and induced the expression of specific genes [206, 207] including *GLYATL1* in the LTED cells.

### **5.3 Downregulation of *GLYATL1* but not Overexpression Influences Cell Proliferation**

Upregulation of *GLYATL1* exclusively in LTED under estrogen-deprived conditions indicates a distinct role in resistance towards aromatase inhibition. In this study, I could show that the knockdown of *GLYATL1* significantly diminished the proliferative capacity of LTED cells in both MCF7 and T47D cells under estrogen-depleted conditions (Figure 18). Moreover, *GLYATL1* knockout further exacerbated the negative effects on cell proliferation (Figure 20), indicating that residual *GLYATL1* levels in the knockdown might partially compensate for the cellular function related to proliferation.

In contrast to the observed influence of *GLYATL1* knockdown and knockout, stable overexpression of *GLYATL1* in MCF7 and T47D wildtype did not enhance cell proliferation under estrogen-depleted conditions with proliferation rates comparable to those of the empty vector control (Figure 22). Thus, *GLYATL1* is required for proliferation in LTED cells; however, overexpression of *GLYATL1* is not sufficient to confer resistance within nine days under antiestrogen conditions.

During resistance development in the used T47D cells, RNA sequencing revealed that *GLYATL1* mRNA levels were only modestly elevated during the initial two months but showed a significant increase at later stages of resistance acquisition [131]. This temporal expression pattern together with the missing effect of *GLYATL1* overexpressing on proliferation could indicate that *GLYATL1* plays a resistant-supportive rather than a driving role, potentially acting on maintaining the established resistance phenotype.

### **5.4 *GLYATL1* Contributed to Succinic Acid Accumulation, however, does not Influence Glutamine Dependency**

The gene *GLYATL1* encodes the Glutamine N-acyltransferase-like protein 1, which catalyzes the transfer of an acyl group to the  $\alpha$ -amino group of glutamine. This enzymatic capability could consequently influence cellular metabolism as observed in previous studies, where *GLYATL1* was found to influence metabolic pathways, such as glycolysis and gluconeogenesis in prostate cancer cell lines [138, 139].

Glutamine is the most abundant amino acid with concentrations in the human plasma ranging from ~500 to 800  $\mu\text{M}$  and even higher concentrations in some tissues such as the liver and skeletal muscle [208, 209]. In this study, the cells were cultured in commercially available DMEM media with standard 2 mM glutamine, which highly exceeds the physiological glutamine levels. However, I could show that under low glutamine concentrations, the proliferation rates of MCF7 and T47D are not significantly altered compared to the growth in standard cell culture media during eight days (Figure 26).

Furthermore, it is commonly observed that in cell culture media the glutamine levels are lower than prescribed due to the decay of glutamine to ammonia and pyrrolidine carboxylic acid [210]. As a result, the actual glutamine concentrations in the media may have been lower than initially assumed, aligning more closely with physiological levels. Based on the usage of glutamine as an educt, *GLYATL1* upregulation in the LTED cells could correlate with increased glutamine dependency. Indeed, I could observe a dependency of the LTED on glutamine, as the proliferation rate significantly dropped with glutamine depletion (Figure 26, 0mM). However, the *GLYATL1* knockout cells exhibited the same diminished proliferation behavior with no significant difference compared to LTED indicating that the observed glutamine dependency might be independent of *GLYATL1*. Instead, it appears that adaptation to long-term estrogen deprivation induces alterations affecting the requirement of glutamine supply that is maintained after *GLYATL1* knockout.

In the literature, increased glutamine demand and dependency was commonly associated with drug resistance including resistance towards antiestrogen treatment in breast cancer [211]. In resistant breast cancer cells, increased glutamine dependency could be correlated with increased MYC signaling regulating enzymes involved in glutamine uptake and catabolism. Consequently, the increase in glutamine catabolism could lead to metabolic reprogramming to induce dependency on glutamine to promote tumor growth and survival [212, 213].

Further metabolic analysis revealed that both *GLYATL1* knockout cell lines, particularly clone 1, exhibited a metabolic profile highly similar to LTED, while the wildtype cells showed a pronounced deregulation of several metabolites (Figure 29). A diminished abundance of all tricarboxylic acid cycle intermediates except succinic acid could be

commonly observed in the LTED cells. The accumulation of succinic acid was significantly reverted in the *GLYATL1* knockout cell lines. In line with this observation, mRNA levels of the succinate dehydrogenase subunits, especially *SDHB*, are significantly diminished in the LTED cells and conversely elevated in the *GLYATL1* knockout cell lines. The mRNA levels of *SDHC* and partially *SDHD* showed similar trends, however, not reaching significant levels. Downregulation of these subunits in the LTED cells could lead to decreased oxidation of succinate, the dianionic form of succinic acid, to fumarate and consequently to the observed accumulation of succinate. In line with this, the fumarate levels are significantly lower in the LTED cells and significantly restored in the *GLYATL1* knockout cell lines. Given that the levels of succinate are tightly correlated with the expression of *GLYATL1*, it might be possible that *GLYATL1* directly or indirectly influences the succinate metabolism in the LTED cells.

Besides the role in metabolism, recent studies revealed a novel role of SDH and succinate in biological processes including tumorigenesis. Altered functions of the SDH complex such as mutations in the SDH subunits, diminished expression, or post-translational modifications, which result in decreased activity and consequently in accumulation of succinate were found in several cancer entities. Thus, *SDH* was recently characterized as a tumor suppressor gene, while succinate was defined as oncometabolite [214]. In cancer cells, accumulation of succinate can cause inhibition of several  $\alpha$ -ketoglutarate ( $\alpha$ KG)-dependent dioxygenases, which influence diverse biological processes including epigenetic modification. Chromatin structure is influenced by several enzymes including  $\alpha$ KG-dependent dioxygenases such as the ten-eleven-translocation (TET) enzymes and several histone demethylases [215]. Thus, accumulation of succinate can induce histone hypermethylation and lead to a decrease of hydroxylation of 5mC consequently resulting in DNA hypermethylation [216-218]. Congruent with the accumulation of succinate, I could observe an alteration in histone methylation, which will be discussed in section 5.6. in detail.

Furthermore, succinate accumulation can activate the TGF $\beta$  signaling pathway ultimately promoting cell migration and invasion, which was reverted by *SDHB* overexpression [219]. I could observe a similar effect on the TGF $\beta$  pathway by knocking out *GLYATL1*, which will be discussed in section 5.9.

Taken together, the tight correlation of *GLYATL1* expression and the accumulation of succinate suggests that GLYATL1 could influence succinate metabolism by for example promoting the synthesis of succinate or inhibiting the subsequent processing to fumarate. Specifically, GLYATL1 could affect anaplerotic reaction to replenish TCA cycle intermediates that subsequently will be catalyzed to succinate. Furthermore, it might be possible that educts of the GLYATL1-catalyzed reaction directly or through alteration of SDH cofactor availability could inhibit the function of SDH. Consequently, succinate accumulation in the LTED cells can promote several biological changes, which ultimately promote tumor growth and disease progression. However, further research is necessary to elucidate the influence of GLYATL1 on succinate.

To analyze potential acyl-donors for the GLYATL1 catalyzed reaction, I analyzed the abundance of several acyl-CoA species in the different MCF7 cell lines. However, none of the measured acyl-CoAs were accumulated in both *GLYATL1* knockout cell lines (Figure 27). This pattern suggests that GLYATL1 might utilize other substrates, which were not analyzed in this experimental setup. Previous study revealed that purified GLYATL1 could bind phenyl-acyl-CoA with high affinity [134] pointing that aryl-group containing CoA species might serve as a substrate for GLYATL1.

The proteomic analysis provided further clues of potential GLYATL1 substrates. The expression of Acyl-CoA Synthetase Long-Chain Family Member 3 (ACSL3) was shown to be elevated in LTED cells and reduced in wildtype and *GLYATL1* knockout cells. ACSL3 catalyzes the synthesis of fatty acyl-CoA esters from long-chain fatty acids [220]. Thus, the upregulation of ACSL3 in LTED cells could be an indicator of potential fatty acyl-CoAs as GLYATL1 substrates, which were not examined in the conducted metabolome study.

Overall, these findings suggest that GLYATL1 influences the abundance of succinate, which consequently might induce biological processes contributing to tumor growth and disease progression. Future studies, including mutational analysis of the catalytic center in GLYATL1, further exploration of potential acyl-donors, and tracing of glutamine within the cell could clarify the role of GLYATL1 on succinate synthesis and its interaction with broader metabolic networks in endocrine therapy-resistant cells.

## 5.5 Mitochondrial GLYATL1 Modulates Oxidative Stress Levels

Despite the role of mitochondrial proteins in metabolic pathways, several mitochondrial proteins are well known for their dual role in generating ROS as byproducts of respiration and managing oxidative stress through antioxidant defense mechanisms. In *Drosophila melanogaster*, the glycine N-acyltransferase (GLYAT) was found to modulate the JNK-mediated ROS activation [221], thereby highlighting the influence of acyltransferases on redox balance.

Flow cytometry analysis using the CellROX probe revealed diminished basal oxidative stress levels in the LTED cells compared to wildtype and *GLYATL1* knockout cell lines, particularly in *GLYATL1* KO2 cells (Figure 30). Further experiments using the roGFP2-Orp1 sensor, which specifically measures H<sub>2</sub>O<sub>2</sub> ROS species, revealed that *GLYATL1* knockout did not significantly affect H<sub>2</sub>O<sub>2</sub> levels in the cytoplasm or mitochondria. This suggests that GLYATL1 plays a crucial role in maintaining low levels of ROS under estrogen-deprived conditions. However, this effect is exclusive to ROS species other than H<sub>2</sub>O<sub>2</sub>, such as superoxide or hydroxyl radicals.

Given GLYATL1's ability to transfer an acyl group to glutamine (Figure 9), GLYATL1 may contribute to antioxidant synthesis, possibly through the production of N-acyl amino acids. In literature some N-acyl amino acids, for instance, N-acetyl-cysteine, are known for their antioxidative properties, mimicking natural ROS scavengers and effectively reducing basal stress levels [222, 223]. Thus, the GLYATL1-catalyzed reaction could contribute to increasing the antioxidative capacity and consequently diminish the intracellular ROS levels. However, this hypothesis requires experimental confirmation.

Elevated ROS production or impaired antioxidative defense can trigger oxidative stress and damage to proteins, lipids, nucleic acids, membranes, and organelles. This damage can impair the proper cellular function and initiate death processes such as apoptosis, ferroptosis, or autophagy [224-227]. Consequently, elevated antioxidant synthesis can enable the tumor to evade cell death and survive under therapeutic stress conditions. Similarly, significantly lower ROS levels and an increased antioxidative capacity were found in tamoxifen-resistant cell lines compared to wildtype [228], supporting the hypothesis that endocrine-resistant tumors potentially evolve mechanisms to maintain low ROS levels with a pivotal role of GLYATL1. This antioxidative capacity potentially modulates the activation of downstream effector pathways.

## 5.6 *GLYATL1* Contributed to Epigenetic Reprogramming

One possible influence of altered oxidative stress levels is on the activity of histone modifiers and downstream histone modifications. Epigenetic-focused cytometry by Time-of-Flight (EpiTOF) revealed significant alterations in H3K27 acetylation and demethylation, H3K4 trimethylation, and H3K64 acetylation (Figure 37). These histone residues showed enhanced modification levels in the MCF7 LTED cells compared to wildtype cells and decreased levels in response to *GLYATL1* knockout. Thus, *GLYATL1* not only influences the previously analyzed H3K9 and K14 acetylation status [131] but also causes the remodeling of more histone residues in endocrine therapy-resistant breast cancer cell lines.

H3K27 acetylation was found associated with enhancer and promoter regions triggering activation of target gene expression. Remodeling of H3K27 acetylation status was previously observed in the context of endocrine therapy resistance, as tamoxifen and fulvestrant-resistant cells both demonstrated gained acetylation, which resulted in gained chromatin interaction with high enrichment in active enhancer marks [229]. Furthermore, inhibition of EP300/CREBBP, which primarily catalyzes H3K27 acetylation, significantly suppressed breast cancer growth in vitro and in vivo [230, 231], strengthening the importance of H3K27 acetylation in tumor growth and progression. Thus, the *GLYATL1*-influenced H3K27 acetylation in the LTED cells could promote the resistance phenotype and contribute to accelerated tumor growth.

While *EP300* expression was not significantly altered in response to *GLYATL1* disruption, *CREBBP* was found to be significantly downregulated in response to *GLYATL1* knockdown and borderline not significant in *GLYATL1* knockout cell lines compared to LTED cells (Figure 44). Although altered expression does not imply altered activation, the expression pattern could hint at possible drivers acting on the histone residues. Furthermore, the expression of HDAC2 and HDAC3, which were found to deacetylate H3K27 histone residue [232, 233], were upregulated in *GLYATL1* knockout cell lines compared to LTED cells. Elevated ROS levels, as observed in the knockout cell lines, have been shown to contribute to HDAC activity including activation of HDAC3 [234]. Thus, *GLYATL1* could influence H3K27 acetylation by diminishing oxidative stress levels and consequently decreasing the activity of HDACs. Conversely, the downregulation and missing activation of *HDAC2* and *HDAC3* accompanied by the upregulation

of *CREBBP* in the LTED cells could shift the balance of H3K27 residue to a more acetylated status.

My results also indicate that H3K27 dimethylation follows the same trend as H3K27ac. Since the same H3K27 residue could only be either acetylated or methylated, this result indicates, that the changes were potentially not globally homogenous but rather locally distinct. In contrast to acetylation of this residue, dimethylation is a marker of gene repression, which could promote breast tumorigenesis by negatively regulating tumor suppressor gene expression [235]. However, downstream analyses are necessary, to identify the affected genes by H3K27 acetylation and demethylation in LTED cells.

H3K27me2 is mainly demethylated by KDM6 [236, 237]. In the cell, the activity of KDM6 is regulated by various factors including succinate, which has been shown to inhibit the activity of KDM6 [238]. As described in section 5.4, succinate is accumulated solely in the LTED cells, and this accumulation was reverted in the *GLYATL1* knockout cells. Therefore, elevated levels of succinate potentially inhibited the function of KDM6, thereby maintaining H3K27 dimethylation in the LTED cells. Conversely, *GLYATL1* knockout led to diminished succinic acid abundance within the cells, which could effectively reverse the inhibitory effect and enable KDM6 to demethylate H3K27 as observed in the EpiTOF experiment.

Furthermore, the EpiTOF experiment revealed significant changes in H3K4 trimethylation, a marker related to active transcription. High trimethylation of this residue, as observed in the LTED cells, significantly correlated with shorter survival rates, shorter progression-free survival, and oncogenic progression in breast cancer [239, 240]. Recent studies in melanoma cells revealed that H3K4 trimethylation contributed to drug resistance by upregulation of the proliferative capacity in slow-cycling drug-tolerant persister cells [241]. In line with this study, downregulation of H3K4me3 enhanced response to fulvestrant and reduced tumor growth and invasiveness in breast cancer cell lines by regulating cancer stemness [242]. Thus, the partial re-sensitizing to antiestrogens in response to *GLYATL1* knockout could partially be induced by H3K4 demethylation.

In prostate cancer, the H3K4 trimethylation was found to be influenced by the TGF $\beta$  pathway [243]. Similar mechanistic influence could be possible in the resistant cells, as TGF $\beta$  signaling was predicted to be more active in the LTED cells (Figure 42).

Histone H3K4 is primarily methylated by complexes of histone methyltransferase 2 (KMT2) family proteins. The activity of these complexes was shown to be triggered by H2B ubiquitination [244]. Although the ubiquitination levels of H2B were not determined in this study, proteome data potentially hint at alterations in the ubiquitination status of H2B. In the proteome data, LEO1 expression was found to be elevated in the LTED and downregulated in both *GLYATL1* knockout cell lines. LEO1, also known as RNA Polymerase-associated protein LEO1 homolog, is a component of the RNA Polymerase II-associated factor (PAF) complex involved in promoting histone modifications such as H2B ubiquitination [245-247]. Thus, the upregulation of LEO1 in the LTED cells might indicate increased ubiquitination of H2B, which further could stimulate H3K4 trimethylation in the resistant MCF7 cell line.

Moreover, the KDM5 family of demethylases plays a crucial role in modifying the methylation status of histone H3 at lysine 4 [248]. The mRNA levels of *KDM5B* and *KDM5C* were increased in the *GLYATL1* knockout cell lines (Figure 44), which could consequently lead to diminished H3K4me3 levels as observed in the EpiTOF experiment. Similar to KDM6, the activity of KDM5 proteins is inhibited by elevated succinate levels in the cell [215, 249]. Thus, *GLYATL1*-influenced succinate accumulation could lead to the inhibition of KDM5 abolishing H3K4 demethylation, which results in the observed increase of H3K4me3 levels in the LTED cells.

The final histone residue that showed significant changes in response to *GLYATL1* knockout in both EpiTOF runs was H3K64. Acetylation of H3K64 is associated with open chromatin and active transcription, particularly enriched at enhancer regions where it colocalizes with H3K27ac [250]. In MCF7 cells, both H3K64 and H3K27 acetylation levels followed a similar pattern, with lower levels observed in both wildtype and *GLYATL1* knockout cells. Furthermore, Spearman correlation analysis revealed a strong positive link between H3K27ac and H3K64ac in MCF7 cell lines (Figure 38). This suggests that H3K64 acetylation might enhance and amplify the resistance-promoting effects of H3K27ac target genes.

Further exploration of the downstream effects of these histone markers through ChIP-Sequencing could provide deeper insights into their potential roles in resistance mechanisms. Furthermore, RNA sequencing uncovered further deregulated histone modifiers, which are not known to directly influence the four histone modifications previously discussed (Figure 44). While this study did not assess the activity of these histone modifiers, their deregulation could imply a broader level of epigenetic reprogramming that was not fully detected in this study. As already indicated, these histone residues are potentially not globally reprogrammed, but rather local. Thus, the expected changes could be rather small and masked by limitations in for example antibody quality or reproducibility between the runs, making them difficult to analyze.

To address distinct clusters with specific epigenetic characteristics, we performed an unsupervised clustering approach based on the histone modifications. However, the batches significantly varied between the two EpiTOF runs, and no common trend could be observed. Although the EpiTOF method allows high-dimensional and detailed data generation on a single-cell level, it is highly sensitive to variability between runs. To improve reproducibility normalization beads and anchor samples can help to estimate batch effects and achieve reliable data sets [251, 252].

Moreover, the cytometry by time-of-flight technology is mostly used to characterize heterogeneous samples, such as immune cell subsets or the cellular diversity in complex cell populations. In this scenario, high diversity between the different cell populations which are characterized by distinct marker expressions is expected. However, the diversity of cell populations within one cell line, as I used, is substantially smaller. This reduced diversity within a cell line compared to across different cell types likely makes it more challenging to define distinct clusters using unsupervised methods.

## **5.7 *GLYATL1* Expression Negatively Influence p53 Pathway Activation**

To evaluate the downstream effects of *GLYATL1*-influenced accumulation of succinate, diminished ROS levels, and the identified histone modifications, I performed RNA sequencing and full proteome analysis with subsequent pathway and gene set enrich-

ment analysis and pathway analysis. The principal component analysis using the proteome data revealed a significant distinction between wildtype cells and the LTED cells, as well as the two *GLYATL1* knockout cell lines, primarily along the PC1 axis, which accounts for nearly 40% of the total variance (Figure 45A). Additionally, the PC2 axis further differentiated the LTED cells from the *GLYATL1* knockout lines; however, it did not provide additional separation between the knockout lines and the wildtype cells. Since the *GLYATL1* knockout cell lines were derived from the LTED cells, this could explain their closer proximity and the major separation to the wildtype cells. Moreover, knockout of *GLYATL1* reverted, to some extent, the status of the gene expression network back to the wildtype state as indicated by the absence of a significant shift on the PC2 axis. This reversion could indicate that *GLYATL1* seems to have major impact on this network. Furthermore, the reversion of protein expression could be observed in the downstream pathway analysis for example the p53 pathway.

In the LTED cells, p53 pathway-associated genes were negatively enriched compared to wildtype cells. Conversely, genes of this gene set showed a positive enrichment in the comparison of *GLYATL1* KO2 versus LTED cells (Table 11). This significant positive enrichment could be further validated and expanded to both *GLYATL1* knockout cell lines and in response to *GLYATL1* knockdown using the transcriptomic data (Figure 41). Furthermore, analysis of this data set predicted p53 as the only shared upregulated pathway in response to *GLYATL1* knockdown and knockout (Figure 42) and a predicted upregulation of TP53 transcription factor activity in *GLYATL1* KO2 cells (Figure 43). Collectively, high *GLYATL1* expression, as observed in the LTED cells, negatively influenced p53 pathway activation. This negative influence is abolished upon *GLYATL1* knockdown and persisted even after long-term adaptation to *GLYATL1* knockout.

The tumor suppressor protein p53, commonly referred to as the “guardian of the genome”, is a crucial regulatory protein and plays a major role in maintaining genome stability and preventing cancer development [253]. In response to cellular stress, p53 transcriptionally activates genes involved in various biological responses including DNA damage response [254], cell cycle inhibition [255], senescence [256], and apoptosis [257, 258].

Given that *GLYATL1* is localized in the mitochondria, its effect on p53 activation is likely indirect, potentially involving a signaling cascade or second messengers. P53 can be activated by several stimuli, including DNA damage, and stress-activated kinases. Elevated oxidative stress levels can induce DNA damage and mediate phosphorylation of p53 ultimately leading to activation of p53 [259, 260]. Therefore, *GLYATL1* disruption could induce p53 pathway activity by increased oxidative stress levels due to potential low antioxidative capacity. The activation of this tumor suppressor pathway may contribute to abolishing cancer development and re-sensitization to antiestrogen treatment by activating cellular checkpoints and damage response mechanisms.

MDM2, a negative regulator of p53, promotes p53 degradation and inhibits its tumor-suppressive function [261, 262]. Inhibiting MDM2 has emerged as a promising therapeutic strategy in cancer treatment, especially for overcoming challenges associated with directly targeting nuclear p53 [263]. MDM2 inhibition in combinational therapy with fulvestrant successfully induced cell cycle arrest through inhibition of E2F targets and G2M checkpoint signaling, and significantly reduced tumor growth accompanied by reduced Ki-67 levels in resistant patient-derived xenografts models [264]. Similar effects on cell cycle and proliferation were observed in *GLYATL1* knockout and knock-down cell line models.

## **5.8 *GLYATL1* Contributed to Proliferation in Endocrine Therapy-Resistant Cells**

Negative enrichment scores were consistently observed for genes of the G2M checkpoints and E2F target gene sets in both knockout cell lines and following *GLYATL1* knockdown using the RNA sequencing data (Figure 41) and partially validated using proteome data (Table 11). Specifically, the E2F transcription factors (E2F1-4), which are pivotal for driving the cell cycle from G1 to S phase [265-267], showed reduced activity in response to *GLYATL1* disruption (Figure 43). High E2F activity has been linked to poor response to AI treatment and resistance, as E2F transcriptional activity can drive cell cycle progression and proliferation in an estrogen-independent manner [268, 269]. This estrogen-independent E2F activation allows cancer cells to bypass the

growth-inhibitory effects of endocrine therapies. Therefore, *GLYATL1* downregulation may reduce the proliferative capacity of LTED cells by decreasing the activity of E2F transcription factors and G2M checkpoint genes, potentially through p53 pathway activation, which could indicate a proliferation-supportive role of *GLYATL1*.

Moreover, EpiTOF analysis revealed Ki-76 highest levels in wildtype cells and decreased levels in LTED cells, with a further decrease upon *GLYATL1* knockout (Figure 37). As a marker of cell proliferation [270, 271], high Ki-67 levels in wildtype cells indicate higher proliferative properties compared to LTED cells. The reduction of Ki-67 levels upon *GLYATL1* knockout is consistent with the experimental observation of reduced proliferative behavior in the *GLYATL1* knockdown (Figure 18) as well as the *GLYATL1* knockout cells (Figure 20).

### **5.9 GLYATL1 Modulates Activity of TGF $\beta$ Pathway and Associated Effectors**

Pathway analysis following the disruption of *GLYATL1* using PROGENy identified additional altered pathway activities. This analysis predicted a significant upregulation of the TGF $\beta$  signaling pathway in the LTED compared to wildtype cells. Conversely, a consistent downregulation of TGF $\beta$  was the only pathway observed in both knockout clones and knockdown cells (Figure 42). This anti-correlation of *GLYATL1* expression and TGF $\beta$  activation suggests an inhibitory effect of *GLYATL1* on the TGF $\beta$  activity.

TGF $\beta$  is known for its dual role in cancer, acting as a tumor suppressor in the early stage and a promoter of tumor progression and drug resistance in the advanced stage [272, 273]. In advanced and resistant cancer cells, TGF $\beta$  signaling promotes epithelial-mesenchymal transition, angiogenesis, and immune suppression, thereby facilitating invasion, metastasis, and tumor growth [274, 275]. The observed downregulation of TGF $\beta$  activity upon *GLYATL1* knockdown and knockout suggests a reduction in these tumor-promoting effects, which could potentially enhance antiestrogen treatment efficacy.

TGF $\beta$  signaling is initiated by dimerization of TGF $\beta$  receptors, leading to the phosphorylation of downstream receptor-regulated SMAD proteins (SMAD1, 2, 3, 5, 8). These

phosphorylated SMADs then form a complex with SMAD4 and translocate into the nucleus, where the complex regulates the expression of target genes in a cofactor-dependent manner [276].

In this study, transcription factor activity predictions indicated significant downregulated activities of several SMAD transcription factors following *GLYATL1* disruption (Figure 43). Specifically, the activity of SMAD5 was downregulated in both *GLYATL1* knockdown and knockout cells, while SMAD1 activity was downregulated only in knockout cell lines, and SMAD3/4 activity was uniquely downregulated in the *GLYATL1* KO2 cell line.

This altered SMAD activity pattern could suggest a pronounced impact on bone morphogenetic protein (BMP) signaling, particularly through SMAD1/5/8, which are key mediators of BMP-responsive gene expression. Consistent with this, I observed significant downregulation of *BMP7* and *BMP4* following *GLYATL1* disruption, although *BMP4* downregulation was not statistically significant in knockdown cells (Data not shown). This downregulation of this pathway is further supported by the decreased activation of the transcription factors Inhibitors of Differentiation 1-4 (ID1-4) in both *GLYATL1* knockout cell lines (Figure 43), whose expression is regulated by *BMP4* and *BMP7* signaling [277].

Despite a potential activation of the BMP signaling, transcription factor activity prediction indicated a significant downregulation of *GLI2* activity in response to both *GLYATL1* knockdown and knockout. *GLI2*, which is activated downstream of SMAD3, regulates the expression of genes including *GLI1*, which are involved in various responses including migration and cell growth [278-280]. The activation of this cellular pathway is further supported by the predicted downregulation of *GLI1* transcription factor activity observed in *GLYATL1* knockdown cells (Figure 43).

These findings imply that *GLYATL1* upregulation in MCF7 LTED cells could modulate the cellular response to endocrine therapy by upregulating the tumor-promoting TGF $\beta$  pathway and affecting key downstream effectors such as BMPs and *GLI2*.

However, the precise mechanism of how *GLYATL1* influences TGF $\beta$  pathway activity remains unclear. A possible mechanism for how increased *GLYATL1* levels could mediate TGF $\beta$  activation is through the accumulation of succinate as observed in the LTED cells (compare section 5.4). In colorectal cancer, the knockdown of *SDHB* and

the consequent accumulation of succinate led to hyperactivation of the TGF $\beta$  signaling pathway [219]. Thus, a similar mechanism could happen in the LTED cells, where GLYATL1 elevates the succinate levels and consequently activates the TGF $\beta$  signaling.

### **5.10 *GLYATL1* Expression Anticorrelates with JAK-STAT Signaling**

In addition to the discussed deregulated pathways, cytokine-mediated pathways that trigger JAK-STAT activation were commonly overrepresented in the *GLYATL1* knockout cell lines and showed a reverse enrichment in the LTED compared to wildtype levels (Figure 41A and Table 11). Consistently, the PROGENy algorithm revealed a strong activation of the JAK-STAT signaling pathway in both *GLYATL1* knockout cell lines and the reverse pattern in LTED compared to wildtype cells (Figure 42). Additionally, STAT1 and STAT2 transcription factors were predicted to be more active in the knockout cell lines (Figure 43) underlining the negative influence of *GLYATL1* expression on JAK-STAT signaling. In contrast, the STAT2 transcription factor activity is significantly reduced in the LTED cells compared to wildtype (see 4.15) supporting the inhibitory effect of *GLYATL1* expression on JAK-STAT signaling.

The JAK-STAT signaling pathway is activated in response to ligand binding to membrane receptor tyrosine kinases. The noncovalently bound cytosolic Janus kinases (JAKs) get activated and phosphorylate tyrosine residues of the cytosolic domain of the receptor. This phosphorylation residue provides a docking site for the signal transducers and activators of transcription (STATs), which are subsequently phosphorylated by JAK. Consequently, STATs can dimerize in homo- or heterodimers and translocate into the nucleus to mediate transcription of target genes [281, 282].

Beyond activation of antiviral response, JAK-STAT signaling is known for its antitumor effects. Activated STATs, especially STAT1 and STAT2, control tumor growth by suppressing transcription of major cell cycle components, such as cyclins or c-Myc [283], or promoting transcription of the CDK inhibitor p21 [284, 285]. Additionally, the anti-tumor response mediated by JAK-STAT signaling can promote cell death by inducing the formation of protein caspase 1 and 11 [286] and inhibiting the expression of anti-apoptotic *Bcl-2* and *Bcl-x* genes [287]. Therefore, the diminished JAK-STAT signaling

in the LTED cells could contribute to tumor progression by promoting cell cycle progression and inhibiting apoptosis. Conversely, *GLYATL1* knockdown and knockout could abolish this effect, which is consistent with the observed reduction in proliferation (Figure 18, Figure 20) and the enrichment of genes involved in apoptosis (Figure 41).

However, the role of JAK-STAT signaling in cancer is complex and highly dependent on the cellular context. Enhanced JAK-STAT was shown to contribute to AI-resistant phenotype by direct interaction and activation of the estrogen receptor by STAT1 [288]. This contradictory finding highlights the need for further studies to validate the cellular response to JAK-STAT deregulation in the LTED and *GLYATL1* knockout cell lines. Targeting different players of the JAK-STAT pathway, such as JAK1/2 by the specific inhibitor Ruxolitinib [289], could help to understand the effect on cell cycle progression, apoptosis, and tumorigenesis in this specific cellular context. Additionally, the mechanism of how *GLYATL1* influences the activation of STATs remained elusive. Since members of the STAT family, such as STAT1, were shown to be activated in response to increased ROS levels [290], a similar activation mechanism could be possible as a *GLYATL1*-dependent decrease in ROS levels was observed in LTED cells.

### 5.11 Clonal Heterogeneity in *GLYATL1* Knockout Cell Lines

While both *GLYATL1* knockout cell lines exhibited disruptions in the discussed pathways, principal component analysis of transcriptomic and proteomic data revealed significant differences between two *GLYATL1* knockout cell lines. In the PCA analysis utilizing transcriptomic data, the knockout cell lines exhibited a shift along the PC2 axis, which accounted for 17.82% of the total variance (Figure 40A). Since wildtype samples were included in the proteomic data, a clear separation of the two knockout cell lines was observed along the PC3 axis explaining 13.9% of the variance (Figure 45A). These shifts indicate distinct alterations between the two knockout cell lines, which led to significant changes in downstream analyses of transcription factor and pathway activation, including the activation of the estrogen-signaling pathway.

Specifically, the *GLYATL1* KO2 cell line shows downregulated estrogen signaling, as indicated by PROGENy pathway predictions (Figure 42) and GSEA using proteome data (Table 11). In contrast, the *GLYATL1* KO1 cell line demonstrates an upregulation

of estrogen signaling. This increase in estrogen signaling is further supported by GSEA analysis using transcriptomic data (Figure 41) and increased *ESR1* transcription factor activity, as predicted by the DoRothEA algorithm (Figure 43). Additionally, the estrogen receptor exhibited the highest levels in *GLYATL1* knockout clone 1 in the EpiTOF experiment (Figure 37), whereas clone 2 showed similar low levels as LTED cells.

As already discussed, the estrogen receptor could be activated by metabolites of the cholesterol biosynthesis and STAT1 (compare 5.2 and 5.10). Compared to the LTED cells, cholesterol biosynthesis was not further upregulated in the *GLYATL1* KO1 cell lines (Data not shown). Furthermore, the STAT1 expression levels and activity levels are similar in both knockout cell lines. Thus, the upregulation of estrogen receptor signaling is potentially a result of other cellular adaptations, which are exclusive in the *GLYATL1* KO1 cell line, highlighting a clonal heterogeneity between the two knockout cell lines. This heterogeneity is further evidenced in the metabolome data, where *GLYATL1* KO2 shows significant metabolic alterations compared to LTED, while these changes could not be observed in *GLYATL1* KO1 (Figure 29).

Based on Sanger sequencing both clones share the same 20 bp homozygous deletion in exon 4 (Figure 19), raising the question of whether the two clones originated from the same progenitor cell and diverged over time, or if the clones originated from different progenitor cells. In the case of different progenitor cells, possible off-target effects of the sgRNA have to be taken into account.

The discrepancy in behavior between the two knockout cell lines raises the possibility that the observed unique differences might not be attributable to *GLYATL1* knockout but could also involve compensatory mechanisms unique to each clone. Further studies involving additional *GLYATL1* knockout cell lines are necessary to determine whether the unique patterns observed in these clones are directly related to the function of *GLYATL1* or resulted from other adaptive processes. Furthermore, whole genome sequencing could indicate possible mutations that drive unique downstream patterns.

## 5.12 Adaptive Cellular Responses to Partial versus Complete *GLYATL1* Loss

In addition to the observed discrepancy between the two *GLYATL1* knockout cell lines, the comparison of partial versus complete loss of *GLYATL1* expression reveals significant transcriptomic changes and differences in activated pathways and transcription factors. While *GLYATL1* knockout induces major transcriptomic changes as indicated by the shift at the PC1 axis explaining over 50% of the variance in the PCA plot, the knockdown samples (si*GLYATL1*) and the transfection control (siControl) are only slightly separated as indicated by a minor shift along the PC2 axis (Figure 40A). Specifically, the transcriptomic analysis identified the deregulation of approximately 200 genes unique to *GLYATL1* knockdown conditions. In contrast, more extensive changes were observed in both *GLYATL1* knockout cell lines, with over 700 consistently deregulated genes with a relative fold change of at least 1. Only 42 genes (27 downregulated and 15 upregulated) were commonly affected by partial and complete loss of *GLYATL1* expression, indicating a limited overlap in the gene expression profiles between these two models (Figure 40).

Consequently, this expression pattern also influences transcription factors and pathway activities. For instance, the WNT signaling pathway was predicted to be downregulated (Figure 42) in line with less active transcription factors like  $\beta$ -catenin, SOX9, MYC, and FOXO3 in knockdown cells (Figure 43), potentially leading to reduced cell proliferation and differentiation. However, this pathway activity was not significantly altered in the LTED cells or in response to *GLYATL1* knockout. Furthermore, GSEA analysis highlighted the upregulation of Notch signaling and downregulation of Hedgehog signaling in *GLYATL1* knockdown conditions (Figure 41). The inverse correlation of these enrichments suggests an interplay between these pathways, where Notch signaling negatively influences Hedgehog signaling. This interaction has been previously documented, indicating that Notch signaling can suppress the expression of Hedgehog components [291].

Furthermore, among the unique deregulated transcription factors in response to *GLYATL1* knockdown, nine transcription factors exhibited a reverse activation pattern

in either one *GLYATL1* knockout cell line or in both, suggesting that *GLYATL1* knockout induces an adaptive response that partially alters the initial effects seen with knock-down.

Taken together, these transcriptomic changes suggest that short-term reduction of *GLYATL1* via RNAi induces a distinct and potentially transient cellular response that is partially retained, or even reversed in *GLYATL1* knockout conditions over time. This could indicate an adaptive mechanism in response to complete *GLYATL1* knockout over time, allowing the cells to compensate for the loss of *GLYATL1* expression. The exclusive deregulation in knockout cell lines could further indicate that the residual *GLYATL1* expression in the knockdown conditions could retain some protein function that is entirely lost in the *GLYATL1* knockout cell lines.

## 6 Conclusion and Outlook

In my study, I revealed functional insights into a previously under-characterized protein, GLYATL1, within the context of endocrine therapy resistance. My findings demonstrate that *GLYATL1* expression is significantly elevated in resistant cell lines and regulated by estrogen supply and the luminal transcription factors ESR1 and FOXA1. While overexpression of *GLYATL1* alone did not induce a resistant phenotype, knock-out led to notable epigenetic reprogramming, specifically affecting the H3K27, H3K4, and H3K64 histone marks. This reprogramming was accompanied by the activation of p53 and JAK-STAT signaling pathways and the downregulation of E2F targets and the TGF $\beta$  pathway, which ultimately could contribute to the observed partial re-sensitization to endocrine therapy.

Due to the distinct localization of GLYATL1 in the mitochondria, the alterations in pathway activation and epigenetic modifications might be due to a secondary effect triggered by GLYATL1. I could observe that GLYATL1 contributed to succinate accumulation and played a role in modulating basal oxidative stress levels, potentially by catalyzing the generation of antioxidants. Further studies are necessary to elucidate the direct mechanism and the involvement of GLYATL1 in the complex interplay of succinate, ROS, epigenetic modifications, and deregulation of signaling pathways. Expanded analysis of potential substrates of GLYATL1, such as aryl-CoA or long-chain fatty acyl-CoA, and glutamine tracing could provide deeper mechanistic insights into endocrine therapy-resistant cell lines. Moreover, the possible direct effect of diminished oxidative stress and accumulated succinate on downstream effector pathways requires further investigation. Based on the literature possible connections of the observed deregulation of p53, TGF $\beta$ , and JAK-STAT pathways could be mediated by altered ROS or succinate levels, however, this needs to be experimentally verified in the used cellular context.

The activation of the potential downstream pathways is predicted by several algorithms based on RNA sequencing and full proteome data. Further analysis of the involved proteins using Western blots or phospho-proteomics to determine the activation of key kinases could further support the deregulation of these pathways to strengthen the predicted findings.

## Conclusion and Outlook

---

Additionally, conducting ChIP-sequencing with the identified histone marks could provide valuable insights into the role of epigenetic regulation at the individual gene and at specific pathway levels.

Identification of the missing link in the role of *GLYATL1* as a potential maintenance protein of the endocrine therapy-resistant phenotype could help to understand the molecular reshaping in resistant cells and provide potential targeting strategies for the treatment of resistant tumors.

## Abbreviations

<b>αKG</b>	Alpha-ketoglutarate
<b>ACSL3</b>	Acyl-CoA Synthetase Long-Chain Family Member 3
<b>ACTB</b>	Actin
<b>AI</b>	Aromatase inhibitor
<b>AKT</b>	Serine/threonine protein kinase
<b>BCA</b>	Bicinchoninic acid
<b>BioID</b>	Proximity-dependent biotin identification
<b>BRCA1/2</b>	Breast cancer type 1/2 susceptibility protein
<b>BSA</b>	Bovine serum albumin
<b>CD49F</b>	Integrin α-6
<b>CDK</b>	Cyclin-dependent kinases
<b>CI</b>	Confidence Interval
<b>CO<sub>2</sub></b>	Carbon dioxide
<b>CoA</b>	Coenzyme A
<b>CS-FBS</b>	Charcoal Stripped FBS
<b>CYO</b>	Cytochrome P450
<b>CYP2D6</b>	Cytochrome P450 2D6
<b>CytoTOF</b>	Cytometry by time-of-flight
<b>DA</b>	Diamide
<b>DMEM</b>	Dulbecco's modified eagle's medium
<b>DMSO</b>	Dimethyl sulfoxide
<b>DNMT-1</b>	DNA methyltransferase 1
<b>DTT</b>	Dithiothreitol
<b>E2</b>	Estrogen
<b>EDTA</b>	Ethylenediaminetetraacetic acid
<b>EGFR</b>	Epidermal growth factor receptors
<b>EpiTOF</b>	Epigenetic-focused cytometry by time-of-flight
<b>ER</b>	Estrogen receptor α
<b>ERE</b>	Estrogen-response element
<b>ESR1</b>	Gene encoding the Estrogen receptor α
<b>FACS</b>	Fluorescence-activated cell sorting
<b>FBS</b>	Fetal bovine serum
<b>FDA</b>	Food and Drug Administration

<b>FDR</b>	False Discovery Rate
<b>FGFR</b>	Fibroblast growth factor receptor
<b>FOXA1</b>	Forkhead box A1
<b>FOXM1</b>	Forkhead box protein M1
<b>FSC</b>	Forward scatter
<b>GLYATL1</b>	Glycine N-Acyltransferase Like 1
<b>H<sub>2</sub>O<sub>2</sub></b>	Hydrogen Peroxide
<b>H3KX</b>	Histone 3 Lysine residue at position X
<b>HAT</b>	Histone acyltransferases
<b>HDAC</b>	Histone deacetylases
<b>HER2</b>	Human epidermal growth factor receptor 2
<b>ICL</b>	Imperial College London
<b>IGF-IR</b>	Insulin-like growth factor-I receptor
<b>IRES</b>	Internal Ribosome Entry site
<b>JAK</b>	Janus Kinase
<b>JNK</b>	Stress-activated protein kinase JNK
<b>KAT</b>	Lysine acetyltransferases
<b>kDa</b>	Kilo Dalton
<b>Ki-67</b>	Proliferation marker protein ki-67
<b>KO</b>	Knock-out
<b>LEO1</b>	RNA polymerase-associated protein LEO1
<b>Log<sub>2</sub>FC</b>	Log 2-fold changes
<b>LS-MS</b>	Liquid chromatography-mass spectrometry
<b>LTED</b>	Long-term estrogen deprived
<b>MAPK</b>	Mitogen-activated protein kinase
<b>METABRIC</b>	Molecular Taxonomy of Breast Cancer International Consortium
<b>mRNA</b>	Messenger ribonucleic acid
<b>MSigDB</b>	Molecular Signature Database
<b>mTOR</b>	Serine/threonine-protein kinase mTOR
<b>NEAA</b>	Non-essential Amino Acids
<b>NES</b>	Normalized Enrichment Score
<b>NFkB</b>	nuclear factor 'kappa-light-chain-enhancer' of activated B-cells

---

<b>OE</b>	Overexpression
<b>Orp1</b>	Glutathione peroxidase-like peroxiredoxin HYR1
<b>OS</b>	Overall survival
<b>p53</b>	Cellular tumor antigen p53
<b>P/S</b>	Penicillin/Streptomycin
<b>PARP</b>	Poly(ADP-ribose) polymerases
<b>PBS</b>	Phosphate-buffered saline
<b>PCR</b>	Polymerase chain reaction
<b>PCA</b>	Principal component analysis
<b>PD-1</b>	Programmed cell death protein 1
<b>PD-L1</b>	Programmed cell death ligand 1
<b>PFA</b>	Paraformaldehyde
<b>PFS</b>	Progression-free survival
<b>PI3K</b>	Phosphatidylinositol-4,5-bisphosphate 3-kinase
<b>PIP2</b>	Phosphatidylinositol-4,5-bisphosphate
<b>PIP3</b>	Phosphatidylinositol-3,4,5-trisphosphate
<b>PR</b>	Progesterone Receptor
<b>PRM</b>	Parallel Reaction Monitoring
<b>PUM1</b>	Pumilio homolog 1
<b>PuroR</b>	Puromycin resistance
<b>RB</b>	Retinoblastoma protein
<b>RT-qPCR</b>	Quantitative reverse transcriptase polymerase chain reaction
<b>RIPA</b>	Radioimmunoprecipitation
<b>RNA</b>	Ribonucleic acid
<b>ROS</b>	Reactive oxygen species
<b>SCC</b>	Side scatter
<b>SD</b>	Standard deviation
<b>SDS-PAGE</b>	Sodium dodecyl sulfate polyacrylamide gel electrophoresis
<b>SEM</b>	Standard error of the mean
<b>SERD</b>	Selective estrogen receptor degrader
<b>SERM</b>	Selective estrogen receptor modulator
<b>siRNA</b>	Small interfering ribonucleic acid
<b>Sirt</b>	Sirtuins
<b>STAT</b>	Signal transducer and transcription activator

## Abbreviations

---

<b>TCA</b>	Tricarboxylic acid
<b>TCGA</b>	The Cancer Genome Atlas
<b>TF-CHIP</b>	Transcription Factor Chromatin Immunoprecipitation
<b>TGF<math>\beta</math></b>	Transforming growth factor $\beta$
<b>TNF<math>\alpha</math></b>	Tumor necrosis factor $\alpha$
<b>TP53</b>	Tumor protein 53
<b>Trail</b>	TNF-related apoptosis-inducing ligand
<b>Trop-2</b>	Trophoblast cell-surface antigen 2
<b>VEGFR</b>	Vascular endothelial growth factor receptor
<b>WNT</b>	Wingless-related integration site
<b>WT</b>	Wildtype

## Acknowledgments

First of all, I would like to thank my PhD supervisor Prof. Dr. Stefan Wiemann for giving me the opportunity to join the Molecular Genome Analysis Division and for his support throughout my research.

I would like to acknowledge the contributions of my Thesis Advisory Committee members, Prof. Dr. Rüdiger Hell, Prof. Dr. Peter Angel, Prof. Dr. Moshe Oren, and Dr. Yael Aylon, for their insightful feedback, critical discussions, and support. I would like to further thank, Prof. Dr. Stefan Wiemann, Prof. Dr. Rüdiger Hell, Prof. Dr. Peter Angel, and Dr. Marco Binder for agreeing to take part in my defense as examiners.

I wish to acknowledge the financial support from the Cancer TRAX, which made this research possible.

The work of this PhD thesis is the result of the combined efforts of many people. I would like to thank my collaborators at the Weizmann Institute in Rehovot, Prof. Dr. Moshe Oren, Dr. Yael Aylon, Dr. Eviatar Weizman, and Dr. Tomer-Meir Salame, for welcoming me to Israel and helping me with the EpiTOF experiment. I am very grateful for the support of the DKFZ core facilities: the Microscopy Core Facility, the Mass Spectrometry Core Facility, the Next Generation Sequencing Core Facility, the Antibody Core Facility, and especially the Cellular Tools Core Facility, Dr. Rainer Will, Heike Wilhelm, Daniela Heiss, and Katja Bauer. Thank you for your efforts with hundreds of single clones and your general support. I would also like to thank Dr. Lisa Schlicker and Prof. Dr. Almuth Schulz for helping me to enter the field of metabolomics. Dr. Antoni Martija and Prof. Dr. Stefan Pusch for their support with the BiOLD2 experiment. I would also like to thank Dr. Jana Samrai and Teresa Marker for their help with the ROS sensor.

For the last four years, I have been happy to be part of the Molecular Genome Analysis Division. During this time, we have had many people come and go who have accompanied me. Thank you all for being part of my journey. It has been a pleasure to work with all of you.

I would especially like to thank Dr. Cindy Körner for the numerous discussions, your constant support, and all your ideas.

## Acknowledgments

---

Thanks to Corinna, Sabine, Angelika, and especially Sara and Daniela for their help in the lab. Moreover, I am also grateful to Birgitta and Veronica for their bioinformatic analyses.

A special thanks goes to my office mate, Luisa. Thank you for all the talks we had, the ideas, all the R problems you helped me solve, your endless support, and the memorable time we had in and even more out of the lab.

My heartfelt thanks to all my friends in Heidelberg and outside, my parents, my sisters, and especially Thomas. Thank you for believing in me and for your constant support. Thank you for every single wonderful moment we spent together, which makes my life so enjoyable.

---

## References

1. Bray, F., et al., *Global cancer statistics 2022: GLOBOCAN estimates of incidence and mortality worldwide for 36 cancers in 185 countries*. *CA Cancer J Clin*, 2024. **74**(3): p. 229-263.
2. WHO. *Breast cancer*. 2024 [09.07.2024]; Available from: <https://www.who.int/news-room/fact-sheets/detail/breast-cancer>.
3. Giaquinto, A.N., et al., *Breast Cancer Statistics, 2022*. *CA Cancer J Clin*, 2022. **72**(6): p. 524-541.
4. *SEER Cancer Stat Facts: Female Breast Cancer*. 2024 [09.07.2024]; Available from: <https://seer.cancer.gov/statfacts/html/breast.html>.
5. Orrantia-Borunda, E., et al., *Subtypes of Breast Cancer*, in *Breast Cancer*, H.N. Mayrovitz, Editor. 2022: Brisbane (AU).
6. Davey, M.G., et al., *Ki-67 as a Prognostic Biomarker in Invasive Breast Cancer*. *Cancers (Basel)*, 2021. **13**(17).
7. Press, M.F., et al., *HER2 Gene Amplification Testing by Fluorescent In Situ Hybridization (FISH): Comparison of the ASCO-College of American Pathologists Guidelines With FISH Scores Used for Enrollment in Breast Cancer International Research Group Clinical Trials*. *J Clin Oncol*, 2016. **34**(29): p. 3518-3528.
8. Allison, K.H., et al., *Estrogen and Progesterone Receptor Testing in Breast Cancer: ASCO/CAP Guideline Update*. *J Clin Oncol*, 2020. **38**(12): p. 1346-1366.
9. Zagami, P. and L.A. Carey, *Triple negative breast cancer: Pitfalls and progress*. *NPJ Breast Cancer*, 2022. **8**(1): p. 95.
10. Badowska-Kozakiewicz, A.M. and M.P. Budzik, *Immunohistochemical characteristics of basal-like breast cancer*. *Contemp Oncol (Pozn)*, 2016. **20**(6): p. 436-443.
11. Hubalek, M., T. Czech, and H. Muller, *Biological Subtypes of Triple-Negative Breast Cancer*. *Breast Care (Basel)*, 2017. **12**(1): p. 8-14.
12. Alluri, P. and L.A. Newman, *Basal-like and triple-negative breast cancers: searching for positives among many negatives*. *Surg Oncol Clin N Am*, 2014. **23**(3): p. 567-77.
13. Cancer Genome Atlas, N., *Comprehensive molecular portraits of human breast tumours*. *Nature*, 2012. **490**(7418): p. 61-70.
14. Liedtke, C., et al., *Response to neoadjuvant therapy and long-term survival in patients with triple-negative breast cancer*. *J Clin Oncol*, 2008. **26**(8): p. 1275-81.
15. Carey, L.A., et al., *The triple negative paradox: primary tumor chemosensitivity of breast cancer subtypes*. *Clin Cancer Res*, 2007. **13**(8): p. 2329-34.

## References

---

16. Dent, R., et al., *Triple-negative breast cancer: clinical features and patterns of recurrence*. Clin Cancer Res, 2007. **13**(15 Pt 1): p. 4429-34.
17. von Minckwitz, G., et al., *Neoadjuvant carboplatin in patients with triple-negative and HER2-positive early breast cancer (GeparSixto; GBG 66): a randomised phase 2 trial*. Lancet Oncol, 2014. **15**(7): p. 747-56.
18. Sikov, W.M., et al., *Impact of the addition of carboplatin and/or bevacizumab to neoadjuvant once-per-week paclitaxel followed by dose-dense doxorubicin and cyclophosphamide on pathologic complete response rates in stage II to III triple-negative breast cancer: CALGB 40603 (Alliance)*. J Clin Oncol, 2015. **33**(1): p. 13-21.
19. Bardia, A., et al., *Efficacy and Safety of Anti-Trop-2 Antibody Drug Conjugate Sacituzumab Govitecan (IMMU-132) in Heavily Pretreated Patients With Metastatic Triple-Negative Breast Cancer*. J Clin Oncol, 2017. **35**(19): p. 2141-2148.
20. Bardia, A., et al., *Sacituzumab Govitecan-hziy in Refractory Metastatic Triple-Negative Breast Cancer*. N Engl J Med, 2019. **380**(8): p. 741-751.
21. Bardia, A., et al., *Sacituzumab Govitecan in Metastatic Triple-Negative Breast Cancer*. N Engl J Med, 2021. **384**(16): p. 1529-1541.
22. Bardia, A., et al., *Biomarker analyses in the phase III ASCENT study of sacituzumab govitecan versus chemotherapy in patients with metastatic triple-negative breast cancer*. Ann Oncol, 2021. **32**(9): p. 1148-1156.
23. Robson, M., et al., *Olaparib for Metastatic Breast Cancer in Patients with a Germline BRCA Mutation*. N Engl J Med, 2017. **377**(6): p. 523-533.
24. Robson, M.E., et al., *OlympiAD final overall survival and tolerability results: Olaparib versus chemotherapy treatment of physician's choice in patients with a germline BRCA mutation and HER2-negative metastatic breast cancer*. Ann Oncol, 2019. **30**(4): p. 558-566.
25. Litton, J.K., et al., *Talazoparib in Patients with Advanced Breast Cancer and a Germline BRCA Mutation*. N Engl J Med, 2018. **379**(8): p. 753-763.
26. Schmid, P., et al., *Atezolizumab and Nab-Paclitaxel in Advanced Triple-Negative Breast Cancer*. N Engl J Med, 2018. **379**(22): p. 2108-2121.
27. Adams, S., et al., *Atezolizumab Plus nab-Paclitaxel in the Treatment of Metastatic Triple-Negative Breast Cancer With 2-Year Survival Follow-up: A Phase 1b Clinical Trial*. JAMA Oncol, 2019. **5**(3): p. 334-342.
28. Adams, S., et al., *Pembrolizumab monotherapy for previously untreated, PD-L1-positive, metastatic triple-negative breast cancer: cohort B of the phase II KEYNOTE-086 study*. Ann Oncol, 2019. **30**(3): p. 405-411.
29. Adams, S., et al., *Pembrolizumab monotherapy for previously treated metastatic triple-negative breast cancer: cohort A of the phase II KEYNOTE-086 study*. Ann Oncol, 2019. **30**(3): p. 397-404.
30. Moasser, M.M., *The oncogene HER2: its signaling and transforming functions and its role in human cancer pathogenesis*. Oncogene, 2007. **26**(45): p. 6469-87.

31. Rubin, E., et al., *Molecular Targeting of the Human Epidermal Growth Factor Receptor-2 (HER2) Genes across Various Cancers*. Int J Mol Sci, 2024. **25**(2).
32. Iqbal, N. and N. Iqbal, *Human Epidermal Growth Factor Receptor 2 (HER2) in Cancers: Overexpression and Therapeutic Implications*. Mol Biol Int, 2014. **2014**: p. 852748.
33. Zaczek, A., B. Brandt, and K.P. Bielawski, *The diverse signaling network of EGFR, HER2, HER3 and HER4 tyrosine kinase receptors and the consequences for therapeutic approaches*. Histol Histopathol, 2005. **20**(3): p. 1005-15.
34. Pollock, N.I. and J.R. Grandis, *HER2 as a therapeutic target in head and neck squamous cell carcinoma*. Clin Cancer Res, 2015. **21**(3): p. 526-33.
35. Slamon, D.J., et al., *Use of chemotherapy plus a monoclonal antibody against HER2 for metastatic breast cancer that overexpresses HER2*. N Engl J Med, 2001. **344**(11): p. 783-92.
36. Romond, E.H., et al., *Trastuzumab plus adjuvant chemotherapy for operable HER2-positive breast cancer*. N Engl J Med, 2005. **353**(16): p. 1673-84.
37. Joensuu, H., et al., *Adjuvant docetaxel or vinorelbine with or without trastuzumab for breast cancer*. N Engl J Med, 2006. **354**(8): p. 809-20.
38. Baselga, J., et al., *Pertuzumab plus trastuzumab plus docetaxel for metastatic breast cancer*. N Engl J Med, 2012. **366**(2): p. 109-19.
39. Prat, A., et al., *Prognostic significance of progesterone receptor-positive tumor cells within immunohistochemically defined luminal A breast cancer*. J Clin Oncol, 2013. **31**(2): p. 203-9.
40. Beyene, D., et al., *Cyclin A2 and Ki-67 proliferation markers could be used to identify tumors with poor prognosis in African American women with breast cancer*. J Cancer Biol, 2023. **4**(1): p. 3-16.
41. Weinberger, C., et al., *Domain structure of human glucocorticoid receptor and its relationship to the v-erb-A oncogene product*. Nature, 1985. **318**(6047): p. 670-2.
42. Green, S., et al., *Cloning of the human oestrogen receptor cDNA*. J Steroid Biochem, 1986. **24**(1): p. 77-83.
43. Kumar, V. and P. Chambon, *The estrogen receptor binds tightly to its responsive element as a ligand-induced homodimer*. Cell, 1988. **55**(1): p. 145-56.
44. Shiau, A.K., et al., *The structural basis of estrogen receptor/coactivator recognition and the antagonism of this interaction by tamoxifen*. Cell, 1998. **95**(7): p. 927-37.
45. Schuurman, T.N., et al., *Tamoxifen and pregnancy: an absolute contraindication?* Breast Cancer Res Treat, 2019. **175**(1): p. 17-25.
46. Brzozowski, A.M., et al., *Molecular basis of agonism and antagonism in the oestrogen receptor*. Nature, 1997. **389**(6652): p. 753-8.

## References

---

47. Robert, N.J., *Clinical efficacy of tamoxifen*. Oncology (Williston Park), 1997. **11**(2 Suppl 1): p. 15-20.
48. Cluze, C., et al., *Adjuvant endocrine therapy with tamoxifen in young women with breast cancer: determinants of interruptions vary over time*. Ann Oncol, 2012. **23**(4): p. 882-90.
49. Davies, C., et al., *Long-term effects of continuing adjuvant tamoxifen to 10 years versus stopping at 5 years after diagnosis of oestrogen receptor-positive breast cancer: ATLAS, a randomised trial*. Lancet, 2013. **381**(9869): p. 805-16.
50. Wijayaratne, A.L., et al., *Comparative analyses of mechanistic differences among antiestrogens*. Endocrinology, 1999. **140**(12): p. 5828-40.
51. Wijayaratne, A.L. and D.P. McDonnell, *The human estrogen receptor-alpha is a ubiquitinated protein whose stability is affected differentially by agonists, antagonists, and selective estrogen receptor modulators*. J Biol Chem, 2001. **276**(38): p. 35684-92.
52. Bross, P.F., et al., *FDA drug approval summaries: fulvestrant*. Oncologist, 2002. **7**(6): p. 477-80.
53. Wakeling, A.E. and J. Bowler, *Steroidal pure antioestrogens*. J Endocrinol, 1987. **112**(3): p. R7-10.
54. Chen, D., et al., *Phosphorylation of human estrogen receptor alpha by protein kinase A regulates dimerization*. Mol Cell Biol, 1999. **19**(2): p. 1002-15.
55. Fawell, S.E., et al., *Inhibition of estrogen receptor-DNA binding by the "pure" antiestrogen ICI 164,384 appears to be mediated by impaired receptor dimerization*. Proc Natl Acad Sci U S A, 1990. **87**(17): p. 6883-7.
56. Wu, Y.L., et al., *Structural basis for an unexpected mode of SERM-mediated ER antagonism*. Mol Cell, 2005. **18**(4): p. 413-24.
57. Wittmann, B.M., A. Sherk, and D.P. McDonnell, *Definition of functionally important mechanistic differences among selective estrogen receptor down-regulators*. Cancer Res, 2007. **67**(19): p. 9549-60.
58. Lai, A.C. and C.M. Crews, *Induced protein degradation: an emerging drug discovery paradigm*. Nat Rev Drug Discov, 2017. **16**(2): p. 101-114.
59. Robertson, J.F.R., et al., *Fulvestrant 500 mg versus anastrozole 1 mg for hormone receptor-positive advanced breast cancer (FALCON): an international, randomised, double-blind, phase 3 trial*. Lancet, 2016. **388**(10063): p. 2997-3005.
60. Howell, A., et al., *ICI 182,780 (Faslodex): development of a novel, "pure" antiestrogen*. Cancer, 2000. **89**(4): p. 817-25.
61. Toy, W., et al., *ESR1 ligand-binding domain mutations in hormone-resistant breast cancer*. Nat Genet, 2013. **45**(12): p. 1439-45.
62. Bidard, F.C., et al., *Elacestrant (oral selective estrogen receptor degrader) Versus Standard Endocrine Therapy for Estrogen Receptor-*

- Positive, Human Epidermal Growth Factor Receptor 2-Negative Advanced Breast Cancer: Results From the Randomized Phase III EMERALD Trial.* J Clin Oncol, 2022. **40**(28): p. 3246-3256.
63. Sasano, H., et al., *Immunolocalization of aromatase, 17 alpha-hydroxylase and side-chain-cleavage cytochromes P-450 in the human ovary.* J Reprod Fertil, 1989. **85**(1): p. 163-9.
64. Sasano, H., *Functional pathology of human ovarian steroidogenesis: Normal cycling ovary and steroid-producing neoplasms.* Endocr Pathol, 1994. **5**(2): p. 81-89.
65. Perel, E. and D.W. Killinger, *The interconversion and aromatization of androgens by human adipose tissue.* J Steroid Biochem, 1979. **10**(6): p. 623-7.
66. Schweikert, H.U., L. Milewich, and J.D. Wilson, *Aromatization of androstenedione by cultured human fibroblasts.* J Clin Endocrinol Metab, 1976. **43**(4): p. 785-95.
67. Larionov, A.A., et al., *Aromatase in skeletal muscle.* J Steroid Biochem Mol Biol, 2003. **84**(4): p. 485-92.
68. Smuk, M. and J. Schwers, *Aromatization of androstenedione by human adult liver in vitro.* J Clin Endocrinol Metab, 1977. **45**(5): p. 1009-12.
69. Eiermann, W., et al., *Preoperative treatment of postmenopausal breast cancer patients with letrozole: A randomized double-blind multicenter study.* Ann Oncol, 2001. **12**(11): p. 1527-32.
70. Mouridsen, H., et al., *Superior efficacy of letrozole versus tamoxifen as first-line therapy for postmenopausal women with advanced breast cancer: results of a phase III study of the International Letrozole Breast Cancer Group.* J Clin Oncol, 2001. **19**(10): p. 2596-606.
71. Lonning, P.E., *Pharmacology and clinical experience with exemestane.* Expert Opin Investig Drugs, 2000. **9**(8): p. 1897-905.
72. Graham-Lorence, S. and J.A. Peterson, *P450s: structural similarities and functional differences.* FASEB J, 1996. **10**(2): p. 206-14.
73. Plourde, P.V., M. Dyroff, and M. Dukes, *Arimidex: a potent and selective fourth-generation aromatase inhibitor.* Breast Cancer Res Treat, 1994. **30**(1): p. 103-11.
74. Iveson, T.J., et al., *Phase I study of the oral nonsteroidal aromatase inhibitor CGS 20267 in postmenopausal patients with advanced breast cancer.* Cancer Res, 1993. **53**(2): p. 266-70.
75. Ma, C.X., C.G. Sanchez, and M.J. Ellis, *Predicting endocrine therapy responsiveness in breast cancer.* Oncology (Williston Park), 2009. **23**(2): p. 133-42.
76. Lemmon, M.A. and J. Schlessinger, *Cell signaling by receptor tyrosine kinases.* Cell, 2010. **141**(7): p. 1117-34.

## References

---

77. Templeton, A.J., et al., *Prognostic relevance of receptor tyrosine kinase expression in breast cancer: a meta-analysis*. *Cancer Treat Rev*, 2014. **40**(9): p. 1048-55.
78. Gutierrez, M.C., et al., *Molecular changes in tamoxifen-resistant breast cancer: relationship between estrogen receptor, HER-2, and p38 mitogen-activated protein kinase*. *J Clin Oncol*, 2005. **23**(11): p. 2469-76.
79. Nayar, U., et al., *Acquired HER2 mutations in ER(+) metastatic breast cancer confer resistance to estrogen receptor-directed therapies*. *Nat Genet*, 2019. **51**(2): p. 207-216.
80. Croessmann, S., et al., *Combined Blockade of Activating ERBB2 Mutations and ER Results in Synthetic Lethality of ER+/HER2 Mutant Breast Cancer*. *Clin Cancer Res*, 2019. **25**(1): p. 277-289.
81. Leary, A.F., et al., *Lapatinib restores hormone sensitivity with differential effects on estrogen receptor signaling in cell models of human epidermal growth factor receptor 2-negative breast cancer with acquired endocrine resistance*. *Clin Cancer Res*, 2010. **16**(5): p. 1486-97.
82. Smyth, L.M., et al., *Efficacy and Determinants of Response to HER Kinase Inhibition in HER2-Mutant Metastatic Breast Cancer*. *Cancer Discov*, 2020. **10**(2): p. 198-213.
83. Giltneane, J.M., et al., *Genomic profiling of ER(+) breast cancers after short-term estrogen suppression reveals alterations associated with endocrine resistance*. *Sci Transl Med*, 2017. **9**(402).
84. Turczyk, L., et al., *FGFR2-Driven Signaling Counteracts Tamoxifen Effect on ERalpha-Positive Breast Cancer Cells*. *Neoplasia*, 2017. **19**(10): p. 791-804.
85. Garcia-Recio, S., et al., *FGFR4 regulates tumor subtype differentiation in luminal breast cancer and metastatic disease*. *J Clin Invest*, 2020. **130**(9): p. 4871-4887.
86. Musolino, A., et al., *Phase II, randomized, placebo-controlled study of dovitinib in combination with fulvestrant in postmenopausal patients with HR(+), HER2(-) breast cancer that had progressed during or after prior endocrine therapy*. *Breast Cancer Res*, 2017. **19**(1): p. 18.
87. Coombes, R.C., et al., *Results of the phase IIa RADICAL trial of the FGFR inhibitor AZD4547 in endocrine resistant breast cancer*. *Nat Commun*, 2022. **13**(1): p. 3246.
88. Vanhaesebroeck, B., et al., *The emerging mechanisms of isoform-specific PI3K signalling*. *Nat Rev Mol Cell Biol*, 2010. **11**(5): p. 329-41.
89. Miller, T.W., et al., *Hyperactivation of phosphatidylinositol-3 kinase promotes escape from hormone dependence in estrogen receptor-positive human breast cancer*. *J Clin Invest*, 2010. **120**(7): p. 2406-13.
90. Huang, D., et al., *PIK3CA mutations contribute to fulvestrant resistance in ER-positive breast cancer*. *Am J Transl Res*, 2019. **11**(9): p. 6055-6065.

91. Campbell, R.A., et al., *Phosphatidylinositol 3-kinase/AKT-mediated activation of estrogen receptor alpha: a new model for anti-estrogen resistance*. J Biol Chem, 2001. **276**(13): p. 9817-24.
92. Baselga, J., et al., *Buparlisib plus fulvestrant versus placebo plus fulvestrant in postmenopausal, hormone receptor-positive, HER2-negative, advanced breast cancer (BELLE-2): a randomised, double-blind, placebo-controlled, phase 3 trial*. Lancet Oncol, 2017. **18**(7): p. 904-916.
93. Jones, R.H., et al., *Fulvestrant plus capivasertib versus placebo after relapse or progression on an aromatase inhibitor in metastatic, oestrogen receptor-positive breast cancer (FAKTION): a multicentre, randomised, controlled, phase 2 trial*. Lancet Oncol, 2020. **21**(3): p. 345-357.
94. Bachelot, T., et al., *Randomized phase II trial of everolimus in combination with tamoxifen in patients with hormone receptor-positive, human epidermal growth factor receptor 2-negative metastatic breast cancer with prior exposure to aromatase inhibitors: a GINECO study*. J Clin Oncol, 2012. **30**(22): p. 2718-24.
95. Baselga, J., et al., *Everolimus in postmenopausal hormone-receptor-positive advanced breast cancer*. N Engl J Med, 2012. **366**(6): p. 520-9.
96. Andre, F., et al., *Alpelisib for PIK3CA-Mutated, Hormone Receptor-Positive Advanced Breast Cancer*. N Engl J Med, 2019. **380**(20): p. 1929-1940.
97. Janku, F., T.A. Yap, and F. Meric-Bernstam, *Targeting the PI3K pathway in cancer: are we making headway?* Nat Rev Clin Oncol, 2018. **15**(5): p. 273-291.
98. Said, T.K., et al., *Progesterone, in addition to estrogen, induces cyclin D1 expression in the murine mammary epithelial cell, in vivo*. Endocrinology, 1997. **138**(9): p. 3933-9.
99. Altucci, L., et al., *Estrogen induces early and timed activation of cyclin-dependent kinases 4, 5, and 6 and increases cyclin messenger ribonucleic acid expression in rat uterus*. Endocrinology, 1997. **138**(3): p. 978-84.
100. Topacio, B.R., et al., *Cyclin D-Cdk4,6 Drives Cell-Cycle Progression via the Retinoblastoma Protein's C-Terminal Helix*. Mol Cell, 2019. **74**(4): p. 758-770 e4.
101. Thangavel, C., et al., *Therapeutically activating RB: reestablishing cell cycle control in endocrine therapy-resistant breast cancer*. Endocr Relat Cancer, 2011. **18**(3): p. 333-45.
102. Finn, R.S., et al., *PD 0332991, a selective cyclin D kinase 4/6 inhibitor, preferentially inhibits proliferation of luminal estrogen receptor-positive human breast cancer cell lines in vitro*. Breast Cancer Res, 2009. **11**(5): p. R77.
103. Finn, R.S., et al., *The cyclin-dependent kinase 4/6 inhibitor palbociclib in combination with letrozole versus letrozole alone as first-line treatment of*

## References

---

- oestrogen receptor-positive, HER2-negative, advanced breast cancer (PALOMA-1/TRIO-18): a randomised phase 2 study.* Lancet Oncol, 2015. **16**(1): p. 25-35.
104. Walker, A.J., et al., *FDA Approval of Palbociclib in Combination with Fulvestrant for the Treatment of Hormone Receptor-Positive, HER2-Negative Metastatic Breast Cancer.* Clin Cancer Res, 2016. **22**(20): p. 4968-4972.
105. Goetz, M.P., et al., *MONARCH 3: Abemaciclib As Initial Therapy for Advanced Breast Cancer.* J Clin Oncol, 2017. **35**(32): p. 3638-3646.
106. Finn, R.S., et al., *Palbociclib and Letrozole in Advanced Breast Cancer.* N Engl J Med, 2016. **375**(20): p. 1925-1936.
107. Hortobagyi, G.N., et al., *Ribociclib as First-Line Therapy for HR-Positive, Advanced Breast Cancer.* N Engl J Med, 2016. **375**(18): p. 1738-1748.
108. Schiavon, G., et al., *Analysis of ESR1 mutation in circulating tumor DNA demonstrates evolution during therapy for metastatic breast cancer.* Sci Transl Med, 2015. **7**(313): p. 313ra182.
109. Zhang, Q.X., et al., *An estrogen receptor mutant with strong hormone-independent activity from a metastatic breast cancer.* Cancer Res, 1997. **57**(7): p. 1244-9.
110. Li, S., et al., *Endocrine-therapy-resistant ESR1 variants revealed by genomic characterization of breast-cancer-derived xenografts.* Cell Rep, 2013. **4**(6): p. 1116-30.
111. Garcia-Carpizo, V., et al., *The growing role of gene methylation on endocrine function.* J Mol Endocrinol, 2011. **47**(2): p. R75-89.
112. Zhou, Q., P. Atadja, and N.E. Davidson, *Histone deacetylase inhibitor LBH589 reactivates silenced estrogen receptor alpha (ER) gene expression without loss of DNA hypermethylation.* Cancer Biol Ther, 2007. **6**(1): p. 64-9.
113. Bicaku, E., et al., *Selective inhibition of histone deacetylase 2 silences progesterone receptor-mediated signaling.* Cancer Res, 2008. **68**(5): p. 1513-9.
114. Sabnis, G.J., et al., *Functional activation of the estrogen receptor-alpha and aromatase by the HDAC inhibitor entinostat sensitizes ER-negative tumors to letrozole.* Cancer Res, 2011. **71**(5): p. 1893-903.
115. Keen, J.C., et al., *A novel histone deacetylase inhibitor, scriptaid, enhances expression of functional estrogen receptor alpha (ER) in ER negative human breast cancer cells in combination with 5-aza 2'-deoxycytidine.* Breast Cancer Res Treat, 2003. **81**(3): p. 177-86.
116. Giacinti, L., et al., *Scriptaid effects on breast cancer cell lines.* J Cell Physiol, 2012. **227**(10): p. 3426-33.
117. Yang, X., et al., *Synergistic activation of functional estrogen receptor (ER)-alpha by DNA methyltransferase and histone deacetylase inhibition*

- in human ER-alpha-negative breast cancer cells*. *Cancer Res*, 2001. **61**(19): p. 7025-9.
118. Fan, J., et al., *ER alpha negative breast cancer cells restore response to endocrine therapy by combination treatment with both HDAC inhibitor and DNMT inhibitor*. *J Cancer Res Clin Oncol*, 2008. **134**(8): p. 883-90.
119. Desta, Z., et al., *Comprehensive evaluation of tamoxifen sequential biotransformation by the human cytochrome P450 system in vitro: prominent roles for CYP3A and CYP2D6*. *J Pharmacol Exp Ther*, 2004. **310**(3): p. 1062-75.
120. Fabian, C., L. Tilzer, and L. Sternson, *Comparative binding affinities of tamoxifen, 4-hydroxytamoxifen, and desmethyltamoxifen for estrogen receptors isolated from human breast carcinoma: correlation with blood levels in patients with metastatic breast cancer*. *Biopharm Drug Dispos*, 1981. **2**(4): p. 381-90.
121. Jin, Y., et al., *CYP2D6 genotype, antidepressant use, and tamoxifen metabolism during adjuvant breast cancer treatment*. *J Natl Cancer Inst*, 2005. **97**(1): p. 30-9.
122. Johnson, M.D., et al., *Pharmacological characterization of 4-hydroxy-N-desmethyl tamoxifen, a novel active metabolite of tamoxifen*. *Breast Cancer Res Treat*, 2004. **85**(2): p. 151-9.
123. Dehal, S.S. and D. Kupfer, *CYP2D6 catalyzes tamoxifen 4-hydroxylation in human liver*. *Cancer Res*, 1997. **57**(16): p. 3402-6.
124. Jordan, V.C., *New insights into the metabolism of tamoxifen and its role in the treatment and prevention of breast cancer*. *Steroids*, 2007. **72**(13): p. 829-42.
125. Katzenellenbogen, B.S., et al., *Proliferation, hormonal responsiveness, and estrogen receptor content of MCF-7 human breast cancer cells grown in the short-term and long-term absence of estrogens*. *Cancer Res*, 1987. **47**(16): p. 4355-60.
126. Cheng, G.J., E.Y. Leung, and D.C. Singleton, *In vitro breast cancer models for studying mechanisms of resistance to endocrine therapy*. *Explor Target Antitumor Ther*, 2022. **3**(3): p. 297-320.
127. Milosevic, J., et al., *Clinical instability of breast cancer markers is reflected in long-term in vitro estrogen deprivation studies*. *BMC Cancer*, 2013. **13**: p. 473.
128. Coser, K.R., et al., *Antiestrogen-resistant subclones of MCF-7 human breast cancer cells are derived from a common monoclonal drug-resistant progenitor*. *Proc Natl Acad Sci U S A*, 2009. **106**(34): p. 14536-41.
129. Beumers, L., et al., *Clonal heterogeneity in ER+ breast cancer reveals the proteasome and PKC as potential therapeutic targets*. *NPJ Breast Cancer*, 2023. **9**(1): p. 97.

## References

---

130. Borgoni, S., et al., *Time-Resolved Profiling Reveals ATF3 as a Novel Mediator of Endocrine Resistance in Breast Cancer*. *Cancers (Basel)*, 2020. **12**(10).
131. Sofyali, E., *GLYATL1 promotes endocrine therapy resistance in breast cancer*, in *Molecular Genome Analysis*. 2019, University of Heidelberg.
132. Zhang, H.e.a., *Molecular Cloning and Characterization of a Novel Human Glycine-N-acyltransferase Gene GLYATL1, Which Activates Transcriptional Activity of HSE Pathway*. *Int. J. Mol. Sci.*, 2007. **8**: p. 433-444.
133. Kuhn, S., et al., *The glycine N-acyltransferases, GLYAT and GLYATL1, contribute to the detoxification of isovaleryl-CoA - an in-silico and in vitro validation*. *Comput Struct Biotechnol J*, 2023. **21**: p. 1236-1248.
134. Matsuo, M., et al., *Designation of enzyme activity of glycine-N-acyltransferase family genes and depression of glycine-N-acyltransferase in human hepatocellular carcinoma*. *Biochem Biophys Res Commun*, 2012. **420**(4): p. 901-6.
135. Zeng, T., et al., *The landscape of extrachromosomal circular DNA (eccDNA) in the normal hematopoiesis and leukemia evolution*. *Cell Death Discov*, 2022. **8**(1): p. 400.
136. Xie, Y., et al., *Identification of glutamine metabolism-related gene signature to predict colorectal cancer prognosis*. *J Cancer*, 2024. **15**(10): p. 3199-3214.
137. Zhang, Z., et al., *The involvement of high succinylation modification in the development of prostate cancer*. *Front Oncol*, 2022. **12**: p. 1034605.
138. Nalla, A.K., et al., *Lentiviral vector-mediated insertional mutagenesis screen identifies genes that influence androgen independent prostate cancer progression and predict clinical outcome*. *Mol Carcinog*, 2016. **55**(11): p. 1761-1771.
139. Eich, M.L., et al., *Characterization of glycine-N-acyltransferase like 1 (GLYATL1) in prostate cancer*. *Prostate*, 2019. **79**(14): p. 1629-1639.
140. Deng, L. and H. Jiang, *Decreased Expression of GLYATL1 Predicts Poor Prognosis in Patients with Clear Cell Renal Cell Carcinoma*. *Int J Gen Med*, 2023. **16**: p. 3757-3768.
141. Zhang, Y., et al., *The value of erlotinib related target molecules in kidney renal cell carcinoma via bioinformatics analysis*. *Gene*, 2022. **816**: p. 146173.
142. Sun, R., et al., *Identification of Ten Core Hub Genes as Potential Biomarkers and Treatment Target for Hepatoblastoma*. *Front Oncol*, 2021. **11**: p. 591507.
143. Guan, R., et al., *The expression and prognostic value of GLYATL1 and its potential role in hepatocellular carcinoma*. *J Gastrointest Oncol*, 2020. **11**(6): p. 1305-1321.

144. Schindelin, J., et al., *Fiji: an open-source platform for biological-image analysis*. Nat Methods, 2012. **9**(7): p. 676-82.
145. Berthois, Y., J.A. Katzenellenbogen, and B.S. Katzenellenbogen, *Phenol red in tissue culture media is a weak estrogen: implications concerning the study of estrogen-responsive cells in culture*. Proc Natl Acad Sci U S A, 1986. **83**(8): p. 2496-500.
146. Balasubramanyam, K., et al., *Polyisoprenylated benzophenone, garcinol, a natural histone acetyltransferase inhibitor, represses chromatin transcription and alters global gene expression*. J Biol Chem, 2004. **279**(32): p. 33716-26.
147. Lobera, M., et al., *Selective class IIa histone deacetylase inhibition via a nonchelating zinc-binding group*. Nat Chem Biol, 2013. **9**(5): p. 319-25.
148. Frankish, A., et al., *GENCODE: reference annotation for the human and mouse genomes in 2023*. Nucleic Acids Res, 2023. **51**(D1): p. D942-D949.
149. Andrews, S. *FastQC - A Quality Control application for FastQ files*. Available from: <https://github.com/s-andrews/FastQC>.
150. Ramirez, F., et al., *deepTools2: a next generation web server for deep-sequencing data analysis*. Nucleic Acids Res, 2016. **44**(W1): p. W160-5.
151. Anders, S., P.T. Pyl, and W. Huber, *HTSeq--a Python framework to work with high-throughput sequencing data*. Bioinformatics, 2015. **31**(2): p. 166-9.
152. Schubert, M., et al., *Perturbation-response genes reveal signaling footprints in cancer gene expression*. Nat Commun, 2018. **9**(1): p. 20.
153. Badia, I.M.P., et al., *decoupleR: ensemble of computational methods to infer biological activities from omics data*. Bioinform Adv, 2022. **2**(1): p. vbac016.
154. Muller-Dott, S., et al., *Expanding the coverage of regulons from high-confidence prior knowledge for accurate estimation of transcription factor activities*. Nucleic Acids Res, 2023. **51**(20): p. 10934-10949.
155. Garcia-Alonso, L., et al., *Benchmark and integration of resources for the estimation of human transcription factor activities*. Genome Res, 2019. **29**(8): p. 1363-1375.
156. Subramanian, A., et al., *Gene set enrichment analysis: a knowledge-based approach for interpreting genome-wide expression profiles*. Proc Natl Acad Sci U S A, 2005. **102**(43): p. 15545-50.
157. Mootha, V.K., et al., *PGC-1alpha-responsive genes involved in oxidative phosphorylation are coordinately downregulated in human diabetes*. Nat Genet, 2003. **34**(3): p. 267-73.
158. Kim, D.I., et al., *An improved smaller biotin ligase for BioID proximity labeling*. Mol Biol Cell, 2016. **27**(8): p. 1188-96.

## References

---

159. Hughes, C.S., et al., *Single-pot, solid-phase-enhanced sample preparation for proteomics experiments*. Nat Protoc, 2019. **14**(1): p. 68-85.
160. MacLean, B., et al., *Skyline: an open source document editor for creating and analyzing targeted proteomics experiments*. Bioinformatics, 2010. **26**(7): p. 966-8.
161. Werley, C.A., et al., *Multiplexed Optical Sensors in Arrayed Islands of Cells for multimodal recordings of cellular physiology*. Nat Commun, 2020. **11**(1): p. 3881.
162. Agrawal, S., et al., *El-MAVEN: A Fast, Robust, and User-Friendly Mass Spectrometry Data Processing Engine for Metabolomics*. Methods Mol Biol, 2019. **1978**: p. 301-321.
163. Xia, J., et al., *MetaboAnalyst: a web server for metabolomic data analysis and interpretation*. Nucleic Acids Res, 2009. **37**(Web Server issue): p. W652-60.
164. Nowicka, M., et al., *CyTOF workflow: differential discovery in high-throughput high-dimensional cytometry datasets*. F1000Res, 2017. **6**: p. 748.
165. *Kaplan-Meier plotter with custom data*. 10.05.2024; Available from: [https://kmplot.com/custom\\_data](https://kmplot.com/custom_data).
166. Kent, W.J., et al., *The human genome browser at UCSC*. Genome Res, 2002. **12**(6): p. 996-1006.
167. Laganier, J., et al., *From the Cover: Location analysis of estrogen receptor alpha target promoters reveals that FOXA1 defines a domain of the estrogen response*. Proc Natl Acad Sci U S A, 2005. **102**(33): p. 11651-6.
168. Wen, W., et al., *Genetic variations of DNA bindings of FOXA1 and co-factors in breast cancer susceptibility*. Nat Commun, 2021. **12**(1): p. 5318.
169. Roux, K.J., et al., *A promiscuous biotin ligase fusion protein identifies proximal and interacting proteins in mammalian cells*. J Cell Biol, 2012. **196**(6): p. 801-10.
170. Kim, D.I., et al., *Probing nuclear pore complex architecture with proximity-dependent biotinylation*. Proc Natl Acad Sci U S A, 2014. **111**(24): p. E2453-61.
171. Varnaite, R. and S.A. MacNeill, *Meet the neighbors: Mapping local protein interactomes by proximity-dependent labeling with BioID*. Proteomics, 2016. **16**(19): p. 2503-2518.
172. Lavelin, I., et al., *Discovery of novel proteasome inhibitors using a high-content cell-based screening system*. PLoS One, 2009. **4**(12): p. e8503.
173. Thumuluri, V., et al., *DeepLoc 2.0: multi-label subcellular localization prediction using protein language models*. Nucleic Acids Res, 2022. **50**(W1): p. W228-W234.

174. *DeepLoc - 2.0*. 27.06.2024]; Available from: <https://services.healthtech.dtu.dk/services/DeepLoc-2.0/>.
175. Lab, N. *WoLF PSORT-Protein Subcellular Localization Prediction*. 27.06.2024]; Available from: <https://wolfpsort.hgc.jp/>.
176. Horton, P., et al., *WoLF PSORT: protein localization predictor*. *Nucleic Acids Res*, 2007. **35**(Web Server issue): p. W585-7.
177. Pfanner, N., B. Warscheid, and N. Wiedemann, *Mitochondrial proteins: from biogenesis to functional networks*. *Nat Rev Mol Cell Biol*, 2019. **20**(5): p. 267-284.
178. Haddad, A. and S.S. Mohiuddin, *Biochemistry, Citric Acid Cycle*, in *StatPearls*. 2024: Treasure Island (FL).
179. Arnold, P.K. and L.W.S. Finley, *Regulation and function of the mammalian tricarboxylic acid cycle*. *J Biol Chem*, 2023. **299**(2): p. 102838.
180. Zhang, B., et al., *Role of mitochondrial reactive oxygen species in homeostasis regulation*. *Redox Rep*, 2022. **27**(1): p. 45-52.
181. Kuznetsov, A.V., et al., *The Complex Interplay between Mitochondria, ROS and Entire Cellular Metabolism*. *Antioxidants (Basel)*, 2022. **11**(10).
182. Tirichen, H., et al., *Mitochondrial Reactive Oxygen Species and Their Contribution in Chronic Kidney Disease Progression Through Oxidative Stress*. *Front Physiol*, 2021. **12**: p. 627837.
183. Sies, H., *Introductory remarks in oxidative stress*. 1985, London: Academic Press.
184. Ren, W. and H.W. Ai, *Genetically encoded fluorescent redox probes*. *Sensors (Basel)*, 2013. **13**(11): p. 15422-33.
185. Herzog, P.L., et al., *Developing a cell-bound detection system for the screening of oxidase activity using the fluorescent peroxide sensor roGFP2-Orp1*. *Protein Eng Des Sel*, 2020. **33**.
186. Morgan, B., M.C. Sobotta, and T.P. Dick, *Measuring E(GSH) and H<sub>2</sub>O<sub>2</sub> with roGFP2-based redox probes*. *Free Radic Biol Med*, 2011. **51**(11): p. 1943-51.
187. Gutsche, M., et al., *Proximity-based Protein Thiol Oxidation by H<sub>2</sub>O<sub>2</sub>-scavenging Peroxidases*. *Journal of Biological Chemistry*, 2009. **284**(46): p. 31532-31540.
188. Wang, Z., et al., *Genome-wide mapping of HATs and HDACs reveals distinct functions in active and inactive genes*. *Cell*, 2009. **138**(5): p. 1019-31.
189. Dimauro, I., M.P. Paronetto, and D. Caporossi, *Exercise, redox homeostasis and the epigenetic landscape*. *Redox Biol*, 2020. **35**: p. 101477.
190. Sundar, I.K., et al., *Oxidative stress, thiol redox signaling methods in epigenetics*. *Methods Enzymol*, 2010. **474**: p. 213-44.

## References

---

191. Kietzmann, T., et al., *The epigenetic landscape related to reactive oxygen species formation in the cardiovascular system*. Br J Pharmacol, 2017. **174**(12): p. 1533-1554.
192. R, M.S., et al., *Redox Components: Key Regulators of Epigenetic Modifications in Plants*. Int J Mol Sci, 2020. **21**(4).
193. Jin, Q., et al., *Distinct roles of GCN5/PCAF-mediated H3K9ac and CBP/p300-mediated H3K18/27ac in nuclear receptor transactivation*. EMBO J, 2011. **30**(2): p. 249-62.
194. Howe, L., et al., *Histone H3 specific acetyltransferases are essential for cell cycle progression*. Genes Dev, 2001. **15**(23): p. 3144-54.
195. Ornatsky, O.I., et al., *Study of cell antigens and intracellular DNA by identification of element-containing labels and metallointercalators using inductively coupled plasma mass spectrometry*. Anal Chem, 2008. **80**(7): p. 2539-47.
196. Tracey, L.J., Y. An, and M.J. Justice, *CyTOF: An Emerging Technology for Single-Cell Proteomics in the Mouse*. Curr Protoc, 2021. **1**(4): p. e118.
197. Liberzon, A., et al., *The Molecular Signatures Database (MSigDB) hallmark gene set collection*. Cell Syst, 2015. **1**(6): p. 417-425.
198. Holland, C.H., B. Szalai, and J. Saez-Rodriguez, *Transfer of regulatory knowledge from human to mouse for functional genomics analysis*. Biochim Biophys Acta Gene Regul Mech, 2020. **1863**(6): p. 194431.
199. He, Z., J. He, and K. Xie, *KLF4 transcription factor in tumorigenesis*. Cell Death Discov, 2023. **9**(1): p. 118.
200. Beacon, T.H., et al., *The dynamic broad epigenetic (H3K4me3, H3K27ac) domain as a mark of essential genes*. Clin Epigenetics, 2021. **13**(1): p. 138.
201. Nguyen, V.T., et al., *Differential epigenetic reprogramming in response to specific endocrine therapies promotes cholesterol biosynthesis and cellular invasion*. Nat Commun, 2015. **6**: p. 10044.
202. Endo, A., et al., *Inhibition of cholesterol synthesis in vitro and in vivo by ML-236A and ML-236B, competitive inhibitors of 3-hydroxy-3-methylglutaryl-coenzyme A reductase*. Eur J Biochem, 1977. **77**(1): p. 31-6.
203. Serandour, A.A., et al., *Epigenetic switch involved in activation of pioneer factor FOXA1-dependent enhancers*. Genome Res, 2011. **21**(4): p. 555-65.
204. Lupien, M., et al., *FoxA1 translates epigenetic signatures into enhancer-driven lineage-specific transcription*. Cell, 2008. **132**(6): p. 958-70.
205. Liu, Y., et al., *FOXA1 O-GlcNAcylation-mediated transcriptional switch governs metastasis capacity in breast cancer*. Sci Adv, 2023. **9**(33): p. eadg7112.

206. Ji, D., et al., *FOXA1 forms biomolecular condensates that unpack condensed chromatin to function as a pioneer factor*. Mol Cell, 2024. **84**(2): p. 244-260 e7.
207. Carroll, J.S., et al., *Chromosome-wide mapping of estrogen receptor binding reveals long-range regulation requiring the forkhead protein FoxA1*. Cell, 2005. **122**(1): p. 33-43.
208. Roth, E., *Nonnutritive effects of glutamine*. J Nutr, 2008. **138**(10): p. 2025S-2031S.
209. Cruzat, V., et al., *Glutamine: Metabolism and Immune Function, Supplementation and Clinical Translation*. Nutrients, 2018. **10**(11).
210. Heeneman, S., N.E. Deutz, and W.A. Buurman, *The concentrations of glutamine and ammonia in commercially available cell culture media*. J Immunol Methods, 1993. **166**(1): p. 85-91.
211. Demas, D.M., et al., *Glutamine Metabolism Drives Growth in Advanced Hormone Receptor Positive Breast Cancer*. Front Oncol, 2019. **9**: p. 686.
212. Shajahan-Haq, A.N., et al., *MYC regulates the unfolded protein response and glucose and glutamine uptake in endocrine resistant breast cancer*. Mol Cancer, 2014. **13**: p. 239.
213. Wise, D.R., et al., *Myc regulates a transcriptional program that stimulates mitochondrial glutaminolysis and leads to glutamine addiction*. Proceedings of the National Academy of Sciences of the United States of America, 2008. **105**(48): p. 18782-18787.
214. Nazar, E., et al., *The Emerging Role of Succinate Dehydrogenase Genes (SDHx) in Tumorigenesis*. Int J Hematol Oncol Stem Cell Res, 2019. **13**(2): p. 72-82.
215. McDonough, M.A., et al., *Structural studies on human 2-oxoglutarate dependent oxygenases*. Curr Opin Struct Biol, 2010. **20**(6): p. 659-72.
216. Morin, A., et al., *TET-Mediated Hypermethylation Primes SDH-Deficient Cells for HIF2alpha-Driven Mesenchymal Transition*. Cell Rep, 2020. **30**(13): p. 4551-4566 e7.
217. Hoekstra, A.S., et al., *Inactivation of SDH and FH cause loss of 5hmC and increased H3K9me3 in paraganglioma/pheochromocytoma and smooth muscle tumors*. Oncotarget, 2015. **6**(36): p. 38777-88.
218. Killian, J.K., et al., *Succinate dehydrogenase mutation underlies global epigenomic divergence in gastrointestinal stromal tumor*. Cancer Discov, 2013. **3**(6): p. 648-57.
219. Wang, H., Y. Chen, and G. Wu, *SDHB deficiency promotes TGFbeta-mediated invasion and metastasis of colorectal cancer through transcriptional repression complex SNAIL1-SMAD3/4*. Transl Oncol, 2016. **9**(6): p. 512-520.
220. Quan, J., A.M. Bode, and X. Luo, *ACSL family: The regulatory mechanisms and therapeutic implications in cancer*. Eur J Pharmacol, 2021. **909**: p. 174397.

## References

---

221. Ren, P., W.Z. Li, and L. Xue, *GLYAT regulates JNK-mediated cell death in Drosophila*. Scientific Reports, 2017. **7**.
222. Aruoma, O.I., et al., *The antioxidant action of N-acetylcysteine: its reaction with hydrogen peroxide, hydroxyl radical, superoxide, and hypochlorous acid*. Free Radic Biol Med, 1989. **6**(6): p. 593-7.
223. Halasi, M., et al., *ROS inhibitor N-acetyl-L-cysteine antagonizes the activity of proteasome inhibitors*. Biochem J, 2013. **454**(2): p. 201-8.
224. Dodson, M., R. Castro-Portuguez, and D.D. Zhang, *NRF2 plays a critical role in mitigating lipid peroxidation and ferroptosis*. Redox Biol, 2019. **23**: p. 101107.
225. Endale, H.T., W. Tesfaye, and T.A. Mengstie, *ROS induced lipid peroxidation and their role in ferroptosis*. Front Cell Dev Biol, 2023. **11**: p. 1226044.
226. Redza-Dutordoir, M. and D.A. Averill-Bates, *Activation of apoptosis signalling pathways by reactive oxygen species*. Biochim Biophys Acta, 2016. **1863**(12): p. 2977-2992.
227. Azad, M.B., Y. Chen, and S.B. Gibson, *Regulation of autophagy by reactive oxygen species (ROS): implications for cancer progression and treatment*. Antioxid Redox Signal, 2009. **11**(4): p. 777-90.
228. Reinema, F.V., et al., *Tamoxifen induces radioresistance through NRF2-mediated metabolic reprogramming in breast cancer*. Cancer Metab, 2023. **11**(1): p. 3.
229. Achinger-Kawecka, J., et al., *Epigenetic reprogramming at estrogen-receptor binding sites alters 3D chromatin landscape in endocrine-resistant breast cancer*. Nat Commun, 2020. **11**(1): p. 320.
230. Shlyueva, D., G. Stampfel, and A. Stark, *Transcriptional enhancers: from properties to genome-wide predictions*. Nat Rev Genet, 2014. **15**(4): p. 272-86.
231. Bommi-Reddy, A., et al., *CREBBP/EP300 acetyltransferase inhibition disrupts FOXA1-bound enhancers to inhibit the proliferation of ER+ breast cancer cells*. PLoS One, 2022. **17**(3): p. e0262378.
232. Guan, X., et al., *Inhibition of HDAC2 sensitises antitumour therapy by promoting NLRP3/GSDMD-mediated pyroptosis in colorectal cancer*. Clin Transl Med, 2024. **14**(6): p. e1692.
233. Pulya, S., et al., *Selective HDAC3 Inhibitors with Potent In Vivo Antitumor Efficacy against Triple-Negative Breast Cancer*. J Med Chem, 2023. **66**(17): p. 12033-12058.
234. Zhu, H., et al., *Histone deacetylase-3 activation promotes tumor necrosis factor-alpha (TNF-alpha) expression in cardiomyocytes during lipopolysaccharide stimulation*. J Biol Chem, 2010. **285**(13): p. 9429-9436.

235. Hou, Y., et al., *PHF20L1 as a H3K27me2 reader coordinates with transcriptional repressors to promote breast tumorigenesis*. *Sci Adv*, 2020. **6**(16): p. eaaz0356.
236. Hong, S.H., et al., *Identification of JmjC domain-containing UTX and JMJD3 as histone H3 lysine 27 demethylases*. *Proceedings of the National Academy of Sciences of the United States of America*, 2007. **104**(47): p. 18439-18444.
237. Hua, C., et al., *KDM6 Demethylases and Their Roles in Human Cancers*. *Front Oncol*, 2021. **11**: p. 779918.
238. Laukka, T., et al., *Cancer-associated 2-oxoglutarate analogues modify histone methylation by inhibiting histone lysine demethylases*. *Journal of Molecular Biology*, 2018. **430**(18): p. 3081-3092.
239. Berger, L., et al., *Expression of H3K4me3 and H3K9ac in breast cancer*. *J Cancer Res Clin Oncol*, 2020. **146**(8): p. 2017-2027.
240. Messier, T.L., et al., *Histone H3 lysine 4 acetylation and methylation dynamics define breast cancer subtypes*. *Oncotarget*, 2016. **7**(5): p. 5094-109.
241. Ravindran Menon, D., et al., *H3K4me3 remodeling induced acquired resistance through O-GlcNAc transferase*. *Drug Resist Updat*, 2023. **71**: p. 100993.
242. Kao, H.Y., et al., *The PML1-WDR5 axis regulates H3K4me3 marks and promotes stemness of estrogen receptor-positive breast cancer*. *Res Sq*, 2023.
243. Naik, A., N. Dalpatraj, and N. Thakur, *Global Histone H3 Lysine 4 Trimethylation (H3K4me3) Landscape Changes in Response to TGFbeta*. *Epigenet Insights*, 2021. **14**: p. 25168657211051755.
244. Kwon, M., et al., *H2B ubiquitylation enhances H3K4 methylation activities of human KMT2 family complexes*. *Nucleic Acids Res*, 2020. **48**(10): p. 5442-5456.
245. Wood, A., et al., *The Paf1 complex is essential for histone monoubiquitination by the Rad6-Bre1 complex, which signals for histone methylation by COMPASS and Dot1p*. *J Biol Chem*, 2003. **278**(37): p. 34739-42.
246. Ng, H.H., S. Dole, and K. Struhl, *The Rtf1 component of the Paf1 transcriptional elongation complex is required for ubiquitination of histone H2B*. *J Biol Chem*, 2003. **278**(36): p. 33625-8.
247. Van Oss, S.B., C.E. Cucinotta, and K.M. Arndt, *Emerging Insights into the Roles of the Paf1 Complex in Gene Regulation*. *Trends Biochem Sci*, 2017. **42**(10): p. 788-798.
248. Johansson, C., et al., *The roles of Jumonji-type oxygenases in human disease*. *Epigenomics*, 2014. **6**(1): p. 89-120.

## References

---

249. Rondinelli, B., et al., *H3K4me3 demethylation by the histone demethylase KDM5C/JARID1C promotes DNA replication origin firing*. *Nucleic Acids Res*, 2015. **43**(5): p. 2560-74.
250. Di Cerbo, V., et al., *Acetylation of histone H3 at lysine 64 regulates nucleosome dynamics and facilitates transcription*. *Elife*, 2014. **3**: p. e01632.
251. Schuyler, R.P., et al., *Minimizing Batch Effects in Mass Cytometry Data*. *Front Immunol*, 2019. **10**: p. 2367.
252. Fernandez-Zapata, C., et al., *The use and limitations of single-cell mass cytometry for studying human microglia function*. *Brain Pathol*, 2020. **30**(6): p. 1178-1191.
253. Lane, D.P., *Cancer. p53, guardian of the genome*. *Nature*, 1992. **358**(6381): p. 15-6.
254. Williams, A.B. and B. Schumacher, *p53 in the DNA-Damage-Repair Process*. *Cold Spring Harb Perspect Med*, 2016. **6**(5).
255. el-Deiry, W.S., et al., *WAF1, a potential mediator of p53 tumor suppression*. *Cell*, 1993. **75**(4): p. 817-25.
256. Zuckerman, V., et al., *Tumour suppression by p53: the importance of apoptosis and cellular senescence*. *J Pathol*, 2009. **219**(1): p. 3-15.
257. Bouvard, V., et al., *Tissue and cell-specific expression of the p53-target genes: bax, fas, mdm2 and waf1/p21, before and following ionising irradiation in mice*. *Oncogene*, 2000. **19**(5): p. 649-60.
258. Nakano, K. and K.H. Vousden, *PUMA, a novel proapoptotic gene, is induced by p53*. *Mol Cell*, 2001. **7**(3): p. 683-94.
259. Xie, S., et al., *Reactive oxygen species-induced phosphorylation of p53 on serine 20 is mediated in part by polo-like kinase-3*. *J Biol Chem*, 2001. **276**(39): p. 36194-9.
260. Shi, T., et al., *DNA damage and oxidant stress activate p53 through differential upstream signaling pathways*. *Free Radic Biol Med*, 2021. **172**: p. 298-311.
261. Momand, J., et al., *The mdm-2 oncogene product forms a complex with the p53 protein and inhibits p53-mediated transactivation*. *Cell*, 1992. **69**(7): p. 1237-45.
262. Honda, R., H. Tanaka, and H. Yasuda, *Oncoprotein MDM2 is a ubiquitin ligase E3 for tumor suppressor p53*. *FEBS Lett*, 1997. **420**(1): p. 25-7.
263. Yao, Y., et al., *MDM2: current research status and prospects of tumor treatment*. *Cancer Cell Int*, 2024. **24**(1): p. 170.
264. Portman, N., et al., *MDM2 inhibition in combination with endocrine therapy and CDK4/6 inhibition for the treatment of ER-positive breast cancer*. *Breast Cancer Res*, 2020. **22**(1): p. 87.

265. Johnson, D.G., K. Ohtani, and J.R. Nevins, *Autoregulatory control of E2F1 expression in response to positive and negative regulators of cell cycle progression*. *Genes Dev*, 1994. **8**(13): p. 1514-25.
266. Sears, R., K. Ohtani, and J.R. Nevins, *Identification of positively and negatively acting elements regulating expression of the E2F2 gene in response to cell growth signals*. *Mol Cell Biol*, 1997. **17**(9): p. 5227-35.
267. Adams, M.R., et al., *Complex transcriptional regulatory mechanisms control expression of the E2F3 locus*. *Mol Cell Biol*, 2000. **20**(10): p. 3633-9.
268. Gao, Q., et al., *Impact of aromatase inhibitor treatment on global gene expression and its association with antiproliferative response in ER+ breast cancer in postmenopausal patients*. *Breast Cancer Res*, 2019. **22**(1): p. 2.
269. Miller, T.W., et al., *ERalpha-dependent E2F transcription can mediate resistance to estrogen deprivation in human breast cancer*. *Cancer Discov*, 2011. **1**(4): p. 338-51.
270. Gerdes, J., et al., *Production of a mouse monoclonal antibody reactive with a human nuclear antigen associated with cell proliferation*. *Int J Cancer*, 1983. **31**(1): p. 13-20.
271. Li, L.T., et al., *Ki67 is a promising molecular target in the diagnosis of cancer (review)*. *Mol Med Rep*, 2015. **11**(3): p. 1566-72.
272. Zhang, M., et al., *TGF-beta Signaling and Resistance to Cancer Therapy*. *Front Cell Dev Biol*, 2021. **9**: p. 786728.
273. Thompson, A.M., D.J. Kerr, and C.M. Steel, *Transforming growth factor beta 1 is implicated in the failure of tamoxifen therapy in human breast cancer*. *Br J Cancer*, 1991. **63**(4): p. 609-14.
274. Hao, Y., D. Baker, and P. Ten Dijke, *TGF-beta-Mediated Epithelial-Mesenchymal Transition and Cancer Metastasis*. *Int J Mol Sci*, 2019. **20**(11).
275. Babushkina, N., et al., *Role of TGF-beta signaling in the mechanisms of tamoxifen resistance*. *Cytokine Growth Factor Rev*, 2021. **62**: p. 62-69.
276. Attisano, L. and J.L. Wrana, *Smads as transcriptional co-modulators*. *Curr Opin Cell Biol*, 2000. **12**(2): p. 235-43.
277. Rodriguez-Martinez, A., et al., *Analysis of BMP4 and BMP7 signaling in breast cancer cells unveils time-dependent transcription patterns and highlights a common synexpression group of genes*. *BMC Med Genomics*, 2011. **4**: p. 80.
278. Dennler, S., et al., *Induction of sonic hedgehog mediators by transforming growth factor-beta: Smad3-dependent activation of Gli2 and Gli1 expression in vitro and in vivo*. *Cancer Res*, 2007. **67**(14): p. 6981-6.
279. Dennler, S., et al., *Cloning of the human GLI2 Promoter: transcriptional activation by transforming growth factor-beta via SMAD3/beta-catenin cooperation*. *J Biol Chem*, 2009. **284**(46): p. 31523-31.

## References

---

280. Inaguma, S., et al., *GLI1 orchestrates CXCR4/CXCR7 signaling to enhance migration and metastasis of breast cancer cells*. *Oncotarget*, 2015. **6**(32): p. 33648-57.
281. Pang, K.R., et al., *Biological and clinical basis for molecular studies of interferons*. *Methods Mol Med*, 2005. **116**: p. 1-23.
282. Lee, A.J. and A.A. Ashkar, *The Dual Nature of Type I and Type II Interferons*. *Front Immunol*, 2018. **9**: p. 2061.
283. Dimberg, A., et al., *Ser727/Tyr701-phosphorylated Stat1 is required for the regulation of c-Myc, cyclins, and p27Kip1 associated with ATRA-induced G0/G1 arrest of U-937 cells*. *Blood*, 2003. **102**(1): p. 254-61.
284. Chin, Y.E., et al., *Cell growth arrest and induction of cyclin-dependent kinase inhibitor p21 WAF1/CIP1 mediated by STAT1*. *Science*, 1996. **272**(5262): p. 719-22.
285. Lui, A.J., et al., *IFITM1 suppression blocks proliferation and invasion of aromatase inhibitor-resistant breast cancer in vivo by JAK/STAT-mediated induction of p21*. *Cancer Lett*, 2017. **399**: p. 29-43.
286. Lee, C.K., et al., *STAT1 affects lymphocyte survival and proliferation partially independent of its role downstream of IFN-gamma*. *J Immunol*, 2000. **164**(3): p. 1286-92.
287. Stephanou, A., et al., *Opposing actions of STAT-1 and STAT-3 on the Bcl-2 and Bcl-x promoters*. *Cell Death Differ*, 2000. **7**(3): p. 329-30.
288. Escher, T.E., et al., *Enhanced IFN $\alpha$  Signaling Promotes Ligand-Independent Activation of ER $\alpha$  to Promote Aromatase Inhibitor Resistance in Breast Cancer*. *Cancers (Basel)*, 2021. **13**(20).
289. Ostojic, A., R. Vrhovac, and S. Verstovsek, *Ruxolitinib: a new JAK1/2 inhibitor that offers promising options for treatment of myelofibrosis*. *Future Oncol*, 2011. **7**(9): p. 1035-43.
290. Simon, A.R., et al., *Activation of the JAK-STAT pathway by reactive oxygen species*. *Am J Physiol*, 1998. **275**(6): p. C1640-52.
291. Kumar, V., et al., *The Role of Notch, Hedgehog, and Wnt Signaling Pathways in the Resistance of Tumors to Anticancer Therapies*. *Front Cell Dev Biol*, 2021. **9**: p. 650772.

## Supplementary Data

### Supplementary Table 1: Gene set enrichment analysis of RNA sequencing data using the hallmark gene collection from the Molecular Signature Database.

Analysis was performed with significant ( $\text{padj} \leq 0.05$ ) expressed genes across the indicated comparisons. Normalized Enrichment Score (NES) and the False Discovery Rate (FDR) q-value are indicated with statistically significant scores (FDR q-value  $< 0.25$ ) written in bold text.

Pathway	siGLYATL1		GLYATL1		GLYATL1	
	vs siControl		KO1 vs LTED		KO2 vs LTED	
	NES	FDR q-val	NES	FDR q-val	NES	FDR q-val
MITOTIC_SPINDLE	<b>-1.52</b>	<b>0.108</b>	-1.01	0.778	-0.97	0.911
G2M_CHECKPOINT	<b>-1.49</b>	<b>0.097</b>	<b>-1.44</b>	<b>0.161</b>	<b>-1.70</b>	<b>0.008</b>
E2F_TARGETS	<b>-1.48</b>	<b>0.081</b>	<b>-1.44</b>	<b>0.225</b>	<b>-1.92</b>	<b>0.001</b>
TNFA_SIGNALING_VIA_NFKB	1.19	0.281	<b>1.23</b>	<b>0.210</b>	<b>1.34</b>	<b>0.158</b>
INFLAMMATORY_RESPONSE	<b>1.61</b>	<b>0.064</b>	1.17	0.272	<b>1.72</b>	<b>0.004</b>
INTERFERON_ALPHA_RESPONSE	-1.06	0.705	<b>1.97</b>	<b>&lt;0.0001</b>	<b>2.51</b>	<b>&lt;0.0001</b>
INTERFERON_GAMMA_RESPONSE	<b>1.31</b>	<b>0.176</b>	<b>1.8</b>	<b>0.004</b>	<b>2.54</b>	<b>&lt;0.0001</b>
P53_PATHWAY	<b>1.61</b>	<b>0.045</b>	<b>1.3</b>	<b>0.192</b>	<b>1.43</b>	<b>0.077</b>
APOPTOSIS	1.16	0.320	<b>1.43</b>	<b>0.111</b>	<b>1.52</b>	<b>0.051</b>
IL2_STAT5_SIGNALING	-1.29	0.312	<b>1.4</b>	<b>0.125</b>	<b>1.45</b>	<b>0.075</b>
IL6_JAK_STAT3_SIGNALING	<b>1.39</b>	<b>0.146</b>	0.96	0.567	<b>1.77</b>	<b>0.002</b>
ANGIOGENESIS	<b>1.54</b>	<b>0.059</b>	<b>1.51</b>	<b>0.065</b>	<b>1.83</b>	<b>0.001</b>
ESTROGEN_RESPONSE_EARLY	<b>1.25</b>	<b>0.213</b>	<b>1.65</b>	<b>0.022</b>	1.11	0.473

## Supplementary Data

---

ESTROGEN_RE- SPONSE_LATE	1.13	0.369	<b>1.39</b>	<b>0.118</b>	1.13	0.459
EPITHELIAL_MESENCHY- MAL_TRANSITION	<b>1.34</b>	<b>0.172</b>	<b>1.31</b>	<b>0.199</b>	1.17	0.413
NOTCH_SIGNALING	<b>1.65</b>	<b>0.082</b>	-1.23	0.669	1.13	0.447
HEDGEHOG_SIGNALING	<b>-1.40</b>	<b>0.150</b>	1.03	0.523	0.93	0.748

---